

ABSTRACT

HENRY, JOSH BRADY. Characterization of Tobacco Nutrient Disorders via Remote Sensing. (Under the direction of Drs. Matthew C. Vann and Brian E. Whipker).

This research investigated nutrient disorders in flue-cured tobacco grown in greenhouse and field settings using spectral imaging. Macro- and micronutrient deficiencies and toxicities were induced in a hydroponic sand-culture system, which provided data and images to develop an interactive online diagnostic key. This key was published in 2017 and is intended to be a resource for tobacco growers. Following the development of the online key, the greenhouse-based studies were replicated to investigate the spectral response of nitrogen (N), phosphorus (P), potassium (K), magnesium (Mg), and sulfur (S) deficiencies as well as boron (B) toxicity. Symptoms were monitored using a handheld spectroradiometer to capture the unique reflectance curves exhibited by each disorder. Unsupervised classification methods were used to accurately distinguish among the recorded symptoms. We achieved 92%, 82%, and 75% overall classification accuracies for young, intermediate, and mature macronutrient-deficient plants, respectively. Field studies were also conducted to induce and investigate the spectral response of tobacco plants under nutritional stress. Unmanned aerial vehicle (UAV)-based hyperspectral imagery was obtained on a biweekly basis throughout the 2018 and 2019 growing seasons. Data transformation and manipulation enabled classification accuracies near 100%, even without the presence of visible symptoms. This research is intended enable the development of cost-effective spectral sensors made specifically to distinguish among multiple nutrient disorders.

© Copyright 2020 Josh Brady Henry
All Rights Reserved

Characterization of Tobacco Nutrient Disorders via Aerial and Ground-Based Hyperspectral
Remote Sensing

by
Josh B. Henry

A dissertation submitted to the Graduate Faculty of
North Carolina State University
in partial fulfillment of the
requirements for the degree of
Doctor of Philosophy

Horticultural Science & Crop Science

Raleigh, North Carolina
2020

APPROVED BY:

Matthew C. Vann
Committee Co-Chair

Brian E. Whipker
Committee Co-Chair

Josh Gray

Carl Crozier

DEDICATION

To Gracie, whose unconditional love and support got me through these challenging years.

BIOGRAPHY

Josh B. Henry was born in Cleveland, Ohio on January 22, 1993 to Christopher and Christine Crites. Henry graduated summa cum laude from The Ohio State Agricultural Technical Institute in May 2013, receiving an Associate of Applied Science in Greenhouse and Nursery Management. He later graduated summa cum laude with his Bachelor of Science in Sustainable Plant Systems with Specialization in Horticulture from The Ohio State University in December 2014. Henry interned at Smith Gardens in Aurora, Oregon during the spring of 2015 prior to beginning his Master of Science at North Carolina State University in August 2015. His master's research investigated low phosphorus fertilization of greenhouse bedding crops. In May 2017, Henry completed his Master of Science and began his doctoral work at studying remote sensing of plant nutrient disorders in flue-cured tobacco. Henry's graduate research was completed in the summer of 2019 and he completed his graduate work at the end of 2019. He then began working as a Research Scientist at The Scotts Miracle-Gro Company in Marysville, Ohio.

ACKNOWLEDGMENTS

This work would not have been possible without the help and support of countless individuals. Firstly, I would like to acknowledge my co-advisors, Matthew Vann and Brian Whipker. Both went above and beyond what is typically expected of a graduate advisor, providing immeasurable personal and professional mentorship that helped lead to my current success. Josh Gray, Carl Crozier, and Rob Austin also provided significant contributions on my graduate committee in terms of planning research and reviewing chapters. I also want to thank the North Carolina Tobacco Foundation, Inc. for funding my research.

Conducting my research relied on the help of many individuals over the course of my program. I would like to sincerely thank the technicians, Ingram McCall, Scott Whitley, and Jeremy Machacek who all helped so much in planning and performing these experiments. I would like to thank all those in administration who helped me, but especially to Rachel McLaughlin and Angie Barefoot who kept me on track and assisted me with challenges associated with co-majoring. Thank you to Brian Jackson, Helen Kraus, and Bob Patterson for their mentorship in teaching. Thank you also to those in extension who helped with my research; Norman Harrell, Tommy Batts, Jessica Anderson, Bryant Spivey, and many others.

Thank you to all the graduate students who helped me in the classroom, in the field, and provided me with a sense of community during my time in North Carolina; Nathan Jahnke, Paige Herring, Hunter Landis, Maggie Short, Paul Cockson, Nick Manning, Drew Clapp, Camden Finch, Matt Inman, Hans Spalholz, Paul Bartley, and countless others. I also wish to thank the undergraduates whom I have had the pleasure of working with over the past several years. To Patrick Veazie, Jeb Bullard, Channie Renn, and Drake Stevens, thank you all so much for your

help. Thank you especially to Marschall Furman for the countless hours of statistical assistance and help with coding.

I want to sincerely thank the Whipker family for taking us in when we could not spend holidays with our families. That type of caring and commitment to supporting a graduate student goes further than you could ever realize. I would also like to acknowledge Forest Hills Baptist Church for the sense of community they provided, and the many friends made through life group. Thank you to the support staff in the immunization clinic who made it possible for me to breathe in the slurry of pollen and other particulate matter referred to as “air” in North Carolina. Also, thank you to the many individuals at the NCSU Counseling Center who helped me overcome the stress that came with graduate school. Thank you for helping me understand that it is always okay to ask for help when you need it.

Lastly, I wish to thank my family for their love and support over the past several years. To my parents, thank you for supporting my interest in a field you knew little about, and for opening so many doors. To my grandparents, thank you for always checking in to see how my program was going, and for keeping me well fed when I came home to visit for the holidays. Thank you to my in-laws who have continued to show me their compassion and caring on their many vacations to North Carolina. Thank you to Michael, Brad, Mike, and Andrew for your brotherhood over the years. Thank you to Gracie, whose playful and rambunctious nature helped me find time for fun and reminded me the joys of life. Most importantly, I want to thank Amy Henry, who provided me with more kindness, understanding, love, and support than anyone could hope to receive from their spouse. I truly would not be here without you.

TABLE OF CONTENTS

LIST OF TABLES	ix
LIST OF FIGURES	xi
Chapter 1. Hyperspectral Data Analysis Methods for Crop Nutrient Monitoring.....	1
Abstract	2
Introduction.....	3
Hyperspectral Remote Sensing	9
Plant Nutrient Monitoring.....	14
Pre-Processing Hyperspectral Data.....	17
Hyperspectral Data Analysis Methods.....	23
Hyperspectral Applications in Plant Nutrition.....	27
Available Analysis Software.....	32
Conclusions.....	34
Acknowledgements.....	35
References.....	36
Chapter 2. Nutrient Disorders of Burley and Flue-Cured Tobacco: Part 1 – Macronutrient Deficiencies.....	45
Abstract.....	46
Experiment Outline.....	47
Data Collection and Analysis.....	49
Macronutrient Disorders	50
Nitrogen	50
Phosphorus.....	50
Potassium	51
Calcium.....	52
Magnesium.....	53
Sulfur.....	54
Conclusions.....	55
Acknowledgements.....	55
References.....	56
Chapter 3. Nutrient Disorders of Burley and Flue-Cured Tobacco: Part 2 – Micronutrient Disorders.....	65

Abstract	67
Experiment Outline	68
Data Collection and Analysis.....	69
Micronutrient Disorders	70
Boron.....	70
Copper.....	71
Iron	73
Manganese	73
Molybdenum	74
Zinc	75
Conclusions.....	75
Acknowledgements.....	76
References.....	77
Chapter 4. Spectroscopic Differentiation of Nutrient Disorders in Greenhouse Grown Flue-Cured Tobacco.....	85
Abstract	86
Introduction.....	87
Materials and Methods.....	90
Plant Material and Experimental Design	90
Spectroscopic Measurements	92
Leaf Tissue Analysis.....	93
Data Preparation.....	94
Band Selection	95
Symptom Classification	95
Results and Discussion	96
Band Selection	101
Symptom Classification	106
Acknowledgements.....	108
References.....	109
Chapter 5. UAV-Based Hyperspectral Remote Sensing for Distinguishing Nutrient Disorders in Flue-Cured Tobacco.....	112
Abstract	113
Introduction.....	114

Materials and Methods.....	119
Plant Material and Experimental Design	119
Spectroscopic Measurements.....	121
Nutrient Analysis	122
Data Preprocessing.....	123
Band Selection	124
Symptom Classification	125
Results and Discussion	126
Symptomology	126
Foliar nutrients	127
Band Selection	129
Symptom Classification	132
Acknowledgements.....	136
Literature Cited	137
Chapter 6. Spectral Characterization of Boron Toxicity in Flue-Cured Tobacco	144
Abstract.....	145
Introduction.....	146
Materials and Methods.....	148
Greenhouse Experiment.....	148
Field Experiment.....	150
Spectral Measurements	152
Nutrient Analysis	153
Data Preprocessing.....	154
Band Selection	155
Symptom Classification	156
Results and Discussion	157
Greenhouse Study	157
Field Study	163
Acknowledgements.....	174
References.....	175

LIST OF TABLES

Table 2.1. Mean dry weights of burley and flue-cured tobacco grown with a deficient macronutrient treatment compared to plants grown with a complete fertilizer.	57
Table 2.2. Foliar nutrient concentrations of burley and flue-cured tobacco grown with a deficient macronutrient treatment compared to plants grown with a complete fertilizer.	58
Table 3.1. Mean dry weights of burley and flue-cured tobacco grown with a deficient or toxic micronutrient treatment compared to plants grown with a complete fertilizer.	78
Table 3.2. Foliar nutrient concentrations of burley and flue-cured tobacco grown with a deficient or toxic micronutrient treatment compared to plants grown with a complete fertilizer.	79
Table 4.1. Pairwise comparisons of foliar nutrient concentrations found in the most recently matured leaves of young, intermediate, and mature flue-cured tobacco (<i>Nicotiana tabacum</i> L.) plants grown under macronutrient deficient conditions.	98
Table 4.2. Five most significant wavelengths (nm) selected for discrimination among macronutrient deficiencies in flue-cured tobacco (<i>Nicotiana tabacum</i> L.) at three growth stages. Band selection methods included information entropy, first spectral derivative, and second spectral derivative.	104
Table 4.3. Linear discriminant analysis classification accuracies for nutrient deficient flue-cured tobacco (<i>Nicotiana tabacum</i> L.) plants based on principal component analysis.	107

Table 5.1. Average soil properties exhibited at each field site.	120
Table 5.2. Composition of custom deficiency inducing fertilizers created to replicate commercial 6-6-18 tobacco fertilizer devoid of either N, P, or K.	121
Table 5.3. Flue-cured tobacco (<i>Nicotiana tabacum</i> L.) foliar nutrient concentrations observed in the 2018 and 2019 field experiments. The base fertilizer rate of 6- 6-18 was used as a control to compare with the N-deficient (-N), P-deficient (- P), and K-deficient (-K) strip treatments.	129
Table 6.1. Average soil properties exhibited at each field planting site.	151
Table 6.2. Overall classification accuracies calculated among flue-cured tobacco (<i>Nicotiana tabacum</i> L.) plants exhibiting different levels of B toxicity for each hyperspectral image.	167
Table 6.3. Five highest information entropy wavelengths for classifying among flue- cured tobacco (<i>Nicotiana tabacum</i> L.) plants exhibiting different levels of B toxicity for each hyperspectral image.	170
Table 6.4. Five most significant wavelengths selected for discrimination among flue- cured tobacco (<i>Nicotiana tabacum</i> L.) exhibiting different levels of B toxicity for each hyperspectral image. Wavelengths were selected based on first derivate spectra peaks and valleys with highest absolute values.	172
Table 6.5. Five most significant wavelengths selected for discrimination among flue- cured tobacco (<i>Nicotiana tabacum</i> L.) exhibiting different levels of B toxicity for each hyperspectral image. Wavelengths were selected based on second derivate spectra peaks and valleys with highest absolute values.	173

LIST OF FIGURES

Figure 1.1. Example of typical reflectance spectra from healthy tobacco (<i>Nicotiana tabacum</i>) plants (J. Henry, unpublished data) with labels for some of the primary features.	5
Figure 1.2. Visual demonstration of the concept of wide and narrow bands using electromagnetic radiation (EMR) wavelengths in the green spectrum. Similar sized bands may also be found in the near infrared and short-wave infrared (SWIR) spectra.....	6
Figure 1.3. Average (A) foliar spectral reflectance measured from healthy tobacco (<i>Nicotiana tabacum</i>) leaves (J. Henry, unpublished data) with corresponding (B) first and (C) second-order derivative spectra. Derivatives demonstrate the rate of change between each pair of adjacent wavelengths.	22
Figure 1.4. Spectral signatures of three ornamental sweet potato (<i>Ipomoea batatas</i>) cultivars that each exhibit different natural coloration (J. Henry, unpublished data). The cultivars are ‘Sweet Caroline Bewitched Green with Envy’ (SCBGWE), ‘Illusion Midnight Lace’ (IML), and ‘Sweet Caroline Green Yellow’ (SCGY).	31
Figure 1.5. Average spectra from N-deficient tobacco (<i>Nicotiana tabacum</i>) foliage ($n = 70$) compared to that of the asymptomatic control ($n = 325$) (J. Henry, unpublished data).	32
Figure 2.1. Nitrogen-deficient tobacco plants exhibiting a pale yellow coloration (A) at an early stage of growth, (B) at a mature stage of growth compared with an	

asymptomatic control, and (C) a foliar symptom progression from asymptomatic (left) to highly symptomatic (right).....	59
Figure 2.2. Symptoms of phosphorus deficiency (A) on a young plant leaf, (B) on the lower foliage of a more mature plant, (C) and advanced symptoms on a mature plant. Symptoms of (D) brown and olive green spotting, in addition to an overall yellowing were present on the lower foliage.	60
Figure 2.3. Potassium (K) deficiency symptoms (A) on the lower leaves of a young tobacco plant with (B) a pale yellowing and interveinal browning. On mature plants (C) K deficiency had a deeper yellow coloration, which (D) was most prominent at the leaf tip.	61
Figure 2.4. Symptoms of (A) distortion of the upper leaves developed initially in response to calcium deficiency. These symptoms were similar to those of (B) boron-deficient tobacco. Flue-cured tobacco primarily exhibited (C) a cut leaf pattern, while burley tobacco primarily exhibited (D) a distorted ‘shepherd’s crook’ appearance. In some instances, (E) the apical meristem would die, leading to a proliferation of axillary shoots which quickly became necrotic.	62
Figure 2.5. Magnesium deficiency symptoms of (A) a bright interveinal yellowing of the central and lower leaves that was easily distinguished from asymptomatic control plants. As symptoms progressed, (B) the lower leaves appeared nearly white and wilted.....	63
Figure 2.6. Tobacco rapidly developed symptoms of sulfur deficiency. Young plants (A) had a prominent yellow coloration, while (B) mature plants exhibited a	

uniform pale yellow coloration that (C) was distinctly paler than the asymptomatic controls.	64
Figure 3.1. Boron-deficient tobacco with (A) thickened and distorted foliage, (B) axillary shoot development at the nodes, (C) death of the apical meristem, chlorosis along the veins, and (D) compared with a much larger control plant.	80
Figure 3.2. Boron toxicity symptoms (A) on the lower foliage of a flue-cured tobacco plant, and (B) along the margins a single leaf.	81
Figure 3.3. Copper deficiency symptoms of (A) small chlorotic and necrotic spotting, (B) large chlorotic and necrotic areas with black veins, (C) blackened necrosis at the base of the petiole, and (D) advanced symptoms primarily at the leaf tip and petiole.	82
Figure 3.4. Upper leaves of a control tobacco plant receiving all essential nutrients (left) compared to a tobacco plant displaying iron deficiency symptoms (right).	83
Figure 3.5. Manganese deficiency symptoms of netted chlorosis (A) on the upper foliage of a burley tobacco plant and (B) compared to the upper foliage of a control burley plant. Symptoms of Mn deficiency (C) were different on flue-cured tobacco plants, which exhibited a much greener coloration with larger necrotic spots. Symptomatic leaves (D) of burley (top) and flue-cured (bottom) tobacco were different when compared side-by-side.	84
Figure 4.1. Demonstration of the flue-cured tobacco (<i>Nicotiana tabacum</i> L.) symptom severity rating system using N deficiency as an example.	94

Figure 4.2. Average spectra and associated leaf appearance for (A) nitrogen, (B) phosphorus, (C) potassium, (D) magnesium, and (E) sulfur deficiencies in flue-cured tobacco (*Nicotiana tabacum* L.)..... 99

Figure 4.3. Graphs illustrating A) the average spectral reflectance from 350 to 1000 nm for severely N-deficient flue-cured tobacco (*Nicotiana tabacum* L.) compared to the average control spectra, B) the first derivatives of the N-deficient and control spectra, and C) the second derivatives of the N-deficient and control spectra. 100

Figure 4.4. Savitzky-Golay filtered information entropy observed among (A) young, (B) intermediate, and (C) mature flue-cured tobacco (*Nicotiana tabacum* L.) plants. Peak wavelengths demonstrate locations with the most informative bands necessary to distinguish among each nutrient deficiency..... 102

Figure 4.5. First and second derivatives of (A) young, (B) intermediate, and (C) mature flue-cured tobacco (*Nicotiana tabacum* L.) plants smoothed using the gap-segment algorithm. Peak wavelengths demonstrate locations with the most informative bands necessary to distinguish among each nutrient deficiency. 103

Figure 5.1. Savitzky-Golay filtered information entropy observed among flue-cured tobacco (*Nicotiana tabacum* L.) plants grown under N-, P-, and K-deficient conditions. Peak wavelengths demonstrate locations with the most informative bands necessary to distinguish among these deficiencies and asymptomatic plants. 130

Figure 5.2. First and second derivatives for aggregated flue-cured tobacco (*Nicotiana tabacum* L.) plant data smoothed using the gap-segment algorithm. Peak

wavelengths demonstrate locations with the most informative bands necessary to distinguish among N, P, and K deficiencies.	131
Figure 5.3. Heat map demonstrating classification accuracies achieved among aggregated data from all fertilizer treatment combinations used in the 2018 and 2019 field studies. Red cells along the diagonal represent the percentage of correctly classified subjects within a row while the blue cells represent the percentage of misclassified subjects within a row.	134
Figure 6.1. Intermediate symptoms of B toxicity observed on greenhouse-grown flue-cured tobacco (<i>Nicotiana tabacum</i> L.).....	158
Figure 6.2. Savitzky-Golay filtered information entropy observed among mature B-toxic and control flue-cured tobacco (<i>Nicotiana tabacum</i> L.) plants. Peak wavelengths demonstrate locations with the most informative bands necessary to distinguish between B toxicity and the control.....	160
Figure 6.3. First spectral derivatives of mature B-toxic and control flue-cured tobacco (<i>Nicotiana tabacum</i> L.) plants smoothed using the gap-segment algorithm. Peak wavelengths demonstrate locations with the most informative bands necessary to distinguish between B toxicity and the control.	161
Figure 6.4. Second spectral derivatives of mature B-toxic and control flue-cured tobacco (<i>Nicotiana tabacum</i> L.) plants smoothed using the gap-segment algorithm. Peak wavelengths demonstrate locations with the most informative bands necessary to distinguish between B toxicity and the control.	162
Figure 6.5. Symptoms of B toxicity observed on field-grown flue-cured tobacco (<i>Nicotiana tabacum</i> L.).....	164

Figure 6.6. Heat map demonstrating classification accuracies achieved among aggregated data from all fertilizer treatment combinations used in the 2018 and 2019 field studies. Red cells along the diagonal represent the percentage of correctly classified subjects within a row while the blue cells represent the percentage of misclassified subjects within a row. 165

Figure 6.7. Savitzky-Golay filtered information entropy observed among mature B-toxic and control flue-cured tobacco (*Nicotiana tabacum* L.) plants. Peak wavelengths demonstrate locations with the most informative bands necessary to distinguish between B toxicity and the control..... 169

Figure 6.8. First and second derivatives for aggregated flue-cured tobacco (*Nicotiana tabacum* L.) plant data smoothed using the gap-segment algorithm. Peak wavelengths demonstrate locations with the most informative bands necessary to distinguish among each nutrient deficiency..... 171

CHAPTER 1

Hyperspectral Data Analysis Methods for Crop Nutrient Monitoring

(Written in the style of Agronomy Journal)

Hyperspectral Data Analysis Methods for Crop Nutrient Monitoring

Core Ideas:

- Spectral data have potential to distinguish among nutrient disorders in plants.
- Past studies demonstrate hyperspectral quantification of N and other nutrients.
- Nutrient disorders can be classified and distinguished based on spectral patterns.
- Multiple statistical methods are available and are compared by intended application.
- Differences among species, cultivars, and maturity levels require consideration.

Abstract

Spectral remote sensing is rising in popularity as a tool for precision agriculture. Unmanned aerial vehicles (UAVs) have made remote sensing a feasible method for monitoring crop health status. Some current applications include estimating foliar chlorophyll and N concentrations, leaf area index (LAI), and distinguishing among diseases or weed species. Despite the potential of hyperspectral data applications in agriculture, relatively little progress has been made in linking spectral observations from airborne platforms to particular plant disorders. The goal of this review is to provide plant scientists a simple yet comprehensive overview of the most commonly used hyperspectral data analysis methods along with their application to modeling or classification. In particular, this review focuses on hyperspectral data analysis from a plant nutrition perspective. Numerous studies have investigated hyperspectral remote sensing data for modeling and predicting nutrient status in plants. Although N estimation has been most commonly studied, researchers have created spectra-based models to estimate P, K, and other nutrients. Additionally, spectral remote sensing data is used to classify plants based

on a particular feature and there is potential for classifying among multiple nutrient deficiency symptoms simultaneously. Hyperspectral data can provide plant scientists with enormous quantities of information with which to model plant health, and this review aims to elucidate the procedures that should generally be used for plant nutrition purposes.

Abbreviations: **BRDF**, bidirectional reflectance distribution function; **EMR**, electromagnetic radiation; **GUI**, graphical user interface; **ICP-OES**, inductively coupled plasma optical emission spectrometry; **IFOV**, instantaneous field of view; **LAI**, leaf area index; **MRM**, most recently matured; **NIR**, near infrared; **PC**, principal component; **PCA**, principal component analysis; **PLS**, partial least-squares; **PLSR**, partial least-squares regression; **ROI**, region of interest; **SPAD**, soil-plant analysis development; **SPy**, spectral python; **SWIR**, short-wave infrared; **UAV**, unmanned aerial vehicle; **VI**, vegetative index; **VIS**, visible.

Introduction

Traditional crop scouting methods typically involve walking through a field and making notes of any potential issues observed. This method is time consuming and labor intensive, which is why automation via sensors, mechanization, and other technologies is desirable in agricultural production settings (Abdel-Rahman et al., 2010; Pu, 2017b; Yang et al., 2016). Plants exposed to various biotic and abiotic stressors exhibit different visual symptoms due in part to changes in how light interacts with plant tissues (Abdel-Rahman et al., 2010; Behmann et al., 2014). This characteristic enables some sensors to diagnose plant health problems before symptoms are visually apparent (Behmann et al., 2014). Many different types of sensors can be used to provide non-destructive estimations of various biophysical and biochemical

characteristics of vegetation (Liew et al., 2008). Some of these characteristics of interest include yield, biomass, chlorophyll content, and nutrient status (Daughtry et al., 2000; Delloye et al., 2018; Inoue et al., 2012; Li et al., 2018a, 2018b; Mahajan et al., 2017; Rustioni et al., 2018; Thenkabail et al., 2019; Thorp et al., 2017; Wang et al., 2018; Zhang et al., 2013). Sensors can quickly and efficiently collect enormous quantities of data and are becoming commonplace in agricultural production settings (Liew et al., 2008). Of particular interest is remote sensing with spectral sensors mounted to UAVs, commonly referred to as drones. Often small, inexpensive, and easy to use, UAVs provide a rapid method of scouting that can greatly reduce the intensive labor costs associated with traditional scouting (Abdullahi et al., 2015; Huang et al., 2010; Mahajan et al., 2017). Spectral remote sensing provides opportunities for researchers and industry professionals alike to monitor plant growth in a non-destructive manner.

Remote sensing is simply the act of acquiring data from a subject without making physical contact, which can utilize many different types of sensors. Spectral remote sensing typically uses imaging sensors to measure sunlight reflected from a particular object or surface. Although our primary interest is quantifying the sunlight that is reflected from plants, it is important to realize that much of the light is absorbed, transmitted, and scattered as it travels from the sun, through the atmosphere, to the surface of a plant, and finally back to the sensor (Ortenberg, 2019). Understanding how light interacts with plants, the environment, and the atmosphere enables researchers to acquire measurements to estimate biophysical and biochemical attributes of vegetation (Jin and Wang, 2018; Liew et al., 2008). Of current interest is determining the specific wavelengths of light that are correlated with a particular plant attribute or response in order to achieve rapid and specific diagnostics (Pu, 2017b). This requires a thorough knowledge of the physiological basis of plant spectral responses. For instance,

chlorophyll absorption leads to low reflectance in the ranges of 400 to 499 nm and 650 to 699 nm (Liew et al., 2008), while biomass and cell structure lead to steep reflectance in the “red-edge” (Filella and Penuelas, 1994; Gitelson et al., 1996; Pu, 2017b; Thorp et al., 2017) moving into the near-infrared (Figure 1.1). Additionally, one must consider factors such as leaf cuticle thickness and trichome density which both significantly affect how plants interact with light (Liew et al., 2008).

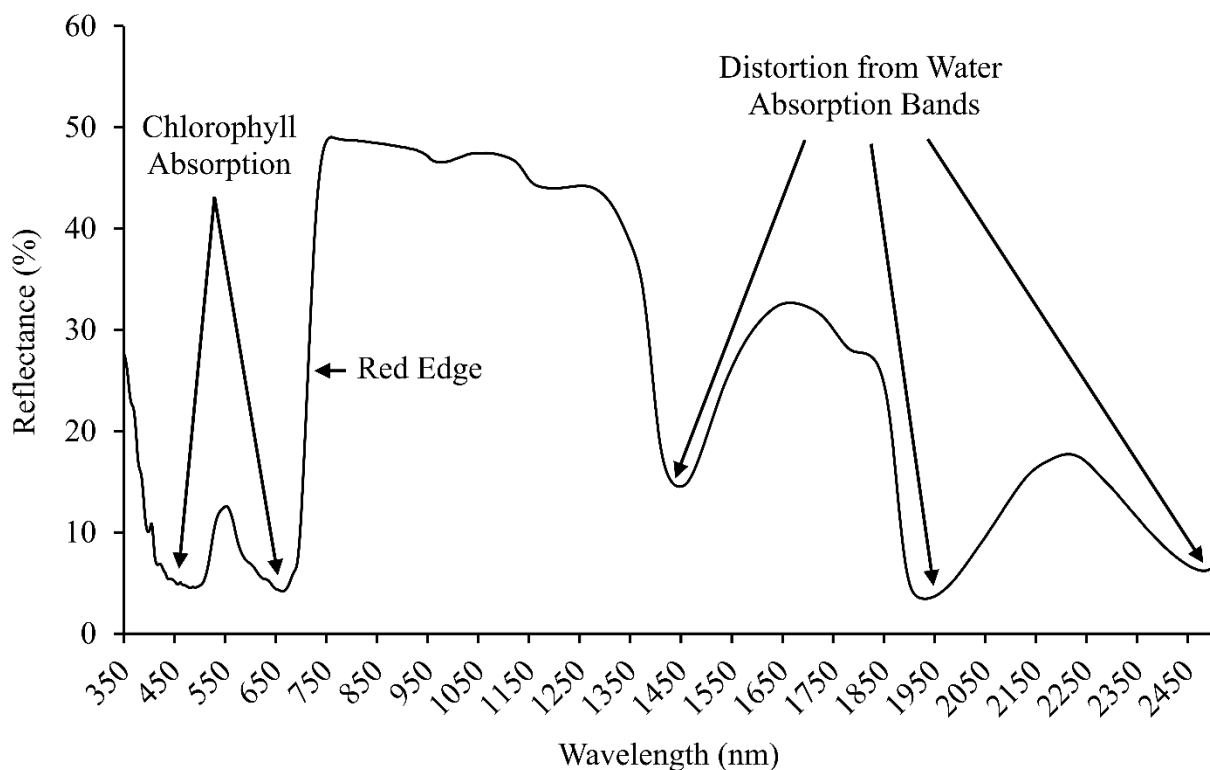


Figure 1.1. Example of typical reflectance spectra from healthy tobacco (*Nicotiana tabacum*) plants (J. Henry, unpublished data) with labels for some of the primary features.

Multispectral imaging typically records the amount of red, green, blue, and infrared light reflected from a surface (Mobaraki and Amigo, 2018). In reality, there are sensors available to

measure the reflectance of any wavelength of electromagnetic radiation (EMR); however, most botanical research focuses on the visible (VIS) and infrared spectra (Ortenberg, 2019). Each measured region of light is commonly referred to as a spectral “band”, which can be wide or narrow in terms of the measured wavelengths (Jensen, 2007). For instance, a sensor may average reflectance from all wavelengths of green light into one broad band, or they may measure reflected light from several narrow bands within the green spectrum (Figure 1.2). In contrast to multispectral imaging, hyperspectral imaging is characterized by measuring reflectance from numerous narrow bands in order to create a nearly continuous spectrum (Mobaraki and Amigo, 2018; Pu, 2017a). The shape of this spectrum is known as a spectral signature and it can be used to identify a particular subject like a unique fingerprint (Mobaraki and Amigo, 2018).

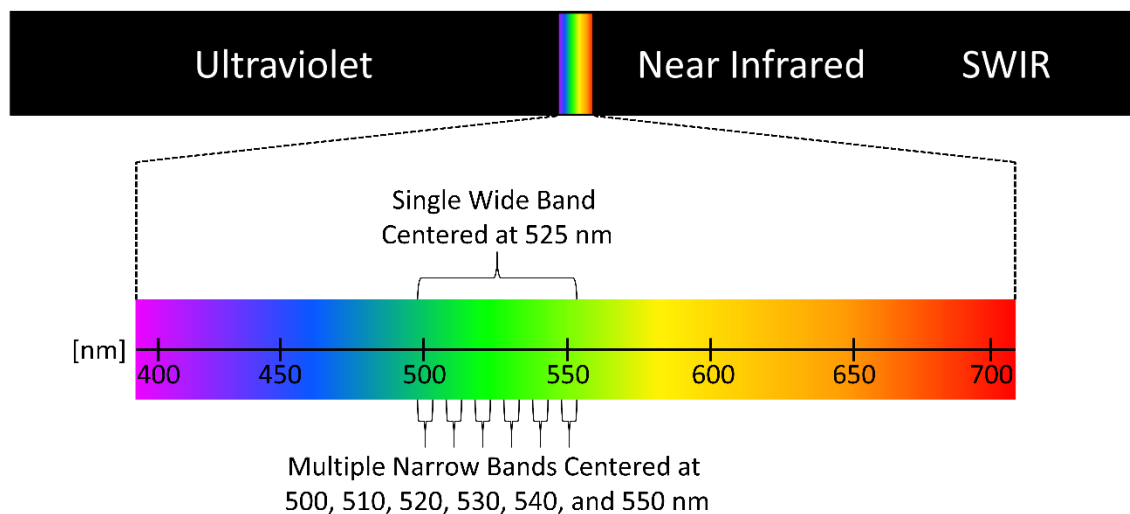


Figure 1.2. Visual demonstration of the concept of wide and narrow bands using electromagnetic radiation (EMR) wavelengths in the green spectrum. Similar sized bands may also be found in the near infrared and short-wave infrared (SWIR) spectra.

Hyperspectral imaging has been used for remote sensing for almost 50 years (Amigo et al., 2015). Spectral imaging sensors utilize a combination of spectroscopy, radiometry, and conventional imaging methods to record one dimension of spectral data to be stored in two spatial dimensions in the form of pixels (Ferrari et al., 2013; Ortenberg, 2019). This three-dimensional array of data, often referred to as a hypercube, may be thought of as numerous images of the same area stacked atop each other, where each layer stores reflectance from a single band (Amigo et al., 2015; Ferrari et al., 2013). Each pixel within a hyperspectral image contains a reflectance value primarily dictated by the subject located in the center of the instantaneous field of view (IFOV) plus noise and scattering from nearby objects (Amigo et al., 2015). Therefore, obtaining the correct pixel size relative to the subject being investigated is essential for obtaining the data needed to model or classify the phenomenon of interest (Woodcock and Strahler, 1987).

Differences observed in spectral reflectance can serve as non-invasive indicators of various plant stressors (Adams et al., 2000a). There are reflectance patterns that differ based on three major factors: 1) the plant species, 2) the stage of development, and 3) the plant stressor. Therefore, it is essential to consider each of these aspects when designing sensors, as spectral responses may exhibit different characteristics due to each variable. Plant pigments play an essential role in spectral detection of plant stress (Jin and Wang, 2018; Pu, 2017b). Many plant stressors result in chlorophyll degradation, leading to symptoms of foliar chlorosis or yellowing (Liew et al., 2008). This makes chlorophyll estimation a good indicator of many plant stressors (Liew et al., 2008). Chlorophyll, which reflects highly in the green spectrum tends to degrade faster than yellow pigments such as carotenoids (Liew et al., 2008; Zhou et al., 2019). Thus, stressors may affect leaf biochemistry in ways that yield unique, detectable spectral signatures.

However, variations in spectral response due to plant stress may manifest in a narrow spectral region. Broad bandwidth measurements may aggregate an observed response with neighboring bands and thus limit the detectability of a particular symptom. This reasoning demonstrates the primary benefit to hyperspectral sensors compared to multispectral sensors.

Commercial multispectral sensors have become readily available and are relatively inexpensive; however, they have considerable limitations. These sensors typically measure reflectance from a few wide bands (approximately 3 to 5), meaning they can be used to distinguish whether a plant is healthy or unhealthy, but likely cannot specify the exact cause of the observed symptoms (Jensen, 2007). In contrast hyperspectral sensors can measure reflectance in many narrow regions of light (hundreds to thousands), but they are very expensive (> \$US 50,000), and typically provide vast quantities of data that are challenging to manage and analyze (Jensen, 2007). Therefore, hyperspectral sensors are well suited for researchers to determine the optimal bands required for sensing various plant health problems, and then using those few bands to develop inexpensive custom sensors. Sensors with fewer measured bands are far less expensive to produce, enabling greater accessibility to crop consultants and growers alike. Although most commercial sensors utilize very broad, indiscriminate bands, it is possible to develop spectral sensors that use the few narrow bands necessary for scouting in a particular crop.

One of the greatest factors currently limiting the use and success of hyperspectral data in the plant sciences is simply the analysis itself (Ferrari et al., 2013; Mobaraki and Amigo, 2018). This is partially due to the many different analysis methods reported over the past several decades (Amigo et al., 2015). Hyperspectral data analysis requires significant knowledge of many remote sensing and statistical concepts not widely known in the plant science community.

However, hyperspectral data present enormous opportunities for researchers to study different processes related to plant growth, development, and physiology. Hyperspectral remote sensing in agriculture is a complex topic that requires collaboration among individuals of several areas of expertise including plant sciences, remote sensing, biological and agricultural engineering, and statistics. Success relies upon interdisciplinary collaboration, but it is still essential for all parties to be familiar with the main concepts, applications, and analysis methods in order to streamline and optimize research. Consequently, there is a significant need for literature tailored specifically to hyperspectral applications in plant science and the most common methods for data manipulation and analysis.

This review aims to simplify and present some of the most popular hyperspectral data analysis methods from the perspective of a plant nutritionist and to provide examples describing how these methods are implemented. We will begin by discussing some of the basic principles of hyperspectral remote sensing, followed by basic concepts in plant nutrient monitoring. Next, we will examine some of the commonly used data pre-processing and analysis techniques. We will then discuss specific applications and findings of hyperspectral remote sensing in plant nutrition followed by a brief summary of available analysis software and possible future directions.

Hyperspectral Remote Sensing

Broad-band multispectral sensors lack the ability to quantify variability on a fine scale because they typically measure reflectance from three to five bands that can be 20 nm wide or greater (Thenkabail et al., 2019). Compared with multispectral sensors, hyperspectral sensors measure data from tens to hundreds of narrow-width bands that can capture reflectance in the VIS and near-infrared (NIR) portions of the electromagnetic spectrum. These narrow

measurements are often near 1 nm in width and can provide a nearly continuous spectra that enable acquisition of well-defined spectral signatures (Thenkabail et al., 2019). Spectra may then be correlated to biochemical, biophysical, and other plant growth factors (Liew et al., 2008; Thenkabail et al., 2019). Narrow-band combinations have potential for accurate separation among vegetation with differing characteristics (Thenkabail et al., 2019). Therefore, it is likely that plants exhibiting symptoms of various nutrient disorders can be distinguished once specific bands are selected (Thenkabail et al., 2019). For these reasons, hyperspectral imaging has been referred to as “the most promising method of remote sensing” (Ortenberg, 2019).

Resolution is a primary factor that must be considered in spectral remote sensing. First, the spatial resolution dictates the surface area of reflectance captured within a pixel, and how many pixels are in a scene. The applicability of spatial resolution is affected by the distance of a sensor from its subject. For instance, a satellite-based sensor may be considered to have high spatial resolution when each pixel corresponds to 1 m or less on the ground (Ortenberg, 2019). In contrast, high spatial resolution for sensors mounted to ground-based vehicles or UAVs may be less than 1 cm. Thus, the spatial resolution is highly dependent on the sensor location relative to its subject. Second, the spectral resolution refers to the number of spectral bands measured and often their associated bandwidths. A high spectral resolution is typically considered to be in the range of 1–10 nm with tens to hundreds of spectral bands (Ortenberg, 2019). Third, the radiometric resolution refers to sensor sensitivity in terms of how many intensity levels are recorded within a single band. Sensors measure reflectance for each band independently, and the values are stored as brightness values that are proportional to spectral radiance (Narumalani and Merani, 2016). The lowest possible radiometric resolution may only distinguish between two intensities, bright and dark. As radiometric resolution increases, different brightness values

become available to bridge the gap bright and dark. Fourth, temporal resolution refers to how often measurements are acquired for the same subject over time. From an agricultural standpoint, it is important to acquire data from multiple different growth stages as plants tend to exhibit different spectral reflectance as they mature. Fifth, an angular resolution considers the different angles of view that may be implemented. Additionally, the overlap that occurs among passes provides different angles of the same subject. These five resolutions (spatial, spectral, radiometric, temporal, and angular) ultimately dictate what can be distinguished within a hyperspectral image.

One must also consider the interaction between spatial and spectral resolutions when designing experiments or analyzing data. The spectral signature recorded within a pixel consists of a mixture of the spectral reflectance of subjects within and near the spatial dimensions of that pixel (Adams et al., 1993). Thus, spectral mixture analysis works to decouple the reflectance of multiple subjects by “modeling image spectra as the linear combination of endmembers” and assuming “reflectance of a pixel is determined by the sum of the reflectance of each material within a pixel multiplied by its fractional cover” (Adams et al., 1993; Dennison and Roberts, 2003; Powell et al., 2007; Youngtob et al., 2011). In terms of agricultural remote sensing, these endmembers could include crop canopy, non-crop species, soil, water, and more. It is imperative to consider that each of these subjects may contribute to any given pixel, and thus, mapping and classifying imagery may need to be done at the sub-pixel level (Powell et al., 2007).

Some basic principles are ubiquitous for spectral sensors that rely on solar reflectance. One of the most important considerations is the time of day at which measurements are taken (Adams et al., 2000b). The angle and intensity of the sun are considerable aspects that affect

measurement quality. In most instances, spectral remote sensing should be conducted within 1 to 2 hr of solar noon, that is, when the sun reaches its peak position. Furthermore, measurements acquired in the morning are less likely to be affected by water stress which typically occurs later in the day (Adams et al., 2000b). Having uniform cloud cover is one of the most important considerations for near-surface imaging. It is preferable to have a cloudless sky, but a uniform cloud deck may also work. Partial clouds are least conducive for measurements as the light intensity will be variable across the field (Jensen, 2007). In contrast, orbital satellite-based sensors necessitate clear skies, as clouds may completely obstruct the ground and any subjects located below the cloud cover.

The relationship of the incidence angle and viewing angle in relation to spectral remote sensing is referred to as the Bidirectional Reflectance Distribution Function (BRDF) (Liu et al., 2017; Roy et al., 2016). This function is defined by the concept that there are no perfect surfaces that will reflect the same quality and quantity of light in every direction, and its application is essential for standardizing satellite-based data (Li et al., 2017). Therefore, the location of the sun, the location of the sensor, and their relationship to one another can affect measurements. These and other issues are important to consider when working with very high resolution data.

Numerous methods are currently used to acquire hyperspectral data. Ground-based sensors can be handheld or mounted to a vehicle such as a truck or tractor (Jensen, 2007). These methods are somewhat slower but are easy to implement and provide a high spatial resolution. Aerial sensors attached to airplanes and UAVs allow for rapid, location-specific data collection. Additionally, most UAVs have global positioning systems (GPS) that enable accurate tracking and recording of the exact location of a measurement (Mattupalli et al., 2017). Recent advances in UAVs have enabled their usage to become widespread, as they are relatively inexpensive and

easy to use (Jensen, 2007). Lastly, spaceborne sensors are mounted to observation satellites constantly imaging the earth (US Geological Survey, 2016).

Spaceborne sensors have improved significantly over recent decades (Jensen, 2007). Satellites launched in the 1970s had broadband sensors with poor spatial resolution. For instance, the Landsat program launched its first satellite in 1972 with the Multispectral Scanner which had a spatial resolution of 79 m and acquired spectral data resolution ≥ 100 nm (US Geological Survey, 2016). In contrast, the Landsat 8 satellite launched in 2013 obtains data at a 15–30 m spatial resolution with 11 bands as narrow as 20 nm in width (Roy et al., 2016; US Geological Survey, 2016). Although resolution has improved with time, most of these orbital sensors lack the spectral or spatial resolution to discriminate plant health problems at a reasonable scale. Other current spaceborne sensors can obtain data from hundreds of narrow bands at varying spatial resolutions (Thenkabail et al., 2019). Immense quantities of spaceborne spectral data are available at no cost from sources including the USGS (US Geological Survey, 2016). These images can have a high temporal resolution, meaning that data are recorded in relatively narrow intervals in time. It is important to note that satellites are typically limited to imaging during overpasses dictated by their orbital configuration and therefore, images may be rendered inappropriate for analysis due to cloud cover and other atmospheric noise.

In summary, there are numerous variables to consider when studying hyperspectral remote sensing. The spatial, spectral, radiometric, temporal, and angular resolutions dictate several qualities of measurements. These resolutions can be affected by the sensor itself, the platform to which the sensor is mounted, the distance from the subject of interest, and many other factors. It is essential to record and report the exact specifications used in a study because so many factors affect the quality of hyperspectral measurements. Unreported specifications

could result in extrapolation and error that could otherwise be avoidable. Therefore, plant scientists using hyperspectral remote sensing should thoroughly consider how each variable will affect the results of their study and clearly demonstrate their reasons for using the selected specifications.

Plant Nutrient Monitoring

Although there are at least 17 essential elements required to complete the cycle of plant growth and maturation, monitoring macronutrient status is considered most important for maintaining crop quality and yield. Carbon, H, and O are integral components of plant structure (Mitra, 2017) but are not monitored like the other essential elements. The remaining essential elements can be divided into the macro- and micronutrients. The essential macronutrients are needed in relatively high concentrations and include N, P, K, Ca, Mg, and S (Mitra, 2017). The essential micronutrients also require a certain level of monitoring to prevent deficiency or toxicity development. The micronutrients include B, Cl, Cu, Fe, Mn, Mo, Ni, and Zn (Mitra, 2017). Cobalt is sometimes considered essential, but its official status as essential or beneficial remains under dispute (Broadley et al., 2012; Mitra, 2017). Additional elements considered beneficial but not essential for plant growth include Al, Se, Si, Na, and V (Broadley et al., 2012; Mitra, 2017).

Each of the essential nutrients perform crucial roles in plant development and deficiencies of each nutrient cause unique symptoms that are visually diagnosable in many instances. Some of the primary effects of nutrient deficiencies include stunting and changes in leaf shape or orientation (Römheld, 2012). Nutrient deficiencies often cause changes in foliar coloration which may appear yellow (chlorotic), white (bleached), brown (necrotic), red, or black

(Römheld, 2012). These changes typically correspond to changes in pigment ratios or cell death. For instance, N deficiency is often associated with chlorosis of the lower foliage due to chlorophyll degradation (Römheld, 2012). Phosphorus deficiency is associated with reddening due to enhanced anthocyanin or betacyanin synthesis and accumulation (Henry et al., 2019). Necrosis often occurs when nutrient deficiencies or toxicities become severe (Römheld, 2012). In any case, color changes are perceived as such due to the various proportions of reflected light. Therefore, quantifying the spectral reflectance may enable sensor-based diagnostics of plant nutrient disorders.

Although plants exhibit spectral variation based on nutrient status, it is important to consider that symptoms often do not occur uniformly among the leaves of a single plant due to differences in nutrient mobility. When mobile nutrients such as N, P, and K are unavailable for uptake, plants can salvage these nutrients from existing tissues, known as “stores”, to enable growth of developing tissues, known as “sinks” (Engels et al., 2012; Hawkesford et al., 2012). These sinks typically include the older, lower foliage. In contrast, immobile nutrients such as Ca, Fe, and Mn exhibit little or no translocation from older tissues, causing symptoms to develop on the actively growing upper leaves. Furthermore, individual leaves may develop symptoms uniformly across the leaf blade, in spotting or blotching patterns, between the veins (interveinal), at the leaf tip, or around the leaf margin (marginal) (Römheld, 2012). Thus, deficiency symptom development is largely dictated by the nutrient in question, plant maturity, and leaf position. These factors must be considered when using sensors to acquire data. If a sensor is held directly above a plant at nadir view (as is often done), the upper canopy structure may likely shade the lower foliage, limiting the potential efficacy in detecting mobile nutrient deficiencies. Therefore, spectral monitoring of nutrient disorders requires thorough planning in terms of crop canopy

structure and how this structure affects measurements on individual plants and the crop as a whole.

The most recently matured (MRM) leaves are commonly harvested for chemical analysis as a standard procedure. Therefore, acquiring spectral data from these leaves is most applicable for commercial applications (Daughtry et al., 2000). This is advantageous for most spectral data acquisition methods because the most recently matured leaves are more likely to be visible to the sensor. However, it is important to note that leaf level measurements alone may not be applicable for whole canopy or field level remote sensing. Leaf level reflectance data likely does not capture the variations caused by canopy structure, shading, soil reflectance, and other noise that would be present in an image taken above a field. Therefore, leaf and canopy level measurements may both be useful for analysis, but leaf level measurements may not be applicable to the canopy level and vice versa (Hueni et al., 2019). Care should be taken to standardize practices to eliminate the variability observed by the sensor when held at different angles and distances from the plant. Because leaf level measurements are not as affected by some of the primary canopy level issues, these measurements may be considered as the most readily distinguishable. Therefore, considering the effects of canopy structure, illumination, background, sensor view angle, and sensor altitude may render some disorders indistinguishable when observed at the canopy or field level.

Several nutrient deficiencies share similar absorption features, adding another factor contributing to the difficulty of distinguishing specific nutrient disorders (Hueni et al., 2019; Suárez and Berni, 2012). A primary concern for distinguishing among multiple symptoms is whether the plant is exhibiting one or more symptoms on a single leaf. If more than one symptom is expressed, their interactions may limit the success of sensor-based discrimination;

however, it may be possible to eliminate some potential stressors because plants are not exhibiting the associated reflectance characteristics (Adams et al., 2000b). A priori knowledge of soil physical and chemical properties within a field may also help to narrow the potential stressors (Adams et al., 2000b). For instance, if prior soil tests indicate that a field is high in K, it would be less likely that observed symptoms are due to a K deficiency. However, soil test results are not always an accurate predictor of foliar nutrient status, making direct measurements of foliar symptoms highly valuable for diagnostic purposes (Rustioni et al., 2018).

Accurate detection of nutrient deficiencies via spectral sensors is of significant interest, but sensors offer more than symptom detection. With adequate spatial resolution comes the opportunity to map estimated nutrient status throughout a field in order to apply fertilizers only when and where necessary (Daughtry et al., 2000). This type of site-specific precision management can avoid nutrient loss from overapplication while ensuring nutrient sufficiency and maintaining crop health (Daughtry et al., 2000). Over time, this type of precision management can significantly enhance crop uniformity and yield, enabling growers to optimize production. It is apparent that hyperspectral remote sensing can be used to develop a comprehensive nutrient management program as technology and our knowledge of spectral data analysis continue to advance. Therefore, plant scientists interested in hyperspectral remote sensing must develop an understanding of the relevant data management, manipulation, and analysis methods to conduct successful research with meaningful results.

Pre-Processing Hyperspectral Data

Pre-processing is an essential step to conduct prior to the actual analysis (Narumalani and Merani, 2016). This is especially true for time-series data of images the same subject over time.

Most pre-processing steps aim to make the data more manageable while increasing statistical power. After obtaining hyperspectral data, it is important to first conduct a visual analysis to ensure the image is of reasonable quality and to identify any potential errors due to atmospheric noise or sensor malfunctions (Narumalani and Merani, 2016). Next, one should randomly sample pixels and inspect histograms to ensure values appear accurate across spectra. Preliminary univariate and multivariate statistics can also be calculated to investigate data quality (Narumalani and Merani, 2016). Spatial pre-processing enables images to be masked to the same spatial extent and can remove unnecessary background data (i.e., soil, mulch, weeds) (Ferrari et al., 2013). Examples of spatial pre-processing methods include binning, cropping, masking, and morphological operations (Mobaraki and Amigo, 2018). These processes help to eliminate any major differences among images due to factors such as soil moisture, atmospheric water vapor, or sun angle.

Another initial step is to decrease the number of variables in the dataset, a process referred to as dimensionality reduction (Bajwa et al., 2019). For hyperspectral remote sensing, the dimensionality can be considered equal to the number of bands being measured. Hyperspectral sensors with hundreds of bands exhibit high dimensionality, which leads to a sparsity of data that limits statistical power. This phenomenon is commonly referred to as the curse of dimensionality (Bajwa et al., 2019). With increasing dimensionality comes an exponential increase in the amount of data required to derive statistically significant results (Bajwa et al., 2019; Thenkabail et al., 2019). High dimensionality may also lead to overfitting of statistical models (Thenkabail et al., 2000). Due to the nature of narrow bands, high correlation is often observed among neighboring bands (Thenkabail et al., 2019). This correlation, referred to as multicollinearity, leads to high levels of redundancy, meaning many bands will convey similar

information regarding observed variability. Dimensionality reduction attempts to eliminate redundancy while maintaining data that explain a high degree of the variability (Thenkabail et al., 2019).

Another goal of dimensionality reduction is simply to reduce the size of hyperspectral datasets from a computational standpoint. Some hyperspectral sensors have the potential to create hundreds of gigabytes, petabytes, or exabytes worth of data in a short period of time (Bajwa et al., 2019). This can become overwhelming and infeasible given the vast amount of hard drive space and processing power that these quantities of data require to store and analyze (Bajwa et al., 2019). If users have adequate computational equipment, they may still face issues with data transfer. The large file sizes are a significant obstacle for hyperspectral data users. These issues will have less impact as technology advances, but the immense quantities of data will continue to plague the field of hyperspectral remote sensing for the foreseeable future.

For plant sciences, most hyperspectral data analyses aim to determine the optimal bands or band combinations for distinguishing among various vegetation types and quantifying particular characteristics. The ultimate goal is to use the minimum number of explanatory variables while maximizing model accuracy and computational efficiency (Bajwa et al., 2019). Numerous supervised and unsupervised analysis methods are commonly used. Supervised methods require user knowledge or training datasets to label features, while unsupervised methods attempt to find patterns in nonlabelled data (Bajwa et al., 2019). From a plant nutrition perspective, one must first identify and select or extract a feature, for instance, the band reflectance values from a leaf or plant of known nutrient status. Features refer to the individual bands or transformed data derived from the original data (Bajwa et al., 2019). Hyperspectral data analysis often involves data transformation to reduce collinearity and other issues associated with

the raw data (Bajwa et al., 2019; Thorp et al., 2017). Some feature selection and extraction methods include principal component analysis (PCA) (Martel et al., 2018), wavelet decomposition (Wang et al., 2018), and discriminant analysis. Following feature selection, the next step is to extract the data that accounts for the most variability observed among features (Bajwa et al., 2019). Data extraction methods include clustering, regression, discriminant analysis, and maximum likelihood classification (Bajwa et al., 2019). Once dimensionality is reduced and the data of interest is extracted, one may then use this data to develop models or vegetation indices (VIs) with the intent of nutrient status determination (Bajwa et al., 2019; Pu, 2017b). Many spectral indices exist that attempt to quantify phenomena using some ratio of two or more selected bands (Thenkabail et al., 2019).

Principal components analysis is one of the most popular transformations used to select optimal data for modeling biophysical and biochemical phenomena, while eliminating redundancy (Ferrari et al., 2013). The reduction in dimensionality also reduces the computational power required for analysis (Rodarmel and Shan, 2002; Thenkabail et al., 2019). Because PCA transforms the data, one cannot simply determine which individual bands account for maximum variability, but instead, the principal components (PCs) consist of various linear band combinations that are not readily interpreted (Bajwa et al., 2019). Further calculation allows users to determine the proportion each band contributes to each PC (Narumalani and Merani, 2016). Selected PCs can be considered independent variables that may be regressed against specific response variables (Thorp et al., 2017). The PCs are selected in descending order of variability, with only a few (< 5 to 10) accounting for most of the variability (Rodarmel and Shan, 2002). Additional PCs typically do little to contribute to the explained variability and instead contribute primarily to noise. However, the reduction in bands may eliminate

wavelengths indicating subtle differences in the phenomena of interest (Bajwa et al., 2019). Rodarmel and Shan (2002) report 70 to 80% classification accuracy when using just 10 to 20% of the bands originally measured. In contrast, Cheriyyadat and Bruce (2003) report PCA as sound methodology for data compression but state that it may be suboptimal to use with image classification. Thus, use of PCA should be carefully considered when conducting hyperspectral data analysis.

The correlation of each band in relation to one another can be used to eliminate redundancy as well (Bajwa et al., 2019). Correlation coefficients provide a measure for the covariance of each band combination, with higher absolute values indicating higher levels of redundancy (Bajwa et al., 2019; Narumalani and Merani, 2016). In these instances, one of the two highly correlated bands may be eliminated from further analysis, thus reducing dimensionality (Bajwa et al., 2019). Band selection may also be achieved using correlation when bands are highly correlated to a particular characteristic (Bajwa et al., 2019). For plant nutrition, this characteristic could be foliar nutrient concentrations, for instance.

First and second-order derivative spectra (Figure 1.3) are often calculated for analysis instead of or in conjunction with raw reflectance data (Abdel-Rahman et al., 2010; Thorp et al., 2017). A benefit of using derivatives is that it enables one to analyze the degree of change or slope at various points in the spectra (Abdel-Rahman et al., 2010; Thorp et al., 2017). For instance, the red-edge is a common indicator of plant health based on the rapid shift from low reflectance in the red to high reflectance in the NIR, between 680 and 750 nm (Filella and Penuelas, 1994; Gitelson et al., 1996; Thorp et al., 2017). Healthy plants typically exhibit a greater rate of change in the red-edge than do stressed plants (Abdel-Rahman et al., 2010). Derivatives also help to locate inflection points where the spectrum changes direction (Liew et

al., 2008). These features can be as useful if not more useful than raw reflectance data for hyperspectral data analysis (Abdel-Rahman et al., 2010), and may demonstrate patterns not readily observed in raw reflectance data (Thorp et al., 2017).

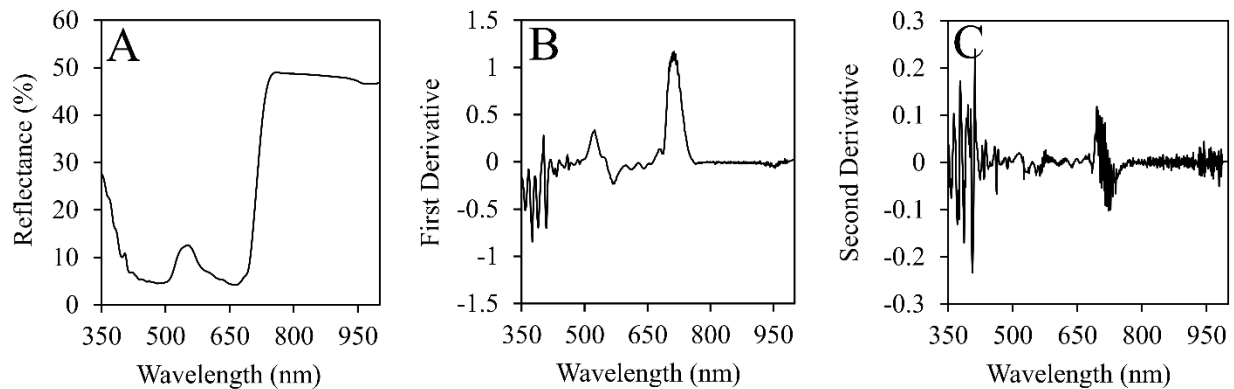


Figure 1.3. Average (A) foliar spectral reflectance measured from healthy tobacco (*Nicotiana tabacum*) leaves (J. Henry, unpublished data) with corresponding (B) first and (C) second-order derivative spectra. Derivatives demonstrate the rate of change between each pair of adjacent wavelengths.

One of the main environmental factors that contributes to noise and distorts spectral measurements is the presence of water (Liew et al., 2008). Different moisture levels in the atmosphere, in the plant, and on the surface of the plant can significantly alter spectral measurements. Several water absorption features can be found throughout the spectrum but especially in the short-wave infrared (SWIR) region. For instance, water absorbs significant quantities of EMR in the ranges of 1355 to 1450 nm and 1800 to 1950 nm (Abdel-Rahman et al., 2010; Kumar et al., 2002; Liew et al., 2008). These bands may be important for detecting water related stress such as drought, but they may also interfere with the results of analyses

investigating nutrient stress. Therefore, it is important to carefully consider removing these bands from the analysis depending on the desired application (Abdel-Rahman et al., 2010).

Another issue often faced by researchers is whether to use all data in a hyperspectral image or to average spectral values from pixels belonging to the same class in order to reduce computation time and complexity. This may result in a loss of significant variability that should be accounted for in models developed with the data. It also removes much of the spatial variation, eliminating the relationships of pixels in relation to one another (Ferrari et al., 2013). However, Dennison and Roberts (2003) report that confusion among spectrally similar classes may be overcome by averaging values by user-defined polygons. The data selected for analysis can affect the results, and therefore, care should be taken to thoroughly plan analysis techniques before conducting experiments. For these reasons, it is essential that hyperspectral remote sensing analysis methods in agriculture be thoroughly defined and standardized for further research and commercial applications. As researchers analyze hyperspectral data, they should aim to do so in a way that makes sense given the application (Thorp et al., 2017). The numerous transformations and analysis methods currently used can easily yield results that are statistically significant but may not be useful from an applied perspective.

Hyperspectral Data Analysis Methods

Modeling and classification are the two primary routes considered after image pre-processing and initial feature selection results (Bajwa et al., 2019). Several types of regression are used to develop empirical models for quantitative variables such as foliar nutrient content (Bajwa et al., 2019). Thus, such models can be used to predict foliar nutrient concentrations based on reflectance (Mobaraki and Amigo, 2018). Only a portion of the original data should be

used for model development, as further data is required to calibrate and validate the resulting model (Ferrari et al., 2013). Keeping test data aside to validate a model is essential for ensuring model accuracy (Griffith and Anderson, 2019). Leave-one-out cross validation is commonly used in the development of narrow-band and hyperspectral data models (Abdel-Rahman et al., 2010). Multivariate regression can be used in hyperspectral data analysis, but collinearity among raw bands can cause modeling error (Thorp et al., 2017). Therefore, multivariate regression is better suited for modeling PCs, VIs, or other transformed data (Bajwa et al., 2019).

Partial least squares regression (PLSR) is one of the more commonly used methods in hyperspectral plant analysis (Bajwa et al., 2019; Thenkabail et al., 2019; Thorp et al., 2017). Similar to PCs, Partial least squares (PLS) factors are derived from transformations of the original data intended to maximize covariance between the factors and the dependent variables (Bajwa et al., 2019). One or more dependent variables can be regressed using the PLS factors (Bajwa et al., 2019). A negative issue associated with PLSR is that it does not necessarily create a subset of optimal spectral features, and instead may use the full spectrum for model development (Thorp et al., 2017). This may limit the identification of the fewest bands necessary for symptom discrimination and prevent the development of targeted, lower-cost sensor systems. Still, PLSR often results in statistically sound models with which various biophysical and biochemical traits may be estimated.

Recent studies demonstrate the efficacy of using PLSR in conjunction with genetic algorithms for optimal band selection (Thorp et al., 2017). Genetic algorithms simulate natural selection by iterating “generations” of individuals with a “chromosome” consisting of a specific number of “genes” which each correspond to a spectral feature. The individuals are then selected based on a fitness score associated with how well the spectra can explain the problem; that is,

finding the optimal features to explain the variability observed in a particular spectral response. The fittest individuals are then used to develop the next generation and so on. This process continues until an optimal solution is found, a specific number of generations have passed, or the iterative process plateaus so no further improvements can be made. This offers an advanced data mining opportunity to find useful spectral features with which models estimating various vegetation characteristics may be developed (Thorp et al., 2017).

Vegetation indices are mathematical ratios or formulas used to model biophysical and biochemical characteristics of plants (Liew et al., 2008; Thenkabail et al., 2019). These formulas vary in complexity depending on the bands used for VI development and how the relationships among bands can be manipulated to estimate a particular characteristic (Narumalani and Merani, 2016). Many VIs have been developed from broad-band multispectral sensors over the course of several decades, but hyperspectral data enables refinement of existing VIs using more specific narrow bands (Thorp et al., 2017). Hyperspectral narrow-band data also provides potential for the development of thousands of new VIs (Thenkabail et al., 2019). Therefore, determination of optimal bands for a particular phenomenon is essential for the successful implementation of a new index. Vegetation indices may consist of two or more spectral bands and typically seek to exploit specific spectral reflectance differences associated with particular phenomenon (e.g., red absorption and NIR reflectance of chloroplasts). It is typically beneficial to normalize simple ratios to enable accurate comparisons (Thenkabail et al., 2019). Derivative greenness indices are particularly important for sensing plant stress (Thenkabail et al., 2019) by representing the degree of change along the red-edge. Numerous VIs have been developed and published for modeling foliar nutrient concentrations and other plant characteristics (Bajwa et al., 2019; Thorp et al., 2017).

In contrast to modeling, classification methods are used for analysis of categorical variables (Bajwa et al., 2019). For instance, classification methods can be used to identify various nutrient disorder symptoms. Image classification is commonly used in multispectral image analysis but may also be utilized with hyperspectral imagery. Classification may be supervised or unsupervised and often use algorithms based on maximum-likelihood methods (Narumalani and Merani, 2016). Supervised classification requires the provision of labeled “training data” that are used to develop discriminatory features. Clustering is a useful method for hyperspectral data analysis that works by grouping observations based on similarities in distance (Bajwa et al., 2019). Numerous methods of measuring distance are available, including Euclidean and Mahalanobis distances. These clustering techniques can distinguish patterns in the distribution of similar pixels (Mobaraki and Amigo, 2018).

Discriminant analysis is a classification method that involves modeling based on multiple variables (Thenkabail et al., 2019). The analysis attempts to determine which explanatory variables or features are optimal for separating among two or more unique classes (Bajwa et al., 2019). There are several frequently used methods including canonical, Fisher’s ratio, Kernel Fisher, and stepwise discriminant analysis (Bajwa et al., 2019; Thenkabail et al., 2019); however, Fisher’s ratio is most commonly used (Bajwa et al., 2019). Dimensionality reduction techniques are typically applied before discriminant analysis (Bajwa et al., 2019). An alternative way to reduce the number of features used is to run stepwise discriminant analysis, where each variable is selected or rejected from the model individually following an F-test for significance (Bajwa et al., 2019). Regardless of the specific method used, the ultimate goal of discriminant analysis is to separate clusters of similar measurements. For instance, discriminant analysis can be used to distinguish among multiple different nutrient deficiencies or multiple severities of a single

deficiency. However, it is important to consider that discriminant analysis techniques are not well suited for distinguishing among subtle differences (Bajwa et al., 2019).

Hyperspectral Applications in Plant Nutrition

Nitrogen is typically considered the primary nutrient of interest due to the relatively high concentrations required by plants and because most common N forms are readily leached and volatilized from the root zone (Mitra, 2017; Stroppiana et al., 2019). In fact, it is estimated that only half of the N applied agronomically is used by the crop while the rest is lost to the environment (Hawkesford et al., 2012; Sylvester-Bradley and Kindred, 2009). Much of the N is lost in the form of nitrate which can accumulate and pollute groundwater (Inoue et al., 2012). As a result, N deficiency is one of the most commonly observed nutrient disorders in crops.

Scouting for N deficiency symptoms using traditional scouting methods is very time consuming and can be difficult to feasibly accomplish in large scale commercial production settings.

Therefore, rapid, automated, and accurate N deficiency identification using sensors has become a topic of significant interest for estimating crop N status (Thorp et al., 2017). Spatially estimated N status may be used to optimize N application timing and quantities based on localized crop need (Thorp et al., 2017).

Aerial and ground-based spectral sensors have been used for several decades for N estimation (Stroppiana et al., 2019), but other studies have investigated the spectral response of other nutrient deficiencies in a variety of species (Abdel-Rahman et al., 2010; Adams et al., 2000a; Li et al., 2018a; Mahajan et al., 2017; Suárez and Berni, 2012; Thorp et al., 2017; Zhang et al., 2013). In sugarcane (*Saccharum officinarum*), Abdel-Rahman et al. (2010) reported significant correlations to foliar N concentration using wavelengths between 418 to 481 nm, 551

to 608 nm, 697 to 749 nm as well as 1266, 2142, and 2243 nm. These values demonstrate the importance of reflection in the visible and red-edge spectra for N estimation. Thorp et al. (2017) studied spectral reflectance from durum wheat (*Triticum durum*) grown with N fertilizer treatments ranging from 0 to 403 kg ha⁻¹. They compared broad-band multispectral sensors with a 512-band radiometer using PLSR to analyze reflectance as well as first and second derivative spectra (Thorp et al., 2017). A genetic algorithm was also implemented to determine the most important spectral features. Thorp et al. (2017) found that narrow-band N estimation models were superior to those developed with multispectral broad-band data. Using PLSR in conjunction with the genetic algorithm led to superior N estimates than PLSR alone (Thorp et al., 2017). The best models (lowest RMSE) for N content used a combination of PLSR, the genetic algorithm, reflectance data, and derivative spectra (Thorp et al., 2017).

Li et al. (2018a) studied hyperspectral reflectance for estimating N in upper, middle, and lower oilseed rape (*Brassica napus*) plants. They used PLSR and reported optimal wavelengths of 437, 565, 667, 724, 993, 1084, and 1189 nm for upper leaves, 423, 570, 598, 659, 725, and 877 nm for middle leaves, and 420, 573, 597, 667, and 718 nm for lower leaves (Li et al., 2018a). Li et al. (2018b) also used PLSR to model and predict foliar N and P concentrations in oilseed rape. They compared PLSR with other data transformations such as first derivatives and continuum removal and found that PLSR with first derivatives was most effective. Optimal wavelengths selected for N were 445, 556, 657, 764, 985, 1082, and 1994 nm while those selected for P included 755, 832, 891, 999, 1196, and 1267 nm (Li et al., 2018b). Zhang et al. (2013) investigated the spectral response of oilseed rape to N, P, and K deficiencies using PLSR. They reported optimal wavelengths of 440, 473, 513, 542, 659, 718, 744, 865, 928, 965, 986, and

1015 nm for N, 468, 522, 698, 721, 817, 967, 979, and 1025 nm for P, and 456, 554, 667, 720, and 1027 nm for K (Zhang et al., 2013).

Fewer studies investigated the spectral reflectance of multiple nutrient deficiencies within a single species, and most importantly, whether the symptoms could be accurately distinguished from one another. A study by Adams et al. (2000b) investigated spectral discrimination of Cu, Fe, Mn, and Zn deficiency symptoms in soybean (*Glycine max* L.). They developed discriminant rules to identify among these deficiencies which help to classify each measurement into a specific deficiency or non-deficient group. Results indicated Cu-deficient leaves were most successfully distinguishable and Mn-deficient leaves were also distinguishable in many cases; however, Fe and Zn deficiencies were more difficult to classify (Adams et al., 2000b). Adams et al. (2000a) suggested that Cu, Fe, and Mn may affect spectral reflectance due to their specific roles in chlorophyll synthesis and electron transport.

A study by Rustioni et al. (2018) reported successful discrimination among N, K, Mg, and Fe deficiencies in grape (*Vitis vinifera*) leaves using hyperspectral reflectance measurements. They used leaves of several maturity levels and recorded reflectance from different areas on the leaf surface (i.e., near veins, between veins, and near margins). Symptomatic leaf reflectance data were transformed and normalized before being subtracted from control spectra (Rustioni et al., 2018). Each of the four nutrient deficiencies resulted in symptoms of chlorosis that were distinguishable based on the reflectance values associated with various pigments. For instance, the presence of chlorophylls *a* and *b*, carotenoids, and anthocyanins could be distinguished using bands near 678, 650, 495, and 550 nm (Rustioni et al., 2018).

Many studies demonstrate spectral patterns exhibited by specific stressors in controlled environments (Abdel-Rahman et al., 2008); however, it is important to consider that growth

habits are significantly influenced by their environment. For instance, the glass panes of a greenhouse will reflect, refract, and transmit light of specific wavelengths, altering the quantity and quality of light reaching the leaf surface compared to a plant grown in the presence of direct sunlight (Liew et al., 2008). This and other factors in a controlled environment (e.g., substrate, pot size, irrigation frequency) will certainly affect the growth and spectral signature compared to field-grown plants. Therefore, controlled environment studies are good for research purposes, but should not be directly applied to field situations without prior testing.

Certain wavelengths are already associated with plant stress in general and nutrient stress specifically. Many of these bands fall within the red-edge at approximately 700, 720, and 740 nm (Filella and Penuelas, 1994; Gitelson et al., 1996; Thenkabail et al., 2019). Other wavelengths of interest fall in the blue, (375, 466, and 490 nm), green (515, 520, 525, 550, and 575 nm) and red (675 and 682 nm) spectra (Thenkabail et al., 2019). These wavelengths have demonstrated a response to nutrient stress or pigment changes (Pu, 2017b; Thenkabail et al., 2019). Soil-Plant Analysis Development (SPAD) meters emit targeted EMR near 650 and 940 nm and subsequently measure the amount of radiation transmitted through the leaf (Daughtry et al., 2000). The values obtained from these sensors provide a measure of the green (high values) or yellow (low values) coloration exhibited in the foliage (Daughtry et al., 2000). These measurements are based on the premise that they estimate leaf chlorophyll concentrations which in turn correlate to leaf N concentrations.

It is important to note that spectral differences exist not only among species, but also by growth stage (Cheng et al., 2019). Furthermore, spectral differences may be observed among species of the same cultivar or variety. This is especially true for ornamental plants which can vary significantly in natural pigmentation. Fig. 4 demonstrates this scenario with three cultivars

of ornamental sweet potato (*Ipomoea batatas*). Healthy leaves from these cultivars can be green, purple, or variegated, and these types of color differences are not uncommon. Therefore, estimating nutrient concentrations or discriminating among nutrient deficiencies and other plant health issues may require spectral model development at the cultivar level. Of particular note is that the dark purple leaves of ‘Illusion Midnight Lace’ exhibited nearly uniform reflectance throughout the VIS, lacking the peak in the green-yellow region typically observed in green leaves. It is likely that a model developed using one of the cultivars in fig. 4 would not be applicable to the other cultivars. This issue is less likely to be an issue for agronomic crops but remains an important consideration.

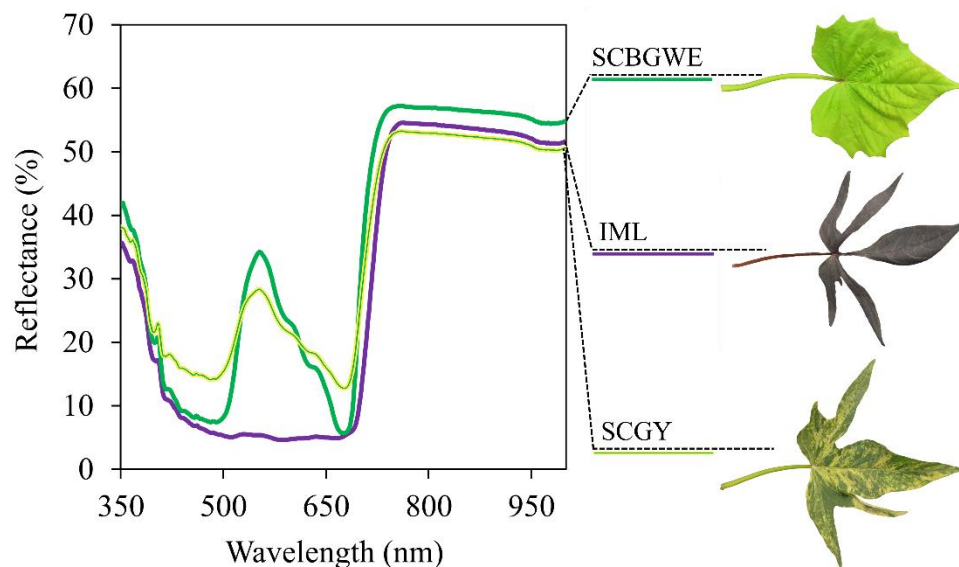


Figure 1.4. Spectral signatures of three ornamental sweet potato (*Ipomoea batatas*) cultivars that each exhibit different natural coloration (J. Henry, unpublished data). The cultivars are ‘Sweet Caroline Bewitched Green with Envy’ (SCBGWE), ‘Illusion Midnight Lace’ (IML), and ‘Sweet Caroline Green Yellow’ (SCGY).

Classifying nutrient deficiencies based on spectral reflectance is also of interest.

Differences among spectra can be quite indicative of nutrient stress. For instance, Fig. 5 demonstrates how visible light is more highly reflected by N-deficient tobacco plants than the asymptomatic control. This also demonstrates how the red-edge of N-deficient spectra shift toward shorter wavelengths, and how the proportion of red and blue light absorption in chlorophyll changes (Figure 1.5). It is apparent that N-deficient foliage utilizes less red light compared to blue light for photosynthesis due to the higher reflectance in the red (Figure 1.5).

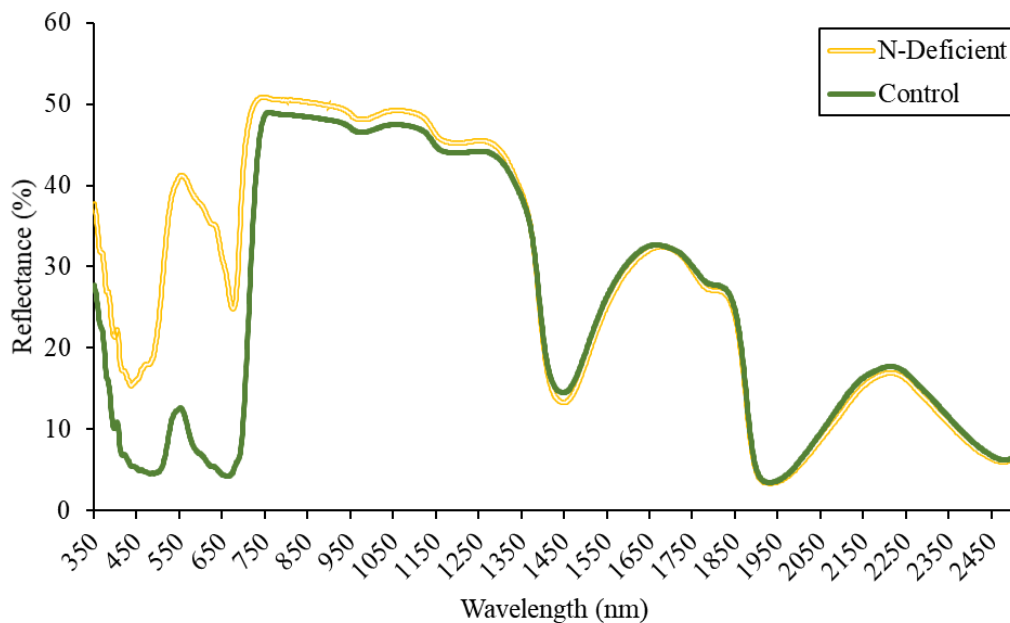


Figure 1.5. Average spectra from N-deficient tobacco (*Nicotiana tabacum*) foliage ($n = 70$) compared to that of the asymptomatic control ($n = 325$) (J. Henry, unpublished data).

Available Analysis Software

Many options are available for conducting hyperspectral image analysis. Programs and coding languages commonly implemented include Matlab, Python, and R (Mobaraki and Amigo,

2018; Python Software Foundation, 2019; R Core Team, 2019; The MathWorks, Inc., 2019).

Within these programs, various scripts, modules, and toolboxes have been developed specifically for hyperspectral data analysis. Some options are considerably more user-friendly than others, with some requiring coding in a command-line interface and others providing a “point-and-click” graphical user interface (GUI). An additional consideration is that some options are freely available (i.e., open source) while others require a license.

Mobaraki and Amigo (2018) developed a hyperspectral image analysis toolbox for Matlab (license required) called HYPER-Tools. This toolbox allows users to analyze their imagery using a simple and well-organized GUI that employs a series of windows with point-and-click options (Mobaraki and Amigo, 2018). HYPER-Tools contains numerous pre-processing and analysis methods that utilize pattern recognition, clustering, classification, and regression techniques (Mobaraki and Amigo, 2018). Although HYPER-Tools was not created specifically for agricultural or biological applications, it provides most of the commonly used analysis methods discussed earlier including PCA, DA, and PLSR (Mobaraki and Amigo, 2018). Additionally, HYPER-Tools automatically graphs spectral signatures, PCA loadings and scores, cluster statistics, and more. HYPER-Tools offers a suite of analysis tools in a way that is easy to understand and implement, making it an excellent option for those with limited coding experience.

The R Project for Statistical Computing offers numerous basic and advanced packages that can be used to analyze and visualize hyperspectral data. For instance, the “pls” package can be used to conduct PLSR (Thorp et al., 2017). The ‘plantspec’ package in R focuses on the use of VIS-NIR data for modeling the elemental composition of plants with an emphasis on PLSR (Griffith and Anderson, 2019). Griffith and Anderson (2019) suggest that proper model

development and calibration using this package provides an inexpensive alternative to traditional chemical quantification methods such as inductively coupled plasma optical emission spectrometry (ICP-OES). Furthermore, this package enables users to calibrate models with a mixture of their own data and a large sample dataset added by the package developers (Griffith and Anderson, 2019). Other similar R packages include ‘ChemoSpec’, and ‘chemometrics’. Another package called ‘Hyperspec’ focuses on hyperspectral data analysis, while a newer package called ‘hsdar’ was developed specifically for pre-processing, feature extraction, classification, and regression of hyperspectral vegetation data (Lehnert et al., 2019).

Similar to R, Python offers the ability to code for numerous relevant statistical procedures. Scripts have been developed for interpolation (Thorp et al., 2017), derivative calculation (Thorp et al., 2017), and spectral data simulation (Thorp et al., 2015). Spectral Python (SPy; <https://www.spectralpython.net>) is a module available in Python for working with hyperspectral imagery. It allows users to manipulate, transform, and classify data, create visuals, and apply spectral algorithms. Regardless of the desired application, numerous options are available on various platforms. The software options listed here should certainly provide researchers with a good starting point to aid in their pursuit of hyperspectral data analysis.

Conclusions

The vast quantities of data obtained from hyperspectral sensors are limiting to their common usage in commercial agricultural production. Time of computational processing, data storage, and data analysis are major considerations that must be addressed in the future. Future research should focus on optimal methods of determining spectral features (e.g. bands and band combinations) helpful for the detection of various plant stressors (Thenkabail et al., 2002). These

features could be used to develop multispectral sensors that are made to monitor specific crop-stressor pairs. Over time, research will elucidate which bands are most important and which are redundant for various agricultural applications (Thenkabail et al., 2019). This will greatly increase the speed at which useful information is extracted from hyperspectral data and implemented in commercial production settings. However, collaboration among members of the scientific, sensor manufacturing, and governing communities is required to achieve the advancements necessary for commercial implementation (Ortenberg, 2019).

Ultimately, the ability to accurately quantify crop nutrient concentrations and categorize deficiencies before symptoms are visible can avoid fertilizer waste by applying nutrients only where and when they are needed. This goal appears achievable but requires further research on numerous plant species with which to develop models. Furthermore, future model development requires a certain level of standardization. The community of plant scientists studying hyperspectral reflectance data must come to an agreement as to which methods are most acceptable so that future studies may be more easily integrated into the current body of knowledge. Additionally, there is a significant need for researchers to improve the methods sections in peer-reviewed publications, as many papers lack the detail necessary to be reproducible. Numerous challenges must be overcome as hyperspectral remote sensing becomes more widely utilized; however, the future appears promising.

Acknowledgements

The authors would like to thank the North Carolina Tobacco Foundation for funding this review.

References

- Abdel-Rahman, E.M., F.B. Ahmed, and M. van den Berg. 2008. Imaging spectroscopy for estimating sugarcane leaf nitrogen concentration. In: C.M.U. Neale, M. Owe, and G. D'Urso, editors, Proceedings SPIE 7104, Remote Sensing for Agriculture, Ecosystems, and Hydrology X, Cardiff, United Kingdom. p. V1–V12.
- Abdel-Rahman, E.M., F.B. Ahmed, and M. van den Berg. 2010. Estimation of sugarcane leaf nitrogen concentration using in situ spectrometry. *Int. J. Appl. Earth Observation Geoinformation* 12S:S52–S57.
- Abdullahi, H.S., F. Mahieddine, and R.E. Sheriff. 2015. Technology impact on agricultural productivity: A review of precision agriculture using unmanned aerial vehicles. In: P. Pillai, Y.F. Hu, I. Otung, and G. Giambene, editors, *Wireless and Satellite Systems*, 7th International Conference, WiSATS 2015, Bradford, UK, July 6–7, 2015, Revised Selected Papers. Springer, Cham, Switzerland. p. 388–400.
- Adams, J.B, M.O. Smith, and A.R. Gillespie. 1993. Imaging spectroscopy: Interpretation based on spectral mixture analysis. In: C.M. Pieters and P.A.J. Englert, editors, *Remote Geochemical Analysis: Elemental and Mineralogical Composition*. Pres Syndicate of University of Cambridge, Cambridge, England. p. 145–166.
- Adams, M.L., W.A. Norvell, W.D. Philpot, and J.H. Peverly. 2000a. Spectral detection of micronutrient deficiency in 'Bragg' soybean. *Agron. J.* 92:261–268.
- Adams, M.L., W.A. Norvell, W.D. Philpot, and J.H. Peverly. 2000b. Toward the discrimination of manganese, zinc, copper, and iron deficiency in 'Bragg' soybean using spectral detection methods. *Agron. J.* 92:268–274.

- Amigo, J.M., H. Babamoradi, and S. Elcoroaristizabal. 2015. Hyperspectral image analysis. A tutorial. *Anal. Chim. Acta* 896:35–51.
- Bajwa, S.G., Y. Zhang, and A. Shirzadifar. 2019. Hyperspectral image data mining. In: P.S. Thenkabail et al., editors, *Hyperspectral Remote Sensing of Vegetation Volume One: Fundamentals, Sensor Systems, Spectral Libraries, and Data Mining for Vegetation*. 2nd ed. CRC Press, Boca Raton, FL. p. 273–302.
- Behmann, J., J. Streinrücken, and L. Plümer. 2014. Detection of early plant stress responses in hyperspectral images. *ISPRS J. Photogramm. Remote Sens.* 93:98–111.
- Broadley, M., P. Brown, I. Cakmak, J.F. Ma, Z. Rengel, and F. Zhao. 2012. Beneficial elements. In: P. Marschner, editor, *Marschner's Mineral Nutrition of Higher Plants*. 3rd ed. Academic Press, London, UK. p. 249–269.
- Cheng, T., Y. Zhu, D. Li, X. Yao, and K. Zhou. 2019. Hyperspectral remote sensing of leaf nitrogen concentration in cereal crops. In: P.S. Thenkabail et al., editors, *Hyperspectral Remote Sensing of Vegetation Volume Two: Hyperspectral indices and image classifications for agriculture and vegetation*. 2nd ed. CRC Press, Boca Raton, FL. p. 163–182.
- Cheriyadat, A., and L.M. Bruce. 2003. Why principal component analysis is not an appropriate feature extraction method for hyperspectral data. In: 2003 IEEE International Geoscience and Remote Sensing Symposium Proceedings, 21–25 July 2003. IEEE, Toulouse, France. p. 3420–3422.
- Daughtry, C.S.T., C.L. Walthall, M.S. Kim, E. Brown de Colstoun, and J.E. McMurtrey III. 2000. Estimating corn leaf chlorophyll concentration from leaf and canopy reflectance. *Remote Sens. Environ.* 74:229–239.

- Delloye, C., M. Weiss, and P. Defourny. 2018. Retrieval of the canopy chlorophyll content from sentinel-2 spectral bands to estimate nitrogen uptake in intensive winter wheat cropping systems. *Remote Sens. Environ.* 216:245–261.
- Dennison, P.E., and D.A. Roberts. 2003. Endmember selection for multiple endmember spectral mixture analysis using endmember average RMSE. *Remote Sens. Environ.* 87:123–135.
- Engels, C., E. Kirkby, and P. White. 2012. Mineral nutrition, yield and source-sink relationships. In: P. Marschner, editor, *Marschner's Mineral Nutrition of Higher Plants*. 2nd ed. Academic Press, London, UK. p. 85–133.
- Ferrari, C., G. Foca, and A. Ulrici. 2013. Handling large datasets of hyperspectral images: Reducing data size without loss of useful information. *Anal. Chim. Acta* 802:29–39.
- Filella, I., and J. Penuelas. 1994. The red edge position and shape as indicators of plant chlorophyll content, biomass and hydric status. *Int. J. Remote Sens.* 15:1459–1470.
- Gitelson, A.A., M.N. Merzlyak, and H.K. Lichtenthaler. 1996. Detection of red edge position and chlorophyll content by reflectance measurements near 700 nm. *J. Plant Physiol.* 148:501–508.
- Griffith, D.M., and T.M. Anderson. 2019. The 'plantspec' R package: A tool for spectral analysis of plant stoichiometry. *Methods Ecol. Evolution* 10:673–679.
- Hawkesford, M., W. Horst, T. Kichey, H. Lambers, J. Schjoerring, I.S. Møller, and P. White. 2012. Functions of macronutrients. In: P. Marschner, editor, *Marschner's Mineral Nutrition of Higher Plants*. 2nd ed. Academic Press, London, UK. p. 135–189.
- Henry, J., P. Perkins-Veazie, I. McCall, and B. Whipker. 2019. Restricted phosphorus fertilization increases the betacyanin concentration and red foliage coloration of *alternanthera*. *J. Amer. Soc. Hort. Sci.* 144:264–273.

- Huang, Y., S.J. Thomson, Y. Lan, and S.J. Maas. 2010. Multispectral imaging systems for airborne remote sensing to support agricultural production management. *Int. J. Agric. Biol. Eng.* 3:50–62.
- Hueni, A., L. Suárez, L.A. Chisholm, and A. Held. 2019. The use of spectral databases for remote sensing of agricultural crops. In: P.S. Thenkabail et al., editors, *Hyperspectral Remote Sensing of Vegetation Volume One: Fundamentals, Sensor Systems, Spectral Libraries, and Data Mining for Vegetation*. 2nd ed. CRC Press, Boca Raton, FL. p. 165–185.
- Inoue Y., E. Sakaiya, Y. Zhu, and W. Takahashi. 2012. Diagnostic mapping of canopy nitrogen content in rice based on hyperspectral measurements. *Remote Sens. Environ.* 126:210–221.
- Jensen, J.R. 2007. *Remote sensing of the environment: An earth resource perspective*. 2nd ed. Pearson Prentice Hall, Upper Saddle River, NJ.
- Jin, J., and Q. Wang. 2018. Informative bands used by efficient hyperspectral indices to predict leaf biochemical contents are determined by their relative absorptions. *Intl. J. Appl. Earth Observation Geoinformation* 73:616–626.
- Kumar, L., K. Schmidt, S. Dury, and A. Skidmore. 2002. Imaging spectrometry and vegetation science. In: F.D. van der Meer and S.M. de Jong, editors, *Image Spectrometry: Basic Principles and Prospective Applications, Volume 4*. Springer, Dordrecht, The Netherlands. p. 111–155.
- Lehnert, L.W., H. Meyer, W.A. Obermeier, B. Silva, B. Regeling, B. Thies, and J. Bendix. 2019. Hyperspectral data analysis in R: The hsdar package. *J. Stat. Software* 89(12):1–23.

- Li, F., D.L. Jupp, M. Paget, P.R. Briggs, M. Thankappan, A. Lewis, and A. Held. 2017. Improving BRDF normalisation for landsat data using statistical relationships between MODIS BRDF shape and vegetation structure in the australian continent. *Remote Sens. Environ.* 195:275–296.
- Li, L., B. Jákli, P. Lu, T. Ren, J. Ming, S. Liu, S. Wang, and J. Lu. 2018a. Assessing leaf nitrogen concentration of winter oilseed rape with canopy hyperspectral technique considering a non-uniform vertical nitrogen distribution. *Ind. Crops Products* 116:1–14.
- Li, L., S. Wang, T. Ren, Q. Wei, J. Ming, J. Li, X. Li, R. Cong, and J. Lu. 2018b. Ability of models with effective wavelengths to monitor nitrogen and phosphorus status of winter oilseed rape leaves using in situ canopy spectroscopy. *Field Crops Res.* 215:173–186.
- Liew, O.W., P.K.J. Chong, B. Li, and A.K. Asundi. 2008. Signature optical cues: Emerging technologies for monitoring plant health. *Sensors* 8:3205–3239.
- Liu, Y., Z. Wang, Q. Sun, A.M. Erb, Z. Li, C.B. Schaaf, X. Zhang, M.O. Román, R.L. Scott, and Q. Zhang. 2017. Evaluation of the VIIRS BRDF, albedo and NBAR products suite and an assessment of continuity with the long term MODIS record. *Remote Sens. Environ.* 201:256–274.
- Mahajan, G., R. Pandey, R. Sahoo, V. Gupta, S. Datta, and D. Kumar. 2017. Monitoring nitrogen, phosphorus and sulphur in hybrid rice (*Oryza sativa* L.) using hyperspectral remote sensing. *Precision Agric.* 18:736–761.
- Martel, E., R. Lazcano, J. López, D. Madroñal, R. Salvador, S. López, E. Juarez, R. Guerra, C. Sanz, and R. Sarmiento. 2018. Implementation of the principal component analysis onto high-performance computer facilities for hyperspectral dimensionality reduction: Results and comparisons. *Remote Sens.* 10(864):1–30.

- Mattupalli, C., M.R. Komp, and C.A. Young. 2017. Integrating geospatial technologies and unmanned aircraft systems into the grower's disease management toolbox. *APS Features*.
- Mitra, G. 2017. Essential plant nutrients and recent concepts about their uptake. In: N. Naeem et al., editors, *Essential Plant Nutrients: Uptake, Use Efficiency, and Management*. Springer, Cham, Switzerland. p. 3–36.
- Mobaraki, N., and J.M. Amigo. 2018. HYPER-Tools. A graphical and user-friendly interface for hyperspectral image analysis. *Chemometrics Intelligent Lab. Syst.* 172:174–187.
- Narumalani, S., and P. Merani. 2016. Digital image processing: A review of the fundamental methods and techniques. In: P.S. Thenkabail, editor, *Remote Sensing Handbook Volume I: Remotely Sensed Data Characterization, Classification, and Accuracies*. CRC Press, Boca Raton, FL. p. 197–217.
- Ortenberg, F. 2019. Hyperspectral sensors characteristics: Airborne, spaceborne, hand-held, and truck-mounted; integration of hyperspectral data with LiDAR. In: P.S. Thenkabail et al., editors, *Hyperspectral Remote Sensing of Vegetation Volume One: Fundamentals, Sensor Systems, Spectral Libraries, and Data Mining for Vegetation*. 2nd ed. CRC Press, Boca Raton, FL. p. 41–70.
- Powell, R.L., D.A. Roberts, P.E. Dennison, and L.L. Hess. 2007. Sub-pixel mapping of urban land cover using multiple endmember spectral mixture analysis: Manaus, Brazil. *Remote Sens. Environ.* 106:253–267.
- Pu, R. 2017. Hyperspectral applications to vegetation. In: Q. Weng, editor, *Hyperspectral Remote Sensing Fundamentals and Practices*. CRC Press Boca Raton, FL. p. 325–388.
- Pu, R. 2017. Overview of hyperspectral remote sensing. In: Q. Weng, editor, *Hyperspectral Remote Sensing Fundamentals and Practices*. CRC Press Boca Raton, FL. p. 1–30.

- Python Software Foundation. 2019. Python language, version 3.7.4. <https://www.python.org>
- R Core Team. 2019. R: A language and environment for statistical computing. R Foundation for Statistical Computing, Vienna, Austria. <https://www.R-project.org/>
- Rodarmel, C., and J. Shan. 2002. Principal component analysis for hyperspectral image classification. *Surveying Land Information Sci.* 62:115–122.
- Römheld, V. 2012. Diagnosis of deficiency and toxicity of nutrients. In: P. Marschner, editor, *Marschner's Mineral Nutrition of Higher Plants*. 2nd ed. Academic Press, London, UK. p. 299–312.
- Roy, D.P., H. Zhang, J. Ju, J.L. Gomez-Dans, P.E. Lewis, C. Schaaf, Q. Sun, J. Li, H. Huang, and V. Kovalsky. 2016. A general method to normalize Landsat reflectance data to nadir BRDF adjusted reflectance. *Remote Sens. Environ.* 176:255–271.
- Rustioni, L., D. Grossi, L. Brancadoro, and O. Failla. 2018. Iron, magnesium, nitrogen and potassium deficiency symptom discrimination by reflectance spectroscopy. *Sci. Hortic.* 241:152–159.
- Stroppiana, D., F. Fava, M. Boschetti, and P.A. Brivio. 2019. Estimation of nitrogen content in herbaceous plants using hyperspectral vegetation indices. In: P.S. Thenkabail et al., editors, *Hyperspectral Remote Sensing of Vegetation Volume Two: Hyperspectral indices and image classifications for agriculture and vegetation*. 2nd ed. CRC Press, Boca Raton, FL. p. 201–225.
- Suárez, L., and J.A.J. Berni. 2012. Spectral response of citrus and their application to nutrient and water constraints diagnosis. In: A.K. Srivastava, editor, *Advances in Citrus Nutrition*. Springer, Dordrecht, The Netherlands. p. 125–141.

- Sylvester-Bradley, R., and D.R. Kindred. 2009. Analysing nitrogen responses of cereals to prioritize routes to the improvement of nitrogen use efficiency. *J. Exp. Bot.* 60:1939–1951.
- The MathWorks, Inc. 2019. MATLAB Release 2019a. The MathWorks, Inc., Natick, MA.
- Thenkabail, P.S., J.G. Lyon, and A. Huete. 2019. Advances in hyperspectral remote sensing of vegetation and agricultural crops. In: P.S. Thenkabail et al., editors, *Hyperspectral Remote Sensing of Vegetation Volume One: Fundamentals, Sensor Systems, Spectral Libraries, and Data Mining for Vegetation*. 2nd ed. CRC Press, Boca Raton, FL. p. 3–37.
- Thenkabail, P.S., R.B. Smith, and E. De Pauw. 2000. Hyperspectral vegetation indices and their relationships with agricultural crop characteristics. *Remote Sens. Environ.* 71:158–182.
- Thenkabail, P.S., R.B. Smith, and E. De Pauw. 2002. Evaluation of narrowband and broadband vegetation indices for determining optimal hyperspectral wavebands for agricultural crop characterization. *Photogramm. Eng. Remote Sens.* 68:607–622.
- Thorp, K.R., G. Wan, K.F. Bronson, M. Badaruddin, and J. Mon. 2017. Hyperspectral data mining to identify relevant canopy spectral features for estimating durum wheat growth, nitrogen status, and grain yield. *Comput. Electron. Agric.* 136:1–12.
- Thorp, K.R., M. Gore, P. Andrade-Sanchez, A. Carmo-Silva, S. Welch, J. White, and A.N. French. 2015. Proximal hyperspectral sensing and data analysis approaches for field-based plant phenomics. *Comput. Electron. Agric.* 118:225–236.
- US Geological Survey. 2016. Landsat—Earth observation satellites. Fact Sheet 2015–3081, US Geological Survey (USGS), Washington, DC. p. 4.

- Wang, J., Y. Chen, F. Chen, T. Shi, and G. Wu. 2018. Wavelet-based coupling of leaf and canopy reflectance spectra to improve the estimation accuracy of foliar nitrogen concentration. *Agric. for. Meteorol.* 248:306–315.
- Woodcock, C.E. and A.H. Strahler. 1987. The factor of scale in remote sensing. *Remote Sens. Environ.* 21:311–332.
- Yang, C., R. Sui, and W.S. Lee. 2016. Precision agriculture in large-scale mechanized farming. In: Q. Zhang, editor, *Precision Agriculture Technology for Crop Farming*. CRC Press, Boca Raton, FL. p. 177–212.
- Youngentob, K.N., D.A. Roberts, A.A. Held, P.E. Dennison, X. Jia, and D.B. Lindenmayer. 2011. Mapping two eucalyptus subgenera using multiple endmember spectral mixture analysis and continuum-removed imaging spectrometry data. *Remote Sens. Environ.* 115:1115–1128.
- Zhang, X., F. Liu, Y. He, and X. Gong. 2013. Detecting macronutrients content and distribution in oilseed rape leaves based on hyperspectral imaging. *Biosyst. Eng.* 115:56–65.
- Zhou, X., W. Huang, J. Zhang, W. Kong, R. Casa, and Y. Huang. 2019. A novel combined spectral index for estimating the ratio of carotenoid to chlorophyll content to monitor crop physiological and phenological status. *Int. J. Appl. Earth Observation Geoinformation* 76:128–142.

CHAPTER 2

Nutrient Disorders of Burley and Flue-Cured Tobacco: Part 1 – Macronutrient Deficiencies

(Published in Crop, Forage & Turfgrass Management)

Henry, J.B., M. Vann, I. McCall, P. Cockson, and B.E. Whipker. 2018a. Nutrient disorders of burley and flue-cured tobacco part 1: Macronutrient deficiencies. Crop, Forage and Turfgrass Mgt. 4:170076. doi:10.2134/cftm2017.11.0076.

Nutrient disorders of burley and flue-cured tobacco part 1: Macronutrient deficiencies

Core Ideas:

- Recognizing macronutrient disorders is important for commercial production.
- Foliar nutrient concentrations were identified for burley and flue-cured tobacco.
- Symptoms and critical values were compared with published results.

Abstract

Nutrient deficiency disorders often manifest unique symptoms and vary in critical nutrient ranges depending on species and type. Understanding and recognizing nutrient disorders for different types of tobacco (*Nicotiana tabacum* L.) is important for maintaining quality and yield. Burley and flue-cured tobacco account for over 90% of all tobacco produced in the United States, and thus, were grown in this study to investigate the effects of macronutrient deficiencies. Tobacco plants were grown in silica sand culture, and control plants received a complete modified Hoagland's all-nitrate solution, whereas nutrient-deficient treatments were induced with a complete nutrient formula withholding a single nutrient. Plants were automatically irrigated, and the leached solution was captured for reuse. A complete replacement of nutrient solutions was done weekly. Plants were monitored daily to document and photograph symptoms as they developed. A description of nutrient disorder symptomology and critical tissue concentrations are presented.

Tobacco production in the United States (U.S.) totaled 326,550 acres in 2015, with burley and flue-cured tobacco accounting for over 90% of total production (USDA NASS, 2016).

Macronutrient deficiencies can become an issue in tobacco transplant production when fertilization is imbalanced, and field production when growing in poor soils or applying an imbalanced fertilizer (Fisher, 2014). Nutrient deficiency symptoms and other secondary issues may also develop due to incorrect fertilizer applications. Root-knot nematodes and black shank fungus are reported to be more prevalent when fertilization practices provide excessive or deficient nutrient levels (Fisher, 2014).

Well documented symptom descriptions and images are vital for proper diagnostics. Nutrient deficiency symptoms were previously induced and reported (McCants and Woltz, 1967; McMurtrey, 1964), but these resources are dated given the advances in photography over the past 50 years. Bryson and Mills (2014) published nutritional sufficiency values for field grown tobacco at several stages of maturity. Sufficiency values are typically very broad and do not specifically indicate the value at which visual symptoms occur. Sufficiency ranges are useful for tobacco growers, but publication of critical foliar nutrient indicate the point at which growers can expect to see visual symptoms. This study was conducted to provide updated descriptions and images of nutritional disorders with associated critical nutrient values.

Experiment Outline

Burley and flue-cured tobacco seeds were sown on 5 May 2016 into four 128-cell plug trays filled with a substrate mix of 80:20 (v:v) Canadian sphagnum peat moss (Conrad Fafard, Agawam, MA) and horticultural coarse perlite (Perlite Vermiculite Packaging Industries, Inc., North Bloomfield, OH) amended with dolomitic lime at 15 lb/yd³ (Rockydale Agricultural,

Roanoke, VA) and a wetting agent (Aquatrols, Cherry Hill, NJ) at 1 lb/yd³. Seedlings were transplanted 1 July into 6-inch diameter (0.5 gal) plastic pots filled with acid washed silica-sand [Millersville #2 (0.03 to 0.05-inch diameter); Southern Products and Silica Co., Hoffman, NC]. There were six pots each containing one single-plant replicate for each treatment and tobacco type, except for the controls, of which there were 30 single plant replicates per tobacco type.

The experiment had a completely randomized design and was conducted in a glass greenhouse in Raleigh, NC (35°N latitude), with 73°F/64°F day/night temperatures. Plants were watered using an automated, recirculating irrigation system made from 4-inch diameter PVC pipe (Charlotte Plastics, Charlotte, NC), fit with 5-inch diameter openings to hold the pots. Control plants were grown with a complete modified Hoagland's all-nitrate solution consisting of 15 mM nitrate-nitrogen (NO₃⁻), 1.0 mM phosphate-phosphorus (H₂PO₄⁻), 6.0 mM potassium (K⁺), 5.0 mM calcium (Ca²⁺), 2.0 mM magnesium (Mg²⁺), and 2.0 mM sulfate-sulfur (SO₄²⁻) (Hoagland and Arnon, 1950); plus 72 μM iron (Fe²⁺), 18 μM manganese (Mn²⁺), 3 μM copper (Cu²⁺), 3 μM zinc (Zn²⁺), 45 μM boron (BO₃³⁻), and 0.1 μM molybdenum (MoO₄²⁻). Macronutrient deficiencies were induced by withholding a single nutrient from this solution. Reagent grade chemicals and deionized (DI) water of 18 mega ohms purity were used to formulate treatment solutions. The plants were drip-irrigated with a sump-pump (model 1A, Little Giant Pump Co., Oklahoma City, OK) system as needed between 6:00 and 18:00 hours. Irrigation solution drained from the pot and was captured for reuse. Nutrient solutions were replaced weekly. The experiment was terminated 76 days after treatments began.

A second set of macronutrient deficient plants was grown for two weeks with the complete fertilizer solution and then thoroughly leached with DI water before being switched to a nutrient deficient solution. This second set had six replicates per treatment. This was done to

allow plants to attain a larger size prior to symptom development, as young nutrient deficient plants were significantly stunted and were not representative of mature plants exhibiting deficiency symptoms.

Data Collection and Analysis

Plants were observed daily to document nutrient disorder symptoms, and were photographed as symptoms progressed. Upon initial symptom development for each treatment, three plants out of six were selected for sampling, as well as three control plants. At each harvest date, plant shoots were separated from the roots and initially rinsed with DI water, then washed in a solution of 0.5 N HCl and again rinsed with DI water. Shoot tissues were dried at 158°F for 72 hours and then ground in a sample mill (Thomas Wiley® Mini-Mill; Thomas Scientific, Swedesboro, NJ), and analyzed for nutrient concentrations by AgSource Laboratories (Lincoln, NE). Total N was processed by Kjeldahl digestion, and determined via flow injection analysis (FIA). Extractable K was processed by 2% acetic acid digestion, and determined via inductively coupled plasma mass spectrometry (ICP-MS). Total P and all other plant minerals were processed by nitric acid/hydrogen peroxide digestion, and determined via ICP-MS. The data was analyzed using PROC ANOVA using SAS (version 9.4; SAS Institute, Cary, NC). Analysis of variance was conducted for each nutrient deficient treatment with its associated control. Where F tests indicated evidence of significant difference among the means, least significant differences (LSDs) ($P \leq 0.05$) were determined to establish mean separation.

Macronutrient Disorders

Nitrogen

Nitrogen (N) deficiency is cited as “the most common deficiency in tobacco” (McMurtrey, 1964). Tobacco grown with N-deficient nutrient solution were the first plants to develop visual symptoms in this study and were sampled eight days after treatments began. Symptoms were similar between burley and flue-cured tobacco. N-deficient plants were initially stunted and had a faint or pale yellow coloration on the lower leaves (Figure 2.1A). The yellow color quickly spread up the plant, and plants remained similar in size to young transplants. Most of the foliage eventually appeared bleached and the lowest leaves became brown. A similar trend of symptom development occurred on plants initially grown with the complete fertilizer solution and later switched to the N-deficient solution (Figure 2.1B). In advanced cases, plants exhibited a distinct gradient from pale yellowing on the lower foliage to green on the upper foliage (Figure 2.1C). Similar symptoms were reported by McMurtrey (1964). This symptomology enables visual distinction from similar symptoms exhibited with a sulfur (S) deficiency.

N-deficient tobacco accumulated significantly less dry weight (Table 2.1), and had foliar N concentrations four-fold and five-fold lower than control plants for flue-cured and burley tobacco, respectively (Table 2.2). The foliar N concentrations of control plants grown in this study were within the sufficiency ranges reported by Bryson and Mills (2014) of 3.5–6.5% N. The concentrations in N-deficient plants were below the sufficiency range (Table 2.2).

Phosphorus

Phosphorus (P) deficient tobacco plants were sampled eight days after treatments began. The plants were stunted and initially developed olive green or brown leaf spots (Figure 2.2A).

Symptoms were similar between burley and flue-cured tobacco. Over time, the olive green spots faded and the leaves became covered in non-uniform brown spots. Similar spotting was reported by McMurtrey (1964), but was stated to be inconsistent. Brown spotting was ubiquitous on all P-deficient plants grown in our study. The lower leaves then developed a bright amber coloration (Figure 2.2B). The brown spots grew larger and often coalesced together to form large necrotic patches. The lower leaves eventually became entirely brown and drooped downward along the margins, taking on a wilted appearance (Figure 2.2C). These symptoms progressed up the plant; however, the upper leaves remained asymptomatic. P deficiency on tobacco resulted in distinct characteristics that should avoid confusing this deficiency with other nutritional disorders (Figure 2.2D). P deficiency prevents field grown tobacco leaves from attaining mature size, as leaves remain narrow in appearance (McMurtrey, 1964).

Control plants accumulated greater dry weight (Table 2.1) and had foliar P concentrations six-fold to seven-fold greater than P-deficient plants (Table 2.2). Published P sufficiency values suggest that foliar P concentrations should be within 0.1–1.0% (Bryson and Mills, 2014). The control plants grown in this study were within this range, while the P-deficient plants had lower foliar P concentrations (Table 2.2).

Potassium

Potassium (K) deficiency symptoms also developed within eight days. Symptoms were similar between burley and flue-cured tobacco. Young tobacco grown under the K-deficient treatment became pale yellow along the lower leaf margins that quickly progressed up the plant (Figure 2.3A). The yellow coloration spread inward from the margin, leaving green tissue only around the midvein and primary leaf veins (Figure 2.3B). Additionally, the affected leaf margins

would curl downward, giving the leaf an umbrella-like appearance. Yellow tissue later became completely brown, and would collapse, giving affected leaves a ragged appearance. These observed symptoms were similar to those described by McMurtrey (1964). Mature plants exhibiting K deficiency developed a bright yellow coloration on the lower and central foliage (Figure 2.3C). Although the symptoms were prominent along the entire margin, early symptoms demonstrate that the yellowing was more severe at the leaf tip (Figure 2.3D).

K-deficient plants accumulated less dry weight (Table 2.1) and had foliar K concentrations seven-fold to ten-fold less than control plants (Table 2.2). The K sufficiency ranges published by Bryson and Mills (2014) suggest optimal foliar K concentrations from 1.6–4.1%. K-deficient plants grown in our study had foliar K concentrations lower than the sufficiency range, while control plants had K concentrations higher than the sufficiency range (Table 2.2). This alludes to the fact that tobacco is considered luxury consumers of K when the K supply is not limited (McMurtrey, 1964), and tobacco plants absorb higher concentrations of K than other mineral nutrients (McCants, 1967).

Calcium

Symptoms of calcium (Ca) deficiency developed 21 days after treatments began. The initial symptom of Ca deficiency was distortion of the upper leaves and apical meristem (Figure 2.4A). These symptoms appeared similar to those exhibited during boron (B) deficiency (Figure 2.4B). As symptoms progressed, two distinct patterns of distortion developed that could be used to distinguish Ca and B deficiencies. Both patterns developed on both types of tobacco; however, each type of tobacco appeared to favor one of the two patterns. One distortion was a cut leaf pattern, in which long tears developed along the leaf margins, perpendicular to the midvein

(Figure 2.4C). The other distortion was similar in appearance to a shepherd's crook, where the leaf tip curved in such a way that the abaxial leaf surface was parallel to itself (Figure 2.4D). The cut leaf pattern was more commonly observed on flue-cured tobacco, while the shepherd's crook pattern was more common on burley tobacco. In some plants, the apical meristem became necrotic, causing a mass of axillary shoots to develop from the stem (Figure 2.4E). These axillary shoots rapidly became necrotic, ceasing further expansion or development. McMurtrey (1964) also reported a proliferation of axillary shoots that was followed quickly by bud death.

Ca-deficient burley tobacco plants accumulated less dry mass, while flue-cured plants were similar in weight to control plants (Table 2.1). As symptoms progressed, all Ca-deficient plants were shorter and more compact than control plants. Ca-deficient plants had foliar Ca concentrations eightfold to tenfold less than control plants (Table 2.2). Foliar Ca concentrations should be 1.5–3.5% (Bryson and Mills, 2014), which was much higher than the concentrations observed in Ca-deficient plants grown in our study (Table 2.2).

Magnesium

Tobacco plants deficient in magnesium (Mg) were initially asymptomatic but developed symptoms after 33 days of treatment. Symptoms were similar between burley and flue-cured tobacco. Interveinal chlorosis of the lower and central foliage rapidly spread to all but the most immature leaves (Figure 2.5A). The chlorosis became a pale yellow over time, nearly turning white. Only the midrib and primary veins retained any green coloration. When leaves turned white, the leaf margins appeared wilted (Figure 2.5B). Mg-deficient burley tobacco accumulated less dry weight than control plants, while flue-cured tobacco plants were similar in dry weight (Table 2.1). Control plants from both types of tobacco had foliar Mg concentrations ten-fold to

eleven-fold greater than Mg-deficient plants (Table 2.2). Published sufficiency values suggest foliar Mg concentrations of 0.20–0.85% (Bryson and Mills, 2014). Mg concentrations in Mg-deficient plants were four-fold to five-fold lower than the low end of this sufficiency range (Table 2.2).

Sulfur

S deficiency resulted in an initial chlorosis that was uniform over the entire plant (Figure 2.6A). Symptoms developed within eight days and were similar between burley and flue-cured tobacco. The yellowing was similar in coloration to N-deficient plants, but the overall yellow appearance could be used to distinguish between these two deficiencies. Mature plants exhibiting S deficiency symptoms were pale yellow uniformly over the entire plant (Figure 2.6B). The pale yellow on the upper foliage was easily distinguished from the green coloration on the upper foliage of control plants (Figure 2.6C). When plants were sampled at early symptom development, S-deficient burley and flue-cured tobacco plants had greater dry weight than control plants (Table 2.1). As symptoms progressed, control plants quickly grew larger than S-deficient plants. Foliar S concentrations were significantly less than control plants in S-deficient burley and flue-cured plants (Table 2.2). Foliar S concentrations should be within the range of 0.18–0.50% in tobacco (Bryson and Mills, 2014). Flue-cured tobacco plants grown in our study exhibited deficiency symptoms with 0.21% S, suggesting the published sufficiency range may be too low (Table 2.2).

Conclusions

The macronutrient deficiencies induced in this study provide tobacco growers with updated descriptions and high quality diagnostic images. Additionally, the reported foliar nutrient values will aid growers in making fertilization decisions. All macronutrient deficiencies except S deficiency significantly limited dry weight in burley plants, while only N, P, and K-deficient flue-cured plants accumulated less dry weight than the controls. Macronutrient deficient plants were all stunted later in the study when compared to asymptomatic controls. Symptoms developed rapidly for most macronutrient deficiencies, demonstrating the importance of symptom recognition and implementing fertility monitoring practices.

Acknowledgements

We would like to thank the North Carolina Tobacco Foundation for funding this research.

References

- Bryson, G. and H. Mills. 2014. Plant analysis handbook IV. Micro-Macro Publishing. Athens, GA.
- Fisher, L.R., editor. 2014. 2014 North Carolina State University flue-cured tobacco production guide (AG-187 (revised)). North Carolina Coop. Ext. Serv., Raleigh.
- Hoagland, R.J. and D.I. Arnon. 1950. The water-culture method for growing plants without soil. California Agr. Expt. Sta. Circ. 347. Revised ed.
- McCants, C. and W. Woltz. 1967. Growth and mineral nutrition of tobacco. *Adv. Agron.* 19:211–265.
- McMurtrey, J.E. 1964. Chapter IV: Nutrient deficiencies in tobacco. p. 99–141. *In*: H.B. Sprague. *Hunger signs in crops*. 3rd ed. David McKay Company, Inc., New York, NY.
- USDA NASS. 2016. Crop production 2015 summary. United States Department of Agriculture. <https://www.usda.gov/nass/PUBS/TODAYRPT/cropan16.pdf> (Accessed 12 Oct. 2017).

Table 2.1. Mean dry weights of burley and flue-cured tobacco grown with a deficient macronutrient treatment compared to plants grown with a complete fertilizer.

Treatment	Dry weight (oz)					
	-N [†]	-P	-K	-Ca	-Mg	-S
<i>Burley</i>						
Control	0.05	0.05	0.05	0.51	2.41	0.05
Disorder	0.02	0.03	0.04	0.24	1.60	0.07
	*** [‡]	**	*	***	**	**
<i>Flue-cured</i>						
Control	0.05	0.05	0.05	0.46	2.39	0.05
Disorder	0.02	0.04	0.04	0.34	2.27	0.08
	***	**	*	NS	NS	*

[†] Nitrogen (N), phosphorus (P), potassium (K), calcium (Ca), magnesium (Mg), and sulfur (S)

[‡] *, **, or *** indicate statistically significant differences between sample means based on least significant differences where *F* tests were $P < 0.05$, $P < 0.01$, or $P < 0.001$, respectively. NS (not significant) indicates the *F* test difference between sample means was $P > 0.05$.

Table 2.2. Foliar nutrient concentrations of burley and flue-cured tobacco grown with a deficient macronutrient treatment compared to plants grown with a complete fertilizer.

Treatment	-N [†]	-P	-K	-Ca	-Mg	-S
Tissue nutrient concentration (%)						
Element	N	P	K	Ca	Mg	S
<i>Burley</i>						
Complete	4.80	0.41	5.65	1.91	0.59	0.38
Disorder	0.94	0.07	0.76	0.24	0.05	0.13
	***‡	***	***	***	***	***
<i>Flue-cured</i>						
Complete	4.76	0.47	7.71	2.42	0.41	0.45
Disorder	1.16	0.07	0.76	0.25	0.04	0.21
	***	***	***	***	***	***

[†] Nitrogen (N), phosphorus (P), potassium (K), calcium (Ca), magnesium (Mg), and sulfur (S)

[‡] *, **, or *** indicate statistically significant differences between sample means based on least significant differences where *F* tests were $P < 0.05$, $P < 0.01$, or $P < 0.001$, respectively. NS (not significant) indicates the *F* test difference between sample means was $P > 0.05$.

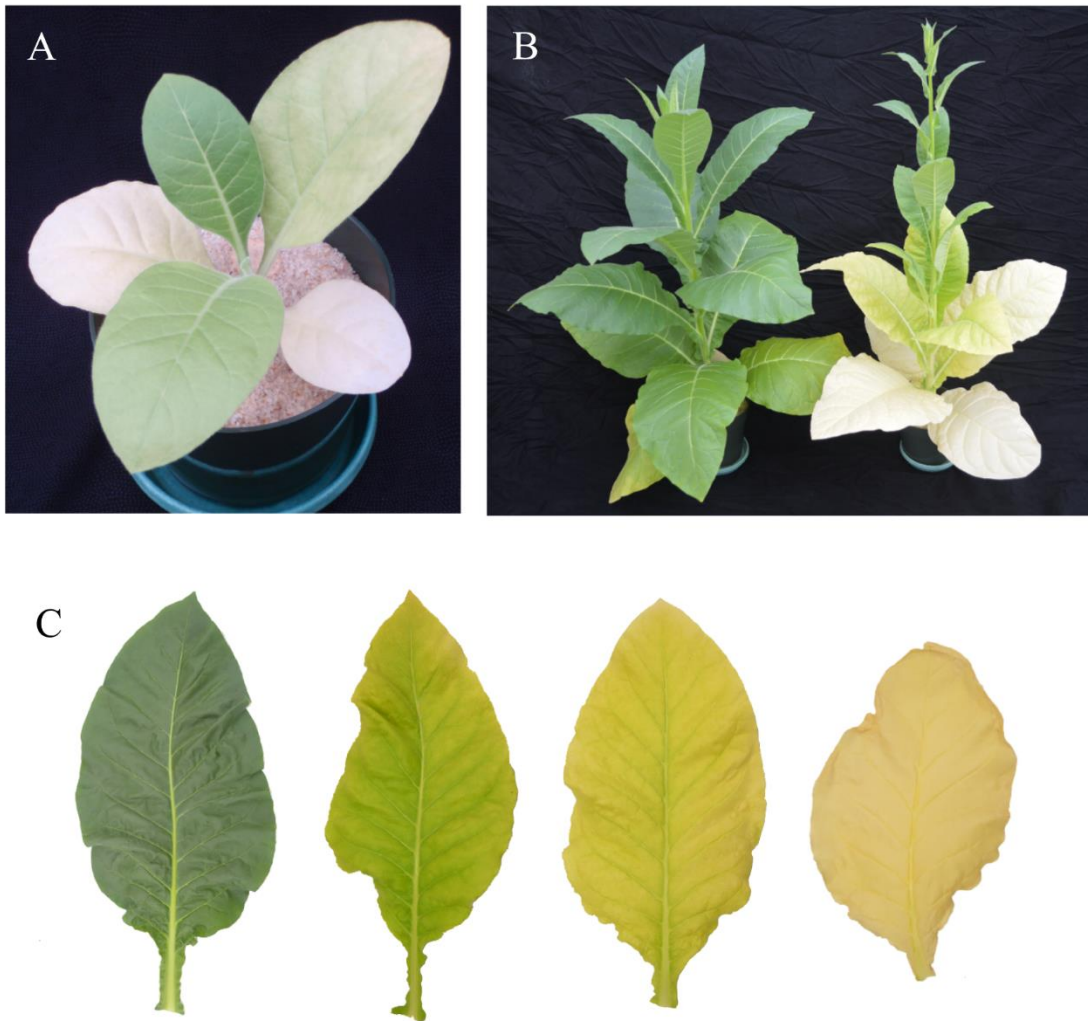


Figure 2.1. Nitrogen-deficient tobacco plants exhibiting a pale yellow coloration (A) at an early stage of growth, (B) at a mature stage of growth compared with an asymptomatic control, and (C) a foliar symptom progression from asymptomatic (left) to highly symptomatic (right).

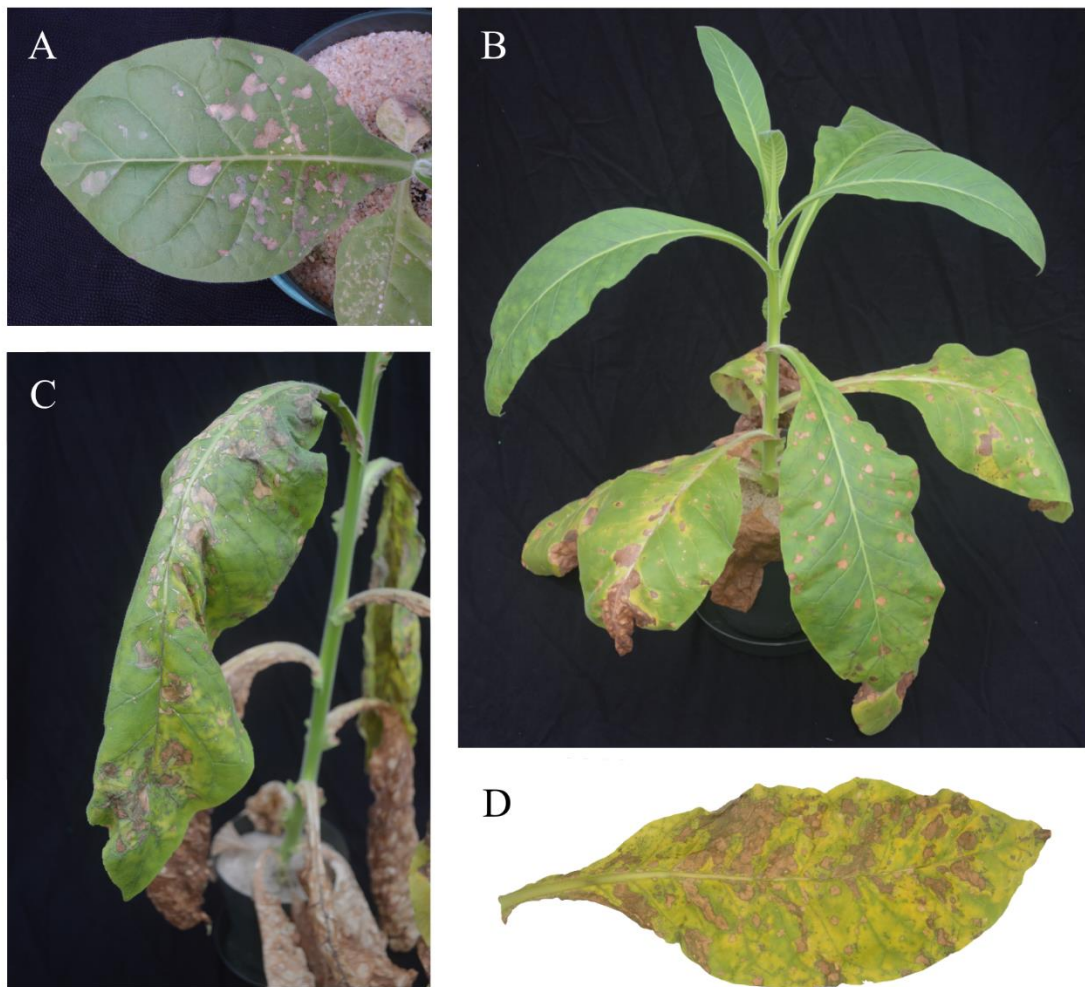


Figure 2.2. Symptoms of phosphorus deficiency (A) on a young plant leaf, (B) on the lower foliage of a more mature plant, (C) and advanced symptoms on a mature plant. Symptoms of (D) brown and olive green spotting, in addition to an overall yellowing were present on the lower foliage.

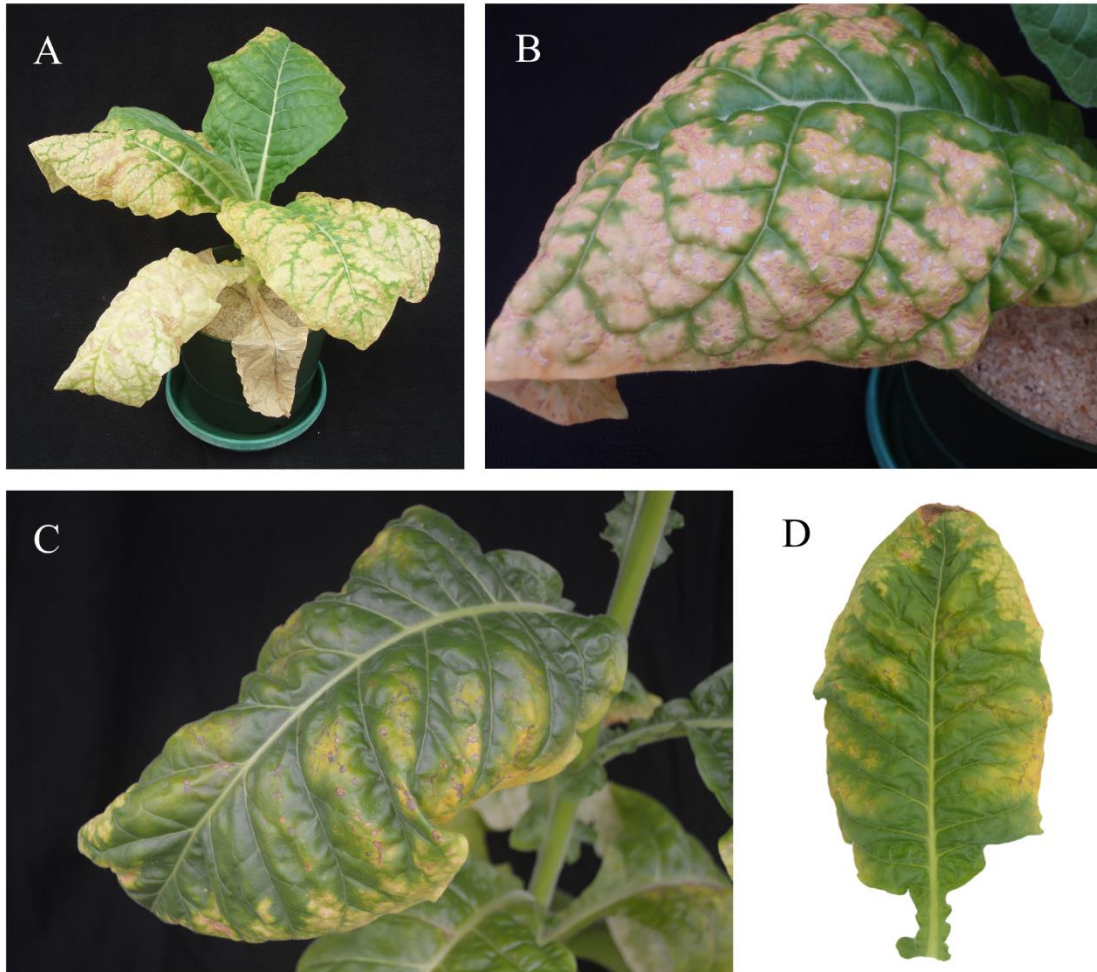


Figure 2.3. Potassium (K) deficiency symptoms (A) on the lower leaves of a young tobacco plant with (B) a pale yellowing and interveinal browning. On mature plants (C) K deficiency had a deeper yellow coloration, which (D) was most prominent at the leaf tip.

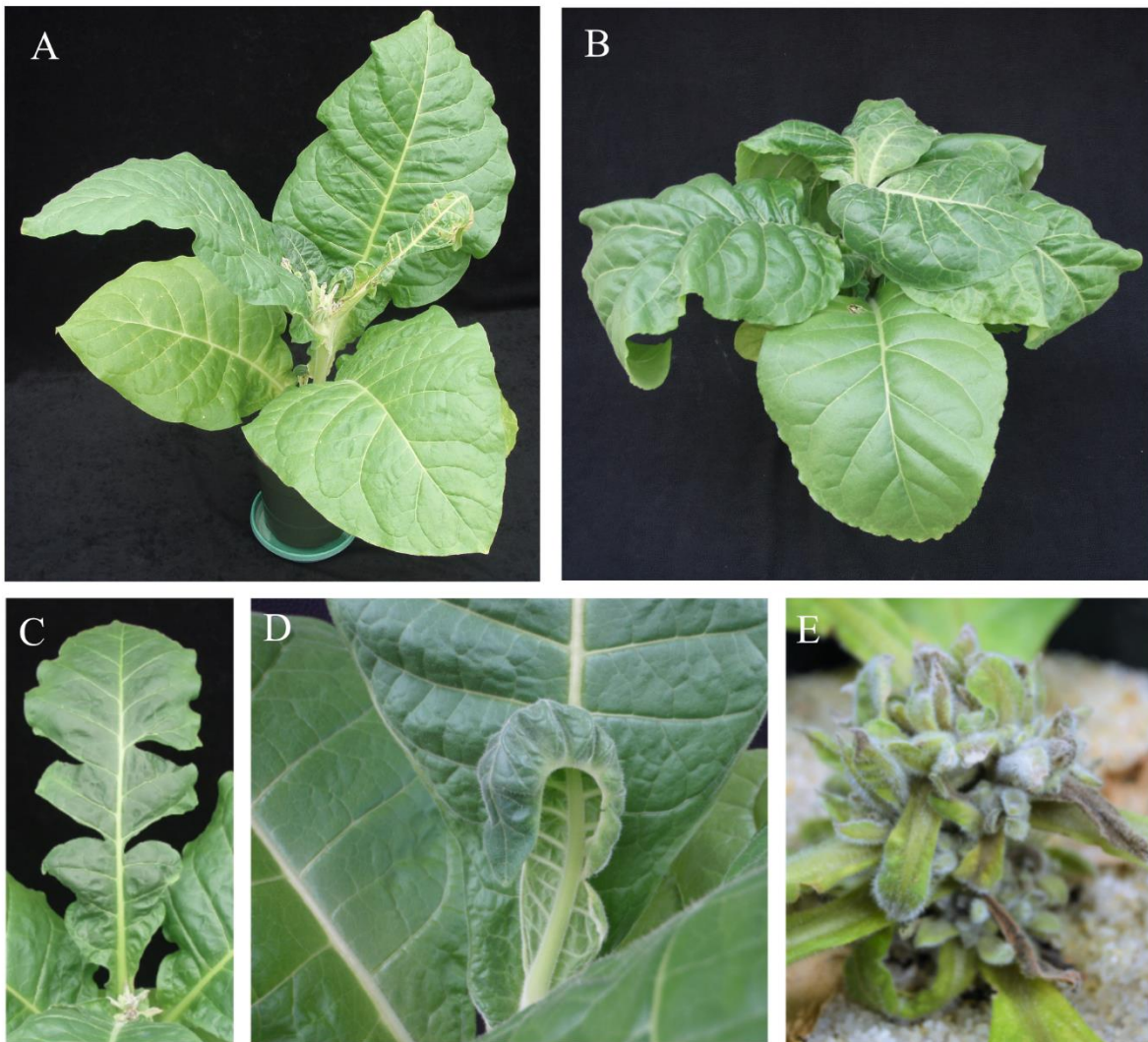


Figure 2.4. Symptoms of (A) distortion of the upper leaves developed initially in response to calcium deficiency. These symptoms were similar to those of (B) boron-deficient tobacco. Flue-cured tobacco primarily exhibited (C) a cut leaf pattern, while burley tobacco primarily exhibited (D) a distorted 'shepherd's crook' appearance. In some instances, (E) the apical meristem would die, leading to a proliferation of axillary shoots which quickly became necrotic.



Figure 2.5. Magnesium deficiency symptoms of (A) a bright interveinal yellowing of the central and lower leaves that was easily distinguished from asymptomatic control plants. As symptoms progressed, (B) the lower leaves appeared nearly white and wilted.

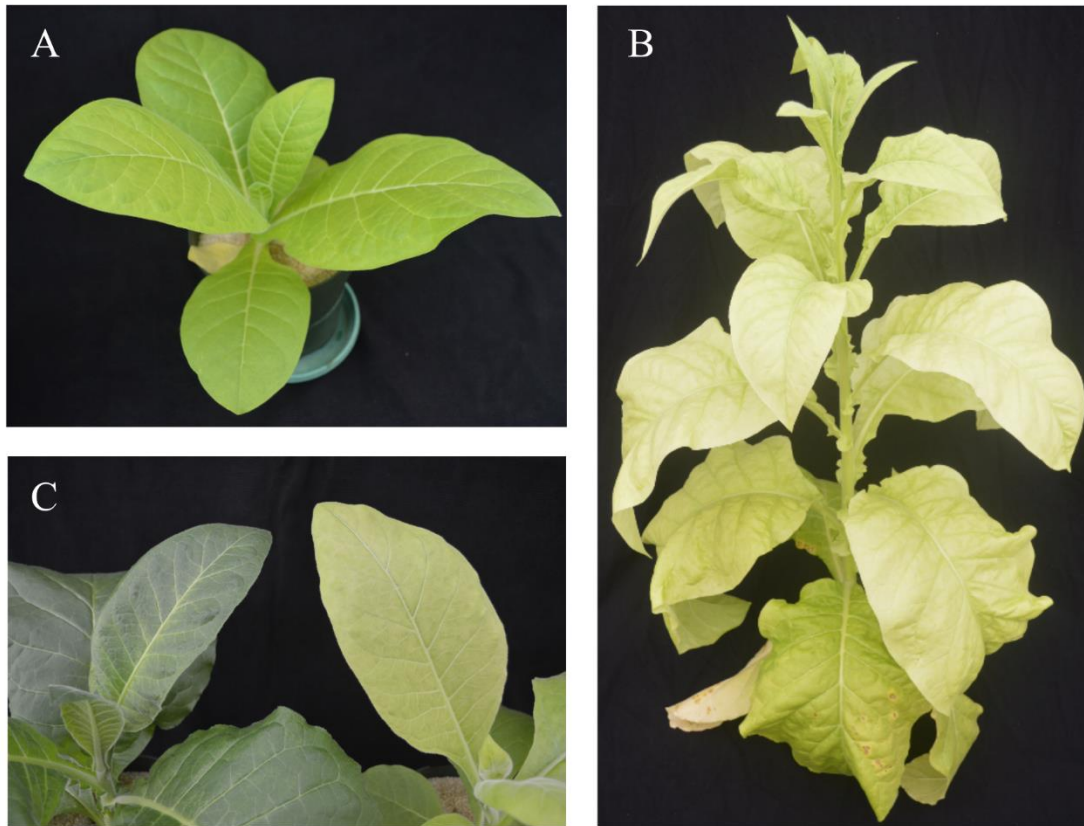


Figure 2.6. Tobacco rapidly developed symptoms of sulfur deficiency. Young plants (A) had a prominent yellow coloration, while (B) mature plants exhibited a uniform pale yellow coloration that (C) was distinctly paler than the asymptomatic controls.

CHAPTER 3

Nutrient Disorders of Burley and Flue-Cured Tobacco: Part 2 – Micronutrient Disorders

(Published in Crop, Forage & Turfgrass Management)

Henry, J.B., M. Vann, I. McCall, P. Cockson, and B.E. Whipker. 2018b. Nutrient disorders of burley and flue-cured tobacco part 2: Micronutrient disorders. Crop, Forage and Turfgrass Mgt. 4:170077. doi:10.2134/cftm2017.11.0077.

Nutrient disorders of burley and flue-cured tobacco part 2: Micronutrient disorders

Josh B. Henry^{1,2,*}, Matthew Vann¹, Ingram McCall², Paul Cockson², and Brian E. Whipker²

¹Dep. of Crop and Soil Sciences, North Carolina State Univ., Raleigh, NC 27695

²Dep. of Horticultural Science, North Carolina State Univ., Raleigh, NC 27695

*Corresponding author (josh.brady.henry@gmail.com)

Core Ideas:

- Recognizing micronutrient disorders is important for commercial production.
- Unique, previously unobserved nutrient disorder symptoms were observed.
- Foliar nutrient concentrations were identified for burley and flue-cured tobacco.
- Symptoms and critical values were compared with published results.

Abstract

Nutrient disorders often manifest unique symptoms and vary in critical nutrient ranges where visual symptoms appear depending on plant species and type. Understanding and recognizing nutrient disorders for different types of tobacco is important for maintaining yield and quality. Burley and flue-cured tobacco (*Nicotiana tabacum* L.) account for over 90% of all tobacco produced in the United States, and thus, were grown in this study to investigate the effects of micronutrient disorders. Tobacco plants were grown in silica sand culture, and control plants received a complete modified Hoagland's all-nitrate solution, whereas nutrient-deficient treatments were induced with a complete nutrient formula withholding a single nutrient. Boron toxicity was also induced by increasing the element tenfold higher than the complete nutrient formula. Plants were automatically irrigated, and the leached solution was captured for reuse. A complete replacement of nutrient solutions was done weekly. Plants were monitored daily to document and photograph symptoms as they developed. A description of nutrient disorder symptomology and critical tissue concentrations associated with symptomology are presented.

Tobacco production in the United States (U.S.) totaled 326,550 acres in 2015, with burley and flue-cured tobacco accounting for over 90% of total production (USDA NASS, 2016). Recognizing the symptoms of nutritional disorders in these two types of tobacco is important for tobacco growers to maintain crop yield and quality. Micronutrient disorders are not typically considered a major issue in commercial tobacco production; however, documenting symptoms is vital for proper diagnostics. Nutritional issues may develop due to incorrect fertilizer applications. For instance, boron toxicity was induced in tobacco with an application rate of just 0.9 lbs per acre (Vann, 2014). Symptoms of several micronutrient disorders were previously induced and reported (McCants and Woltz, 1967; McMurtrey, 1964; Steinberg, 1953), but many of these studies were conducted over 50 years ago. Bryson and Mills (2014) published nutritional sufficiency values for field grown tobacco at several stages of maturity. Sufficiency values are typically very broad and do not specifically indicate the value at which visual symptoms occur. Sufficiency ranges are useful for tobacco growers, but critical foliar nutrient values indicate the point at which growers can expect to see visual symptoms. This study was conducted to provide updated descriptions and images of nutritional disorders with associated critical nutrient values.

Experiment Outline

Burley and flue-cured tobacco seeds were sown on 5 May 2016 into four 128-cell plug trays filled with a substrate mix of 80:20 (v:v) Canadian sphagnum peat moss (Conrad Fafard, Agawam, MA) and horticultural coarse perlite (Perlite Vermiculite Packaging Industries, Inc., North Bloomfield, OH) amended with dolomitic lime at 15 lb/yd³ (Rockydale Agricultural, Roanoke, VA) and a wetting agent (Aquatrols, Cherry Hill, NJ) at 1 lb/yd³. Seedlings were transplanted 1 July into 6-inch diameter (0.5 gal) plastic pots filled with acid washed silica-sand

[Millersville #2 (0.03 to 0.05 inch diameter); Southern Products and Silica Co., Hoffman, NC].

There were six pots each containing one single-plant replicate for each treatment and tobacco type, except for the controls, of which there were 30 single plant replicates per tobacco type.

The experiment had a completely randomized design and was conducted in a glass greenhouse in Raleigh, NC (35°N latitude), with 73°F/64°F day/night temperatures. Plants were grown in an automated, recirculating irrigation system made from 4-inch diameter PVC pipe (Charlotte Plastics, Charlotte, NC), fit with 5-inch diameter openings to hold the pots. Control plants were grown with a complete modified Hoagland's all-nitrate solution consisting of 15 mM nitrate-nitrogen (NO_3^-), 1.0 mM phosphate-phosphorus (H_2PO_4^-), 6.0 mM potassium (K^+), 5.0 mM calcium (Ca^{2+}), 2.0 mM magnesium (Mg^{2+}), and 2.0 mM sulfate-sulfur (SO_4^{2-}) (Hoagland and Arnon, 1950); plus 72 μM iron (Fe^{2+}), 18 μM manganese (Mn^{2+}), 3 μM copper (Cu^{2+}), 3 μM zinc (Zn^{2+}), 45 μM boron (BO_3^{3-}), and 0.1 μM molybdenum (MoO_4^{2-}). Micronutrient deficiencies were induced by withholding a single nutrient from this solution. Boron toxicity was induced by increasing the concentration tenfold higher than the complete nutrient formula. Reagent grade chemicals and deionized (DI) water of 18 mega ohms purity were used to formulate treatment solutions. The plants were drip-irrigated with a sump-pump (model 1A, Little Giant Pump Co., Oklahoma City, OK) system as needed between 6:00 and 18:00 hours. Irrigation solution drained from the pot and was captured for reuse. Nutrient solutions were replaced weekly. The experiment was terminated 76 days after treatments began.

Data Collection and Analysis

Plants were observed daily to document nutrient disorder symptoms, and were photographed as symptoms progressed. Upon initial symptom development for each treatment,

three plants out of six were selected for sampling, as well as three control plants. At each sampling date, whole plant shoots were separated from the roots and initially rinsed with DI water, then washed in a solution of 0.5 N HCl, and again rinsed with DI water. Shoot tissues were dried at 158°F for 72 hours, ground in a mill (Thomas Wiley® Mini-Mill; Thomas Scientific, Swedesboro, NJ), and analyzed for nutrient concentrations by AgSource Laboratories (Lincoln, NE). All micronutrients were processed by nitric acid/hydrogen peroxide digestion, and determined via ICP-MS. The data were analyzed using PROC ANOVA in SAS (version 9.4; SAS Institute, Cary, NC). Analysis of variance was conducted for each nutrient deficient treatment with its associated control. Where F tests indicated evidence of significant difference among the means, least significant differences (LSDs) ($P \leq 0.05$) were determined to establish mean separation.

Micronutrient Disorders

Boron

Plants grown under the B-deficient treatment developed symptoms 8 days after initiating the B-deficiency treatment. Plants were initially stunted and developed thickened dark green leaves (Figure 3.1A). The apical meristem became distorted and necrotic, inhibiting further vertical growth and inducing axillary shoot development (Figure 3.1B). As symptoms progressed, the leaves began to curl downward and developed perpendicular cracks across the midvein (Figure 3.1C). These symptoms were similar to those reported by McMurtrey (1964). Internodes did not elongate, giving the plant a compact, dwarf appearance. A bright amber chlorosis later developed in the primary veins branching off the midvein (Figure 3.1C). The axillary shoots eventually became necrotic as well. B deficiency symptoms were similar to those

of Ca deficiency; however, Ca-deficient plants developed a unique hooked appearance and greater proliferation of axillary stems.

At initial symptom development, B deficient plants were similar or greater in weight compared to control plants (Table 3.1). Deficient plants experienced a rapid cessation of growth and were severely stunted compared to the controls (Figure 3.1D). Foliar B concentrations in B-deficient plants were 6.06 and 15.09 ppm for burley and flue-cured tobacco, respectively (Table 3.2). Control plants contained 27.87–35.60 ppm B, which was within published sufficiency values ranging from 14–50 ppm B (Bryson and Mills, 2014). Previous studies reported B deficiency symptoms on tobacco with 5.5 ppm B in the foliage, and suggest ~15 ppm B as the critical level required to avoid symptoms in flue-cured tobacco (McCants and Woltz, 1967).

Boron toxicity symptoms developed 33 days after treatments began. Boron toxicity initially led to dull chlorotic spots along the margins of the lower foliage (Figure 3.2A). Several of these spots were sunken into the leaf surface, giving the margin an undulating and uneven appearance. The chlorosis slowly spread until entire leaf margins became pale and chlorotic (Figure 3.2B). Symptoms then progressed inward to the midvein, and only the largest veins remained green. Burley and flue-cured plants remained similar in dry weight to control plants (Table 3.1), but accumulated B concentrations that were 5 and 10X greater, respectively (Table 3.2). Flue-cured tobacco accumulated foliar B at concentrations nearly 10X greater than those published by Bryson and Mills (2014).

Copper

Cu deficiency manifested in 65 days with symptoms different from those previously described by McMurtrey (1964). Initial symptoms were small, chlorotic and necrotic spots on the

central and lower foliage (Figure 3.3A). These areas enlarged over time and took on a vibrant amber coloration. Veins within the chlorotic regions became necrotic with a dark black coloration (Figure 3.3B). In addition to foliar symptoms, large black lesions formed on the stems. These necrotic lesions were often located at the base of a leaf petiole and surrounded some or all of the node (Figure 3.3C). Lesions were also located along the internodes but were more commonly found at the base of the petioles. The black lesions near the base of the petioles eventually spread up the petiole onto the leaf surface (Figure 3.3D). These symptoms differed from previously published symptoms, which described bending of the upper stem and wilting in response to Cu deficiency (McMurtrey, 1964). Stem bending was not observed on Cu-deficient plants grown in our study, and plants appeared upright and turgid while symptomatic.

Cu-deficient burley tobacco plants had similar dry weight to controls, while flue-cured tobacco plants had lower dry weights than the controls (Table 3.1). Cu-deficient burley and flue-cured tobacco plants had lower foliar Cu concentrations than their associated controls. Burley tobacco averaged 8.79 and 0.59 ppm Cu in control and Cu-deficient plants, respectively, while flue-cured tobacco had 7.61 and 1.31 ppm Cu (Table 3.2). Published sufficiency values for foliar Cu concentrations in tobacco range from 10–60 ppm (Bryson and Mills, 2014). The Cu-deficient plants grown in this study were sampled at the bloom stage, which had a narrower sufficiency range of 15–60 ppm Cu (Bryson and Mills, 2014). The control plants grown in this study accumulated Cu at concentrations on the lower end of these sufficiency ranges, while Cu-deficient plants had far lower foliar Cu concentrations (Table 3.2).

Iron

Symptoms of an upper leaf interveinal chlorosis developed on Fe-deficient plants in 65 days. The leaves were brighter in appearance compared to control plants, and symptoms spread throughout the upper half of the foliage (Figure 3.4). These symptoms were similar to those reported in a previous study (McMurtrey, 1964). Fe-deficient burley and flue-cured tobacco plants had weights similar to the controls (Table 3.1). Both types of tobacco had significantly lower foliar Fe concentrations than control plants with 33.50 and 37.21 ppm Fe for burley and flue-cured tobacco, respectively (Table 3.2). Published sufficiency values suggest younger tobacco contains higher Fe concentrations ranging from 430–1000 ppm, while plants near the blooming stage have 50–200 ppm Fe (Bryson and Mills, 2014). These values reported for mature tobacco plants were similar to those in the control plants from our study (Table 3.2).

Manganese

Symptoms of Mn deficiency developed in 35 days and differed between burley and flue-cured tobacco plants. Initially, both types of tobacco developed a bright yellow netted interveinal chlorosis on the upper and central foliage (Figure 3.5A). This pattern of chlorosis initiated near the leaf margin and spread toward the midvein. These symptoms were quite distinct when compared with asymptomatic control plants (Figure 3.5B). In burley tobacco, symptoms became pale and uniform over the entire plant. Small, thin necrotic spots (<0.5 inch) developed over most of the leaf surface. Flue-cured tobacco plants were somewhat chlorotic, but remained greener than burley plants (Figure 3.5C). Similar necrotic spotting developed on the middle and lower foliage; however, these spots became much larger than those observed on burley plants (Figure 3.5D). The necrotic spots on flue-cured tobacco plants eventually merged to form large

areas of irregularly shaped necrosis. The necrotic areas eventually cracked, collapsed, and fell out, creating large holes throughout the leaf. The leaves became fragile and quickly developed a ragged appearance. These symptoms were similar to those reported by McMurtrey (1964) and McCants and Woltz (1967).

Mn-deficient burley tobacco accumulated less dry weight than control plants, while flue-cured plants had similar weights as control plants when symptoms initially appeared (Table 3.1). Foliar Mn concentrations were similar between burley and flue-cured tobacco with 33.72–35.84 ppm Mn in control plants (Table 3.2). Mn-deficient plants had significantly lower Mn concentrations, with 12.10–13.48 ppm Mn (Table 3.2). Previous work reported Mn-deficiency symptoms on plants with slightly higher concentrations of 22 ppm Mn (McCants and Woltz, 1967). Foliar Mn concentrations in control plants were within the published sufficiency range of 26–400 ppm Mn (Bryson and Mills, 2014).

Molybdenum

Plants were grown through maturation, and no visual symptoms developed on any Mo deficient tobacco plants. Burley tobacco plants were similar in size, but Mo deficient flue-cured tobacco plants had greater dry weight than control plants (Table 3.1). Foliar Mo levels were similar among control and Mo deficient tobacco plants (Table 3.2). Burley tobacco plants had Mo concentrations averaging 0.01 ppm, while Mo concentrations averaged 10.54–13.11 ppm in flue-cured plants (Table 3.2). Published Mo sufficiency concentrations range from 0.1–1 ppm in field grown tobacco (Bryson and Mills, 2014). Previously reported Mo deficiency symptoms include chlorosis of the lower leaves, twisted and bent foliage, necrotic spotting, and delayed blooming (McCants and Woltz, 1967; McMurtrey, 1964; Steinberg, 1953). Mo and other

micronutrient deficiencies are sometimes difficult to induce and often will not manifest visual symptoms (Barnes, 2010).

Zinc

Zn-deficient plants were similar in size to control plants for both tobacco types (Table 3.1). Neither type developed any visual symptoms, although the Zn concentration in burley tobacco was significantly lower than that of the control (Table 3.2). Previous work reported the development marginal and tip chlorosis on the lower foliage in response to Zn deficiency, followed by water-soaked spotting (McMurtrey, 1964). The water-soaked spots were described as being similar to a common bacterial disease of tobacco, eventually developing necrotic spots with chlorotic halos (McMurtrey, 1964). Published concentrations in flue-cured tobacco ranged from 22–74 ppm Zn in one study (Ward, 1941) and 17–110 ppm Zn for the recently reported sufficiency range (Bryson and Mills, 2014). The foliar Zn concentrations were lower in our study, with 6.57–12.64 ppm Zn in control plants and 1.95–5.73 ppm Zn in deficient plants (Table 3.2).

Conclusions

The micronutrient disorders described in this study provide tobacco growers with updated descriptions and high-quality diagnostic images to better identify nutrient disorders. Previous work described symptoms, but often did not report critical foliar nutrient values. These nutrient values can also help growers to monitor their crop, and can be used to make improved fertilization decisions. Previously undescribed symptoms of Cu deficiency were described in addition to updated descriptions of many other micronutrient disorders. Most disorders had no

initial effect on overall plant dry weight; however, many of the plants with advanced disorder symptomology were ultimately stunted compared to control plants. This illustrates the importance of recognizing these disorders at an early stage to implement corrective procedures in order to optimize yield and produce a successful crop.

Acknowledgements

We would like to thank the North Carolina Tobacco Foundation for funding this research.

References

- Barnes, J.G. 2010. Characterization of nutrient disorders of floriculture species. MS Thesis, North Carolina State Univ., Raleigh, NC.
- Bryson, G. and H. Mills. 2014. Plant analysis handbook IV. Micro-Macro Publishing. Athens, GA.
- Hoagland, R.J. and D.I. Arnon. 1950. The water-culture method for growing plants without soil. California Agr. Expt. Sta. Circ. 347. Revised ed.
- McCants, C. and W. Woltz. 1967. Growth and mineral nutrition of tobacco. *Adv. Agron.* 19:211–265.
- McMurtrey, J.E. 1964. Chapter IV: Nutrient deficiencies in tobacco. p. 99–141. *In*: H.B. Sprague. *Hunger signs in crops*. 3rd ed. David McKay Company, Inc., New York, NY.
- Steinberg, R.A. 1953. Symptoms of molybdenum deficiency in tobacco. *Plant Physiol.* 28(2):319–322.
- USDA NASS. 2016. Crop production 2015 summary. United States Department of Agriculture. <https://www.usda.gov/nass/PUBS/TODAYRPT/cropan16.pdf> (Accessed 12 Oct. 2017).
- Vann, M. 2014. Addressing boron issues in North Carolina flue-cured tobacco. North Carolina State University Extension, Raleigh, NC. <https://tobacco.ces.ncsu.edu/2014/04/addressing-boron-issues-in-north-carolina-flue-cured-tobacco/> (Accessed 12 Oct. 2017).
- Ward, G. 1941. Mineral-absorption studies with tobacco. *The Lighter* 11(1):16–22.

Table 3.1. Mean dry weights of burley and flue-cured tobacco grown with a deficient or toxic micronutrient treatment compared to plants grown with a complete fertilizer.

Treatment	Dry weight (oz)						
	-B [†]	+B	-Cu	-Fe	-Mn	-Mo	-Zn
<i>Burley</i>							
Control	0.05	0.87	1.71	1.71	0.43	2.38	2.38
Disorder	0.05	0.80	1.82	2.20	0.20	3.06	2.19
	NS [‡]	NS	NS	NS	**	NS	NS
<i>Flue-cured</i>							
Control	0.05	2.39	1.85	2.39	0.61	2.72	2.72
Disorder	0.09	2.63	1.59	1.66	0.35	3.98	2.35
	**	NS	**	NS	NS	***	NS

[†] Boron (B), copper (Cu), iron (Fe), manganese (Mn), molybdenum (Mo), and zinc (Zn).

[‡] *, **, or *** indicate statistically significant differences between sample means based on *F* tests at $P < 0.05$, $P < 0.01$, or $P < 0.001$, respectively. NS (not significant) indicates the *F* test difference between sample means was $P > 0.05$.

Table 3.2. Foliar nutrient concentrations of burley and flue-cured tobacco grown with a deficient or toxic micronutrient treatment compared to plants grown with a complete fertilizer.

Treatment	Tissue nutrient concentration (ppm)						
	-B [†]	+B	-Cu	-Fe	-Mn	-Mo	-Zn
<i>Burley</i>							
Control	27.87	48.39	8.79	62.91	33.72	0.01	6.57
Disorder	6.06	235.07	0.59	33.50	12.10	0.01	1.95
	*** [‡]	***	***	***	***	NS	*
<i>Flue-cured</i>							
Control	35.60	48.72	7.61	93.77	35.84	10.54	12.64
Disorder	15.09	484.41	1.31	37.21	13.48	13.11	5.73
	***	***	*	*	***	NS	NS

[†] Boron (B), copper (Cu), iron (Fe), manganese (Mn), molybdenum (Mo), and zinc (Zn).

[‡] *, **, or *** indicate statistically significant differences between sample means based on *F* tests at $P < 0.05$, $P < 0.01$, or $P < 0.001$, respectively. NS (not significant) indicates the *F* test difference between sample means was $P > 0.05$.

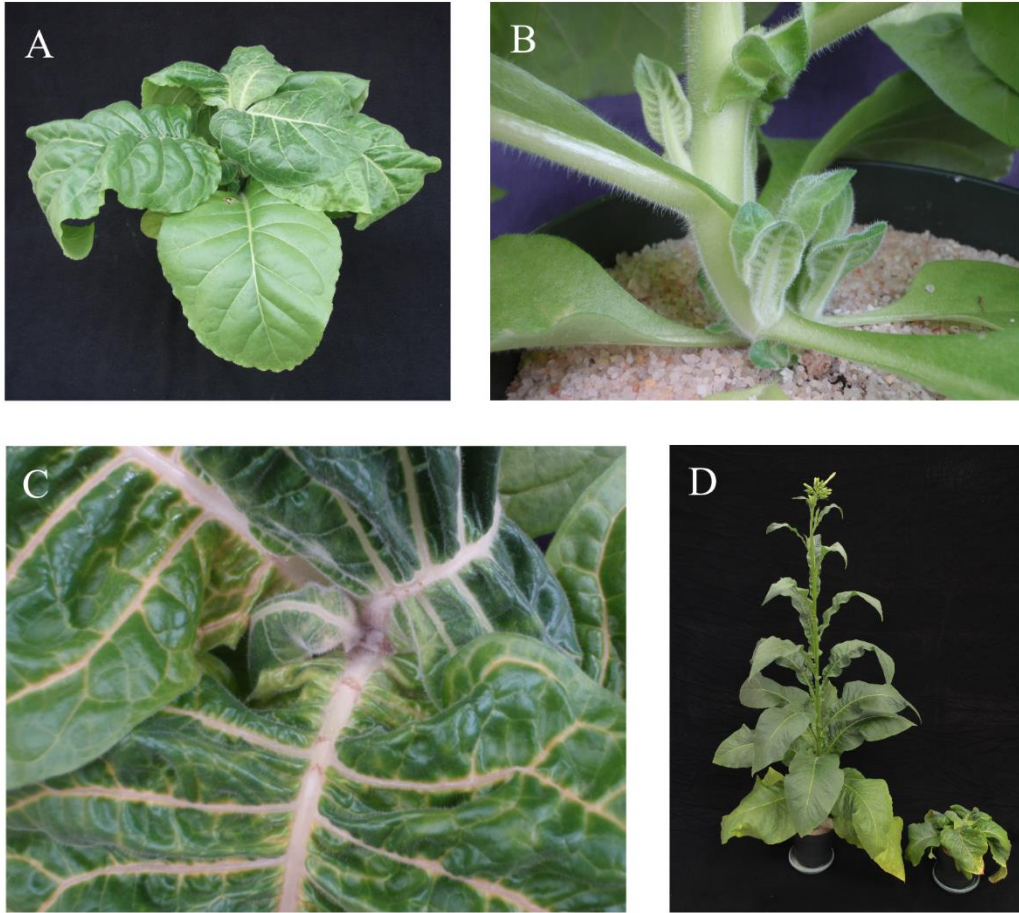


Figure 3.1. Boron-deficient tobacco with (A) thickened and distorted foliage, (B) axillary shoot development at the nodes, (C) death of the apical meristem, chlorosis along the veins, and (D) compared with a much larger control plant.



B



Figure 3.2. Boron toxicity symptoms (A) on the lower foliage of a flue-cured tobacco plant, and (B) along the margins a single leaf.

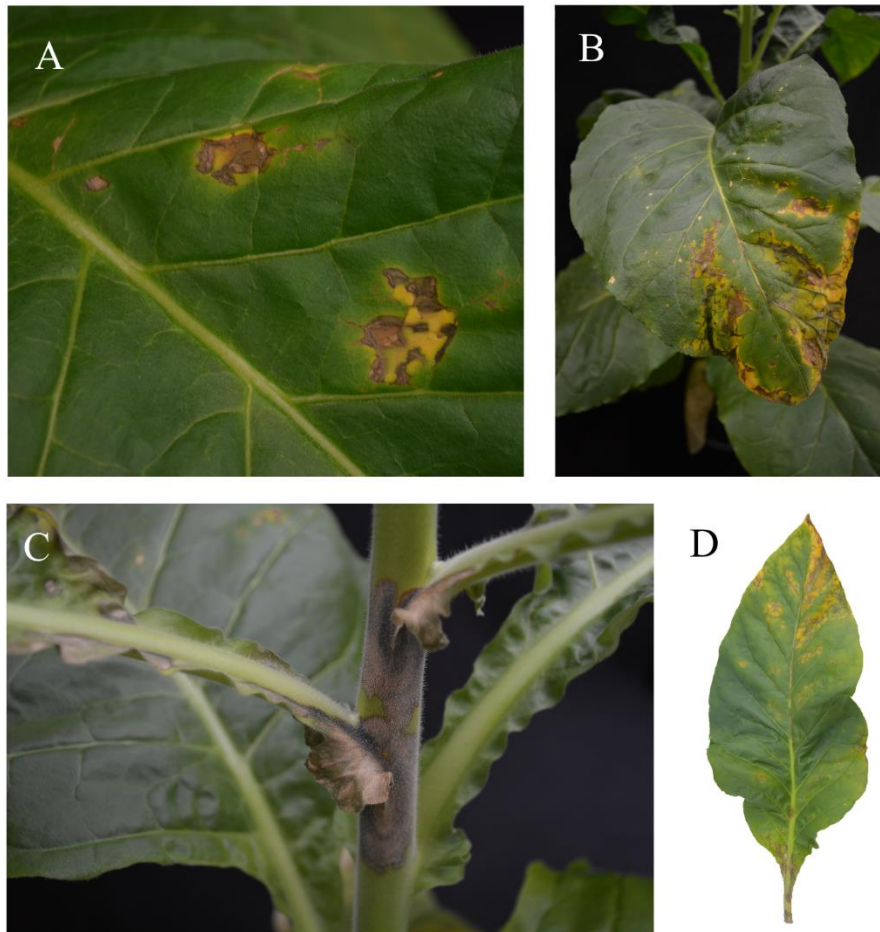


Figure 3.3. Copper deficiency symptoms of (A) small chlorotic and necrotic spotting, (B) large chlorotic and necrotic areas with black veins, (C) blackened necrosis at the base of the petiole, and (D) advanced symptoms primarily at the leaf tip and petiole.



Figure 3.4. Upper leaves of a control tobacco plant receiving all essential nutrients (left) compared to a tobacco plant displaying iron deficiency symptoms (right).

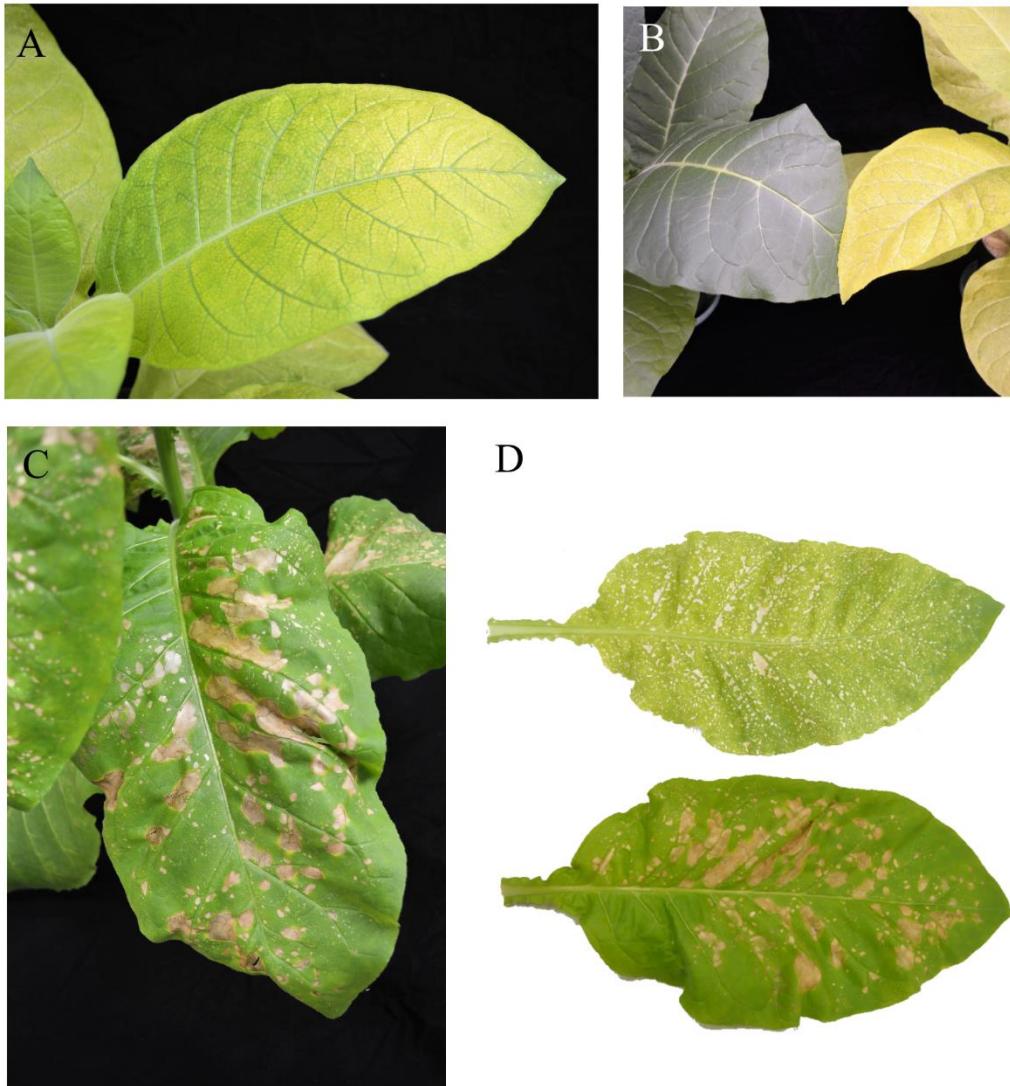


Figure 3.5. Manganese deficiency symptoms of netted chlorosis (A) on the upper foliage of a burley tobacco plant and (B) compared to the upper foliage of a control burley plant. Symptoms of Mn deficiency (C) were different on flue-cured tobacco plants, which exhibited a much greener coloration with larger necrotic spots. Symptomatic leaves (D) of burley (top) and flue-cured (bottom) tobacco were different when compared side-by-side.

CHAPTER 4

Spectroscopic Differentiation of Nutrient Disorders in Greenhouse Grown Flue-Cured

Tobacco

(Written in the style of Agronomy Journal)

Spectral Discrimination of Macronutrient Deficiencies in Greenhouse Grown Flue-Cured Tobacco

Core Ideas:

- Tobacco plants grown in sand culture developed several different symptoms.
- Spectral data from several maturity stages demonstrated statistical differences.
- Models were developed for macronutrient deficiency classification.

Abstract

Remotely sensing spectral reflection enables detection of nutrient deficiencies, drought stress, and other aspects of plant health. Past plant nutrition research primarily investigated N, P, or K deficiencies in a limited number of crops, but few studies have used a holistic approach to spectrally discriminate among several nutrient deficiencies within the same crop. This study was conducted to provide baseline spectral characterization of N, P, K, Mg, and S deficiencies, the most common nutrient disorders observed in flue-cured tobacco (*Nicotiana tabacum* L.). Reflectance measurements were obtained from nutrient deficient plants at several stages of development. Feature selection methods including information entropy and first and second derivatives were used to identify wavelengths useful for discriminating among these deficiencies. These methods demonstrated that most of the important variability could be obtained from wavelengths in the visible spectrum, while near-infrared and shortwave-infrared radiation contributed little to the observed variability. Principal component analysis was used to reduce data dimensionality and the selected components were used to develop linear discriminant analysis models to classify the symptoms. Classification models for young, intermediate, and

mature plants had overall accuracies of 92%, 82%, and 75%, respectively when using 10 principal components. Nitrogen, S, and Mg deficiencies typically exhibited greater classification accuracies while P and K demonstrated poor or inconsistent results. Overall, this study demonstrates that spectral analysis of flue-cured tobacco is a promising methodology to significantly improve current scouting methods.

Abbreviations: DI, deionized; EMR, electromagnetic radiation; FIA, flow injection analysis; FOV, field of view; ICP-MS, inductively coupled plasma mass spectrometry; LDA, linear discriminant analysis; NIR, near-infrared; PAR, photosynthetically active radiation; PC, principal component; PCA, principal component analysis; PLSR, partial least squares regression; PVC, polyvinyl chloride; SPAD, Soil-Plant Analysis Development; UV, ultraviolet; UAV, unmanned aerial vehicle.

Introduction

Remote sensing of nutrient disorders enables growers to rapidly scout their crops and manage fertilization practices with greater precision. Automation using spectral sensors mounted to trucks, tractor spray booms, or unmanned aerial vehicles (UAVs) is becoming more common in agricultural production settings (Abdel-Rahman et al., 2010; Yang et al., 2016). Spectral sensors measure crop reflectance at various wavelengths in the electromagnetic spectrum, which can be correlated to the symptoms of specific nutrient disorders. Plants exposed to various biotic and abiotic stressors exhibit different visual symptoms due in part to changes in how light interacts with plant tissues (Abdel-Rahman et al., 2010; Behmann et al., 2014). This characteristic enables spectral sensors to diagnose plant health problems before symptoms are

visually apparent (Behmann et al., 2014). For instance, Osborne et al. (2002) found several wavelengths in the visible and near-infrared (NIR) spectra that could be used to estimate N content in corn. Zhang et al. (2013) reported several wavelengths that were correlated with N, P, or K deficiencies in rapeseed (*Brassica napus* L.). These studies demonstrate that spectral signatures can be correlated to specific nutrient disorders and can then be used to distinguish among disorders.

Certain wavelengths are already associated with plant stress in general and nutrient stress specifically. Many of these bands fall within the red edge, the portion of the spectrum between the visible red and NIR spectra. These wavelengths are located at approximately 700, 720, and 740 nm (Thenkabail et al., 2019). Other wavelengths of interest fall in the blue, (375, 466, and 490 nm), green (515, 520, 525, 550, and 575 nm) and red (675 and 682 nm) spectra (Thenkabail et al., 2019). These wavelengths have been used to classify nutrient stress or pigment changes (Thenkabail et al., 2019). Soil-Plant Analysis Development (SPAD) meters emit targeted electromagnetic radiation (EMR) near 650 and 940 nm and subsequently measure the amount of radiation transmitted through the leaf (Daughtry et al., 2000). The values obtained from these sensors provide a measure of the green (high values) or yellow (low values) coloration exhibited in the foliage (Daughtry et al., 2000). These values correlate to leaf chlorophyll concentrations which in turn correlate to leaf N concentrations. The primary goals of plant spectral analysis in terms of plant nutrition are the detection and discrimination of nutrient disorders or estimating foliar nutrient concentrations.

Rustioni et al. (2018) reported successful discrimination among N, K, Mg, and Fe deficiencies in grape (*Vitis vinifera* L.) leaves using hyperspectral reflectance measurements. The effects of each deficiency on foliar pigment concentrations leads to the observed spectral

differences (Rustioni et al., 2018). Other studies by Adams et al., (2000a, 2000b) demonstrate spectral separability of various micronutrient deficiencies. They found that Cu-deficient leaves were most successfully distinguishable and Mn-deficient leaves were also distinguishable in many cases; however, Fe and Zn deficiencies were more difficult to classify (Adams et al., 2000b). Adams et al. (2000a) suggested that Cu, Fe, and Mn may affect spectral reflectance due to their specific roles in chlorophyll synthesis and electron transport.

Although there are at least 17 essential elements required to complete the cycle of plant growth and maturation, monitoring macronutrient status is considered most important for maintaining crop quality and yield. The essential macronutrients including N, P, K, Ca, Mg, and S are needed in relatively high concentrations (Mitra, 2017). Each of the essential nutrients perform crucial roles in plant development and deficiencies of each nutrient cause unique symptoms that are visually diagnosable in many instances. Some of the primary effects of nutrient deficiencies include stunting and changes in leaf shape or orientation (Römheld, 2012). Nutrient deficiencies often cause changes in foliar coloration which may appear yellow (chlorotic), white (bleached), brown (necrotic), red, or black (Römheld, 2012). It is important to consider that the mobility of nutrients within plant tissues also dictate the location symptoms occur. For instance, deficiencies of mobile nutrients such as N, P, K, and Mg typically lead to symptom development on the mature lower foliage while relatively immobile nutrients such as Ca and S cause symptoms to develop on the upper foliage. Additionally, the pattern and distribution of symptoms on a single leaf are important to consider when diagnosing symptoms.

Henry et al. (2018a, 2018b) induced nutrient disorders of flue-cured tobacco and provided detailed descriptions of the symptoms exhibited from each deficiency and toxicity. The results indicated that several nutrient disorders were readily induced, and symptoms had unique

characteristics that made them visually distinguishable. Nitrogen deficiency appeared as a pale-yellow chlorosis that occurred uniformly on individual leaves but was more severe on the lower leaves. (Henry, 2018a). Similarly, S deficiency led to symptoms of pale chlorosis; however, these symptoms occurred uniformly throughout the canopy (Henry et al., 2018a). Phosphorus deficiency resulted in symptoms of nonuniform chlorosis on the lower leaves with olive-green leaf spots and large necrotic lesions (Henry, 2018a). Potassium deficiency led to the development of marginal chlorosis on the lower to central leaves, while Mg deficiency caused symptoms of interveinal chlorosis in the same region of the plant (Henry, 2018a).

The purpose of this study was to determine if macronutrient deficiency symptoms could be distinguished among one another using spectral reflectance data. We hypothesized that discrimination of certain nutrient deficiencies would be more successful than others. In particular, we believed the symptoms of N and S deficiencies would be difficult to uncouple due to their visual similarities. This study was achieved by inducing N, P, K, Mg, and S deficiencies in a controlled environment and recording the spectral reflectance from each disorder at different stages of plant maturity.

Materials and Methods

Plant Material and Experimental Design

The experiment was replicated twice over time beginning 9 Apr. and 7 June 2018. Each replication began by sowing pelletized K-326 tobacco seeds (GoldLeaf Seed Co., Hartsville, SC) into 128-cell plug flats and placing them in a glass-glazed greenhouse at North Carolina State University in Raleigh, NC (35°47'41" N lat, 78°41'57" W long). The substrate was an 80:20 (v:v) mix of Canadian sphagnum peat moss (Conrad Fafard, Agawam, MA) and horticultural

coarse perlite (Perlite Vermiculite Packaging Industries, Inc., North Bloomfield, OH), amended with mesh size #100 dolomitic limestone (Rockydale Agricultural, Roanoke, VA) at 8.9 kg m^{-3} and wetting agent (AquaGro 2000 G; Aquatrols, Cherry Hill, NJ) at 0.6 kg m^{-3} . This custom substrate was used to limit nutrient contamination that would be present in a commercial substrate. Flats were irrigated by hand with nonfertilized water until seeds germinated and cotyledons fully expanded.

Following germination, seedlings were fertilized with a solution consisting of 7.5 mmol L^{-1} N, 0.5 mmol L^{-1} P, 3.0 mmol L^{-1} K, and 2.5 mmol L^{-1} Ca. Previous experiments demonstrated tobacco seedlings require a low concentration of primary macronutrients to develop sufficiently for studies investigating nutrient disorders (Henry et al., 2018a, 2018b). The selected concentrations were a half rate of the primary macronutrient concentrations used in the nutrient-sufficient control solution. The control solution was a modified all-nitrate Hoagland solution consisting of 15.0 mmol L^{-1} N, 1.0 mmol L^{-1} P, 6.0 mmol L^{-1} K, 5.0 mmol L^{-1} Ca, 2.0 mmol L^{-1} Mg, and 2.0 mmol L^{-1} S, $72.0 \text{ } \mu\text{mol L}^{-1}$ Fe, $18.0 \text{ } \mu\text{mol L}^{-1}$ Mn, $3.0 \text{ } \mu\text{mol L}^{-1}$ Cu, $3.0 \text{ } \mu\text{mol L}^{-1}$ Zn, $45.0 \text{ } \mu\text{mol L}^{-1}$ B, and $0.1 \text{ } \mu\text{mol L}^{-1}$ Mo (Hoagland and Arnon, 1950) mixed with deionized (DI) water of 18 megohm purity. All nutrients were provided by the following technical grade salts (Fisher Scientific, Pittsburg, PA): $\text{Ca}(\text{NO}_3)_2 \cdot 4\text{H}_2\text{O}$, KNO_3 , KH_2PO_4 , K_2SO_4 , $\text{MgSO}_4 \cdot 7\text{H}_2\text{O}$, KCl , $\text{CaCl}_2 \cdot 2\text{H}_2\text{O}$, NaNO_3 , $\text{NaH}_2\text{PO}_4 \cdot 2\text{H}_2\text{O}$, iron chelate (Fe-DTPA), $\text{MnCl}_2 \cdot 4\text{H}_2\text{O}$, $\text{ZnCl}_2 \cdot 7\text{H}_2\text{O}$, $\text{CuCl}_2 \cdot 2\text{H}_2\text{O}$, H_3BO_3 , and $\text{Na}_2\text{MoO}_4 \cdot 2\text{H}_2\text{O}$. Solution pH was adjusted to ~ 6.0 using NaOH. Macronutrient deficiencies were induced by replacing each cation (K and Mg) or anion (NO_3 , H_2PO_4 , and SO_4) containing salt with a Na or Cl containing salt, respectively. Fertilizer treatments began upon transplanting into a sand culture system.

The seedlings were thoroughly drenched with DI water three consecutive times to leach any remaining nutrients prior to transplant. Seedlings were transplanted into 12.4 cm diameter pots (Dillen, Middlefield, OH) filled with silica sand [Millersville #2 (0.8 to 1.2 mm diameter); Southern Products & Silica Co., Hoffman, NC] that was soaked in sulfuric acid and triple-rinsed with DI water prior to use. The transplanted seedlings were placed into an automated recirculating sand culture system (Appendix A1) on 1 May and 21 June 2018. The system was built on benches in a glass-glazed greenhouse in Raleigh, NC and utilized a completely randomized design. Each segment of the system (referred to as “lines” hereafter) consisted of 10.2 cm diameter polyvinyl chloride (PVC) piping (Charlotte Plastics, Charlotte, NC) fit with 12.7 cm diameter PVC reducer couplings (Charlotte Plastics). Six couplings were used to hold pots and recapture irrigation solutions in each line. Fertilizer solutions were delivered via drip tubes fed from individual 20 L plastic buckets equipped with submersible pumps (model 1A; Little Giant Pump Co., Oklahoma City, OK). Each line contained one treatment. Solutions were delivered for 1 min each cycle with as many cycles necessary per day to prevent apparent water stress (i.e., wilting) between 6:00 and 18:00 hr. Nutrient solutions were replaced on a weekly basis.

Spectroscopic Measurements

A handheld spectrometer (PSM-2500; Spectral Evolution, Lawrence, MA) was used to collect spectral reflectance data throughout the study. The sensor had a spectral range of 300 to 2,500 nm and a spectral resolution of 3.5 nm at 700 nm, 22 nm at 1,500 nm, and 22 nm at 2,100 nm with the percent reflectance output in 1 nm increments. The sensor was equipped with a fiberoptic leaf clip capable of taking leaf-level measurements. This leaf clip had a self-contained

light source with two light settings, of which, the higher setting was used. Leaf clip measurements were taken inside the greenhouse under ambient light conditions. Measured plants were irrigated prior to measurement to ensure drought stress would not be a confounding factor.

Throughout the experiment, symptomatic and asymptomatic control plants were selected to obtain hyperspectral measurements of the individual leaves. At each measurement date, four individual plant replicates were selected. Reflectance data were collected from each leaf, except for the small bottom two to three leaves exhibiting natural senescence and the few immature upper leaves that were narrow with limited expansion. Measurements using the leaf clip were taken approximately 2 to 3 cm from the leaf margin and one-third of the leaf length away from the leaf tip. This location was selected because it typically represented the average degree of symptoms for each leaf. Areas of necrosis were avoided as necrotic tissues reflected much different patterns than non-necrotic tissues, regardless of symptomology.

Leaf Tissue Analysis

Leaf tissues were dried at 70 °C for 72 hr and then ground in a sample mill (Thomas Wiley® Mini-Mill; Thomas Scientific, Swedesboro, NJ), and analyzed for nutrient concentrations (AgSource Laboratories, Lincoln, NE). Total N was processed by Kjeldahl digestion and determined via flow injection analysis (FIA). Extractable K was processed by 2% acetic acid digestion and determined via inductively coupled plasma mass spectrometry (ICP-MS). Total P and all other plant minerals were processed by nitric acid/hydrogen peroxide digestion and determined via ICP-MS. Pairwise differences between control and deficient plant foliar nutrient concentrations were determined using PROC ANOVA in SAS (version 9.4; SAS Institute, Cary, NC).

Data Preparation

Reflectance data were manipulated and analyzed using R statistical software (R Core Team, 2019). Measurements from each leaf of each treatment were assigned into several subgroups depending on various characteristics. Leaves received an objective symptom severity rating of four possible categories: 1) none, 2) low, 3) intermediate, or 4) high (Figure 4.1). Examples of leaves from each category can be seen in Figure 4.1. Furthermore, measurement stages were separated by maturity: 1) young, 2) intermediate, or 3) mature. Young plants were those that had 6 or fewer leaves, intermediate plants had 7 to 12 leaves, and mature plants had more than 12 leaves. Fully mature tobacco plants developed between 18 and 20 expanded leaves prior to anthesis.

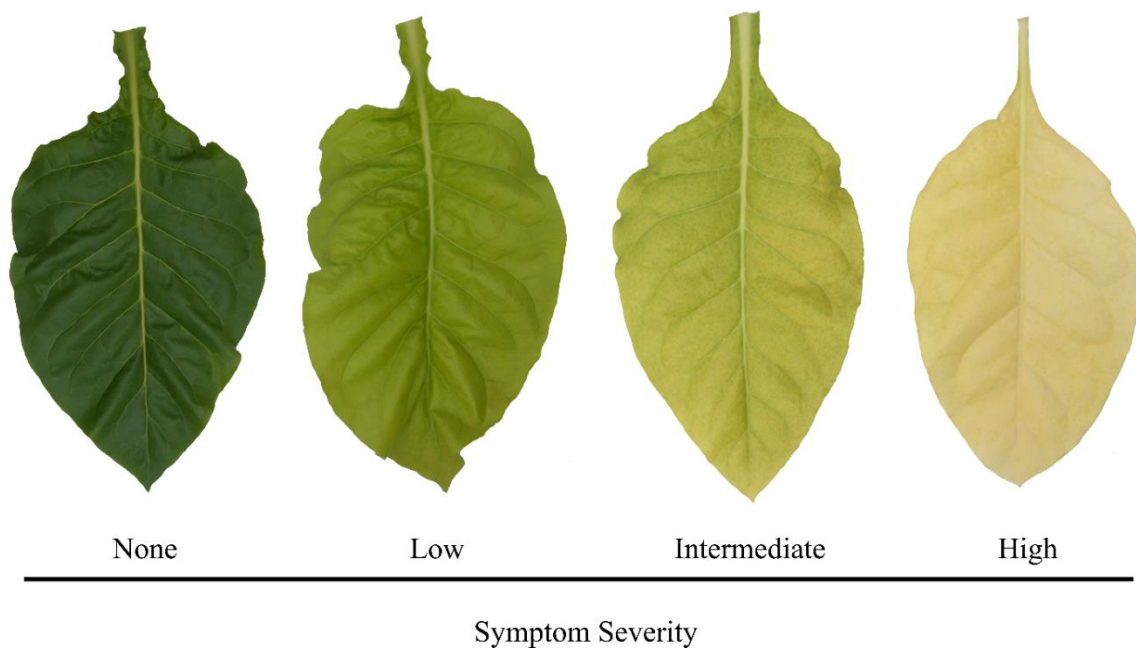


Figure 4.1. Demonstration of the flue-cured tobacco (*Nicotiana tabacum* L.) symptom severity rating system using N deficiency as an example.

Band Selection

Spectra were used to calculate information entropy as well as first and second spectral derivatives to identify which wavelengths contribute most to the variability observed among the nutrient-deficient leaves. Information entropy is a measurement for how much variability is contained within a band and it is commonly used for hyperspectral band selection (Bajcsy and Groves, 2004; Bajwa et al., 2004; Xie et al., 2017). Derivative measures are also useful for band selection by identifying areas with rapid changes in direction or pattern within spectra (Bajcsy and Groves, 2004). Information entropy was calculated using the FSelector package (Romanski and Kotthoff, 2018) while derivatives were calculated using the prospectr package (Stevens and Ramirez-Lopez, 2014) in R. Savitzky-Golay filtering was applied with a window size of 10 bands to information entropy data to reduce noise and smooth the data. Derivatives were calculated and smoothed using the gap-segment algorithm with a filter length of 11 bands for both first and second order derivatives. Peaks and valleys were then calculated using the splus2R package (Constantine et al., 2016) to determine the greatest individual absolute values or ranges of values within a span of 10 bands. Ranges of continuous values with uniform importance were aggregated and used to determine the central wavelength representing that range. The identified wavelengths represented those with the greatest impact on observed variability.

Symptom Classification

Reflectance spectra were analyzed by growth stage using principal component analysis (PCA), with 10 principal components (PCs) selected for each growth stage. Linear discriminant analysis (LDA) was used to develop classification models to distinguish among the various symptoms. The classification models were conducted using a (custom-built) five-fold cross

validation approach, where 80% of the data was randomly selected for model training and the remaining 20% used for testing. Following the first validation, a second validation was conducted with a new set of testing data previously used to train the model. This process was repeated to optimize the model until all data were used for both training and testing functions. The final classification results were put into a confusion matrix for each growth stage and analyzed using the PredPsych package (Koul et al., 2018) in R. The matrices were used to determine the overall accuracy and misclassification rates for each model. Overall accuracy was calculated by dividing the number of correctly classified observations by the total number of observations.

Results and Discussion

Plants grown in each nutrient deficient environment exhibited symptoms similar to those described by Henry et al. (2018a). Nitrogen-, P-, and Mg-deficient plants always developed symptoms on the lower leaves first, regardless of growth stage. Young K-deficient plants developed symptoms on the lower leaves first, but mid and late stage plants exhibited symptoms primarily on the leaves within the middle third of the plant. Sulfur-deficient plants began developing symptoms on the upper foliage, spreading down the plant. Nitrogen-deficient (Figure 4.2A) and S-deficient (Figure 4.2E) plants both developed substantial chlorosis that eventually turned to complete foliar bleaching. Phosphorus-deficient plants developed nonuniform chlorosis with necrotic spotting (Figure 4.2B). Additionally, P-deficient leaves permanently lost their rigidity, appearing wilted with a noticeably pliable texture. Potassium-deficient plants developed the characteristic symptom of “firing” which consists of marginal chlorosis and necrosis (Figure 4.2C). Magnesium-deficient plants developed an interveinal chlorosis which turned to bleaching

between the veins and downward curling leaf margins (Figure 4.2D). Control plants consistently had higher foliar concentrations of the particular deficient nutrient than the nutrient deficient plants at all maturity levels (Table 4.1).

Various trends were exhibited among the mean reflectance spectra of plants grown with each deficiency (Figure 4.2). Each deficiency exhibited higher average reflectance in the visible spectrum compared to that of control plants (Figure 4.2). This was likely due to higher photosynthetic rates coinciding with greater absorption of photosynthetically active radiation (PAR). Nitrogen-deficient leaves exhibited the highest average reflectance in all parts of the visible spectrum (Figure 4.2A). Additionally, these N-deficient leaves exhibited the greatest shift in the red edge (Figure 4.2A). Phosphorus-deficient leaves reflected similarly to the control in the ultraviolet (UV), red edge, and NIR regions but had higher reflectance of green, yellow, and red EMR (Figure 4.2B). Potassium-deficient plants had higher reflectance in the blue, green, yellow, and red regions but had lower reflectance in the NIR (Figure 4.2C). Similarly, Mg-deficient plants had lower reflectance in the NIR with higher reflectance primarily in the green and yellow regions (Figure 4.2D). Although appearing visually similar to N-deficient leaves, S-deficient leaves reflected far less visible EMR than the N-deficient leaves (Figure 4.2E). In fact, the spectral profile of S-deficient plants appeared more similar to that of Mg-deficiency.

Table 4.1. Pairwise comparisons of foliar nutrient concentrations found in the most recently matured leaves of young, intermediate, and mature flue-cured tobacco (*Nicotiana tabacum* L.) plants grown under macronutrient deficient conditions.

Treatment	-N	-P	-K	-Mg	-S
Foliar nutrient concentration (%)					
Element	N	P	K	Mg	S
<i>Young</i>					
Control	5.10a †	0.41a	5.87	0.66_	0.35a
Deficient	0.86b	0.06b	—	—	0.10b
<i>Intermediate</i>					
Control	3.17a	0.11a	4.46a	0.74a	0.32a
Deficient	0.92b	0.05b	0.34b	0.01b	0.09b
<i>Mature</i>					
Control	2.47a	0.10a	3.37a	0.84a	0.33a
Deficient	0.81b	0.04b	0.27b	0.01b	0.06b

† Within column-ordered pairs grouped by plant maturity, means followed by the same letter are not significantly different according to Tukey's HSD (0.05).

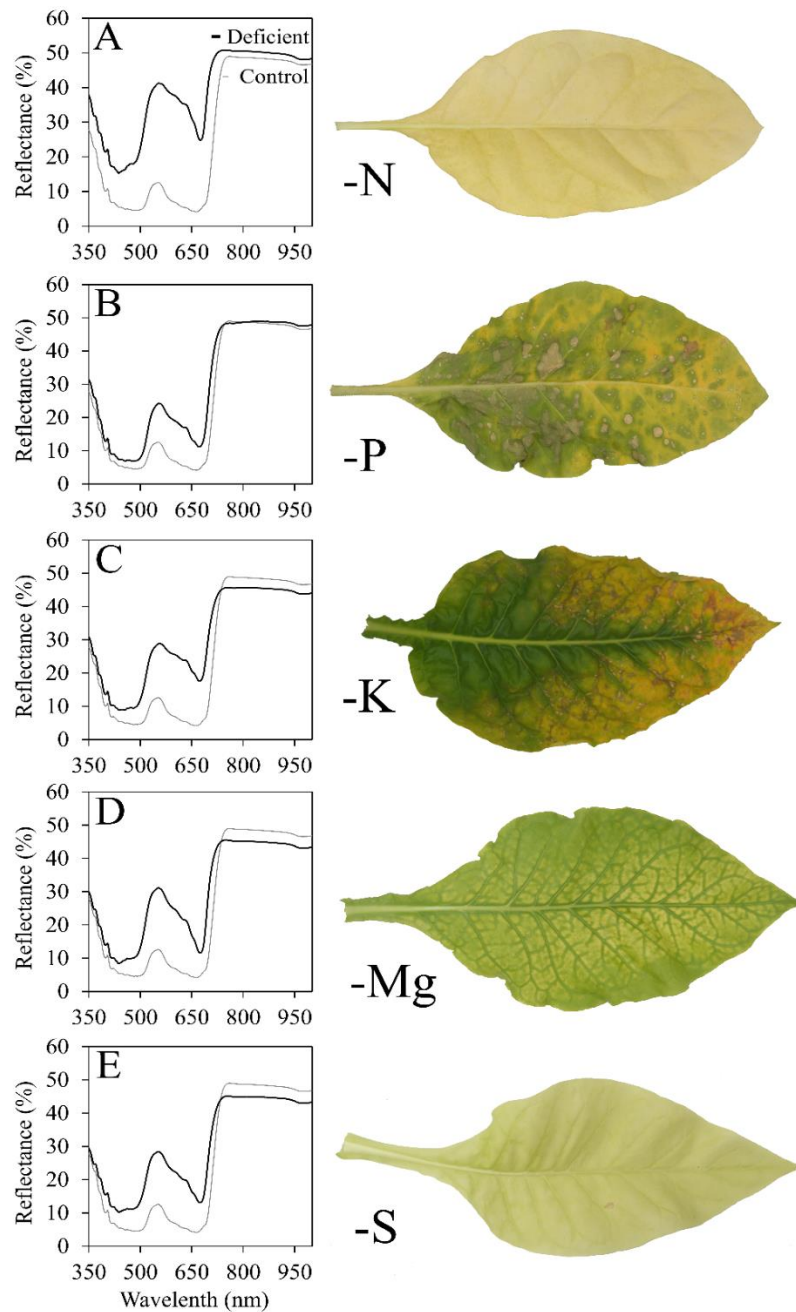


Figure 4.2. Average spectra and associated leaf appearance for (A) nitrogen, (B) phosphorus, (C) potassium, (D) magnesium, and (E) sulfur deficiencies in flue-cured tobacco (*Nicotiana tabacum* L.).

Average spectra of severely N-deficient leaves demonstrate greater reflectance than control leaves at every wavelength from 350 to 1000 nm (Figure 4.3A). Some of the major

differences observed between N-deficient and control leaf spectra was observed in the green and yellow regions of the visible spectrum, with reflectance peaking near 550 nm at approximately 41.1% as opposed to 12.6% in control plants (Figure 4.3A). Control plants also exhibited similar reflectance of red (~650 nm) and blue (~450 nm) EMR, while N-deficient plants reflected higher quantities of red EMR proportionally (Figure 4.3A). Furthermore, raw spectral derivatives illustrated some of the primary areas of interest due to significant changes in slope. For instance, the first spectral derivatives for control and N-deficient plants both exhibited prominent peaks near 550 and 700 nm (Figure 4.3B). However, upon closer inspection, these two peaks illustrate the shift in the red edge from higher wavelengths in control plants to lower wavelengths in N-deficient plants (Figure 4.3B). These trends are also exhibited in the second derivatives, but less so and with significantly more noise, demonstrating the need to implement smoothing techniques (Figure 4.3C).

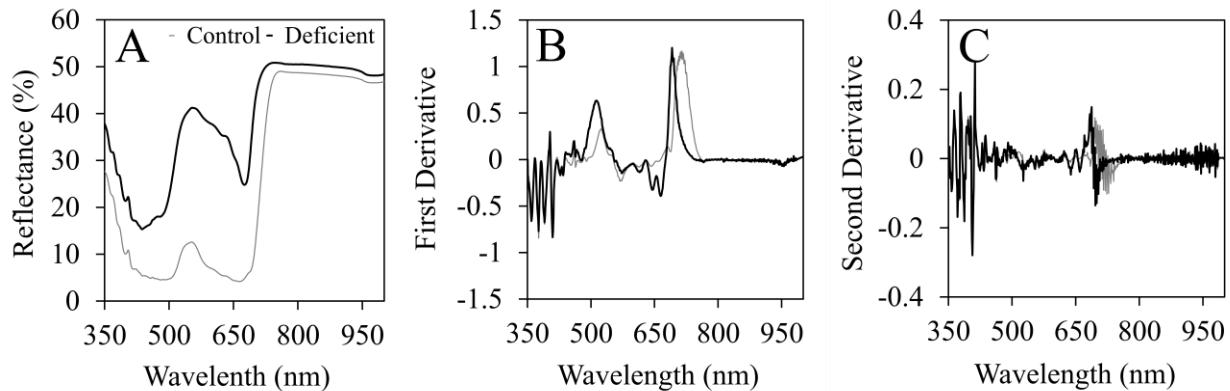


Figure 4.3. Graphs illustrating A) the average spectral reflectance from 350 to 1000 nm for severely N-deficient flue-cured tobacco (*Nicotiana tabacum* L.) compared to the average control

spectra, B) the first derivatives of the N-deficient and control spectra, and C) the second derivatives of the N-deficient and control spectra.

Band Selection

Both information entropy and spectral derivative methods were able to successfully identify wavelengths that could explain the variability observed among symptoms (Table 4.2). In general, the majority of observed variability could be explained by wavelengths in the visible spectrum. Information entropy resulted in several peaks at 400, 423, 502, 530, 557, 618, 638, 657, and 697 nm for young plants (Figure 4.4A), 414, 520, 586, 610, 655, and 700 nm for intermediate maturity plants (Figure 4.4B), and 376, 398, 460, 546, 565, 597, and 701 nm for mature plants (Figure 4.4C). The highest peaks were typically between 500 and 650 nm as well as a specific peak at 700 nm. Plants at each growth stage exhibited a similarly steep decreasing trend between 700 and 750 nm, coinciding with the red edge.

Several wavelengths were selected based on first and second derivative spectra (Table 4.2). Wavelengths selected from the first derivative spectra for young plants included 368, 383, 414, 517, 573, 613, 648, 699, and 951 nm (Figure 4.5A). Second derivative spectra resulted in the selection of 394, 413, 425, 501, 534, 584, 683, 716, and 965 nm (Figure 4.5A). Wavelengths selected from the first spectral derivative of intermediate maturity plants were 369, 383, 414, 518, 573, 613, 647, 702, and 951 nm (Figure 4.5B). Wavelengths selected from second derivatives included 394, 413, 425, 501, 535, 584, 683, 725, and 965 nm for intermediate maturity plants (Fig. 5B). Finally, mature plants had selected wavelengths of 369, 383, 415, 519, 573, 612, 647, 704, and 951 nm for first derivative, and 393, 413, 425, 503, 536, 584, 685, 728, and 965 nm for second derivative spectra (Figure 4.5C).

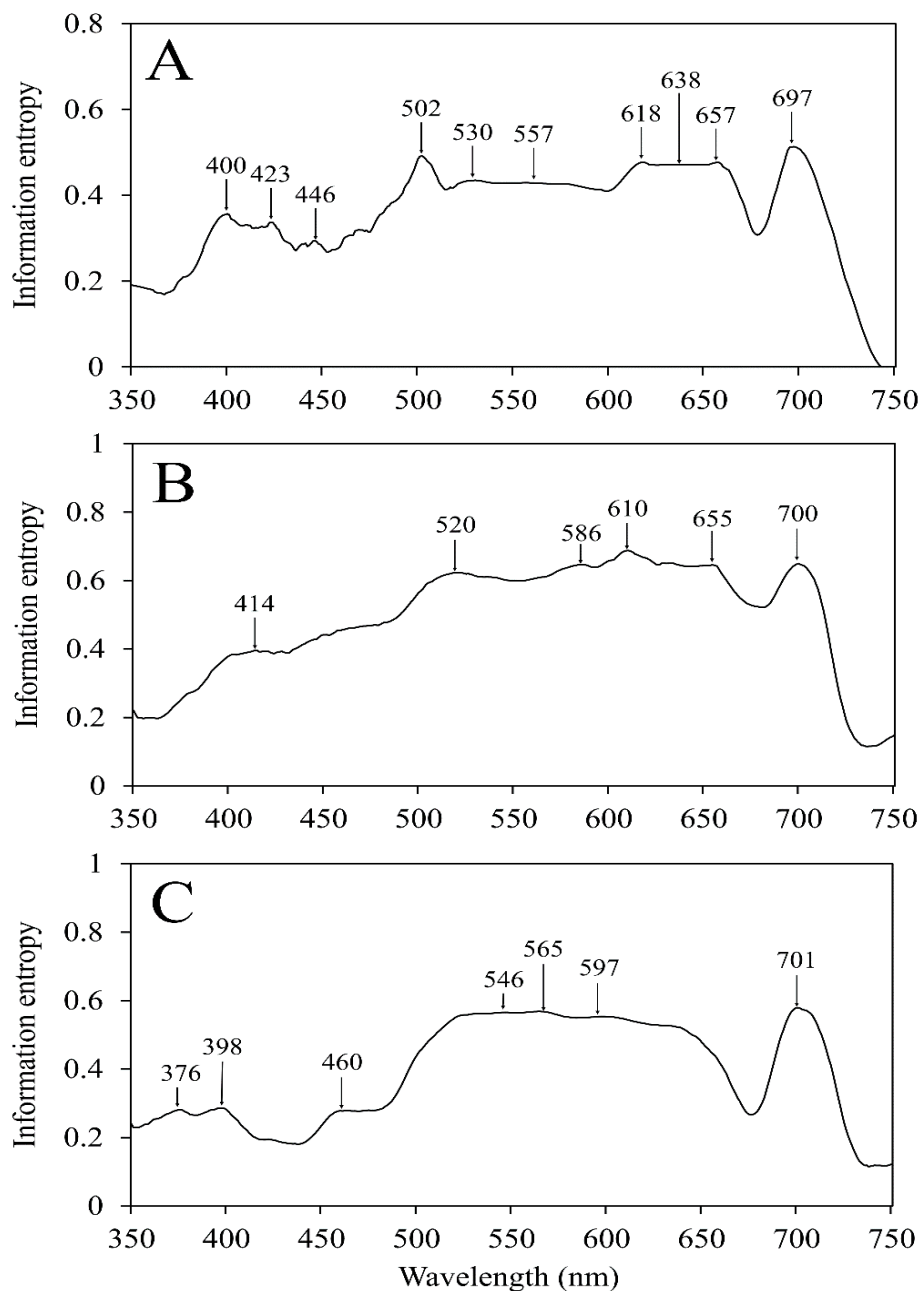


Figure 4.4. Savitzky-Golay filtered information entropy observed among (A) young, (B) intermediate, and (C) mature flue-cured tobacco (*Nicotiana tabacum* L.) plants. Peak wavelengths demonstrate locations with the most informative bands necessary to distinguish among each nutrient deficiency.

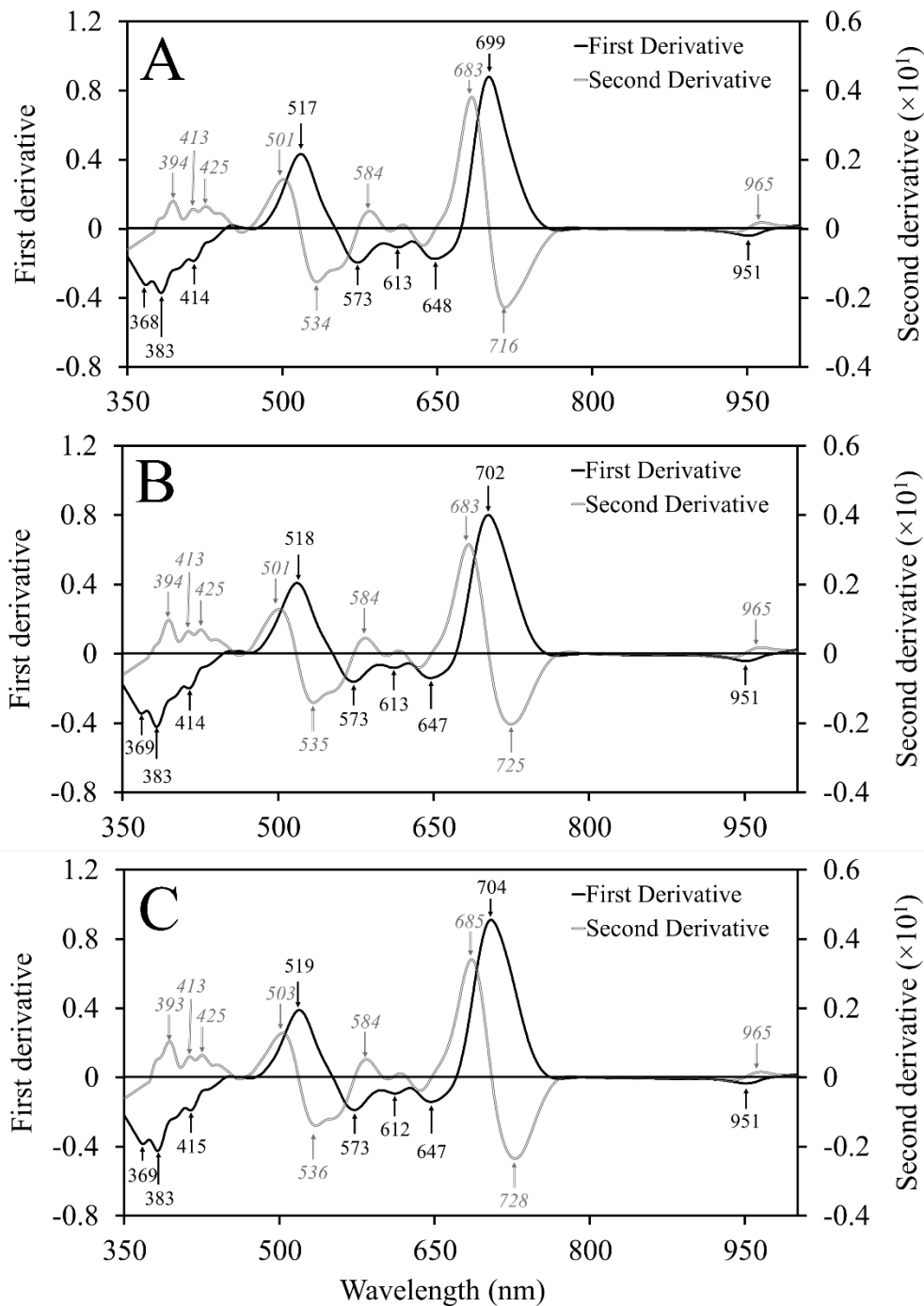


Figure 4.5. First and second derivatives of (A) young, (B) intermediate, and (C) mature flue-cured tobacco (*Nicotiana tabacum* L.) plants smoothed using the gap-segment algorithm. Peak wavelengths demonstrate locations with the most informative bands necessary to distinguish among each nutrient deficiency.

- 1 Table 4.2. Five most significant wavelengths (nm) selected for discrimination among macronutrient deficiencies in flue-cured tobacco
- 2 (*Nicotiana tabacum* L.) at three growth stages. Band selection methods included information entropy, first spectral derivative, and
- 3 second spectral derivative.

Information entropy			First derivative			Second derivative		
Young	Intermediate	Mature	Young	Intermediate	Mature	Young	Intermediate	Mature
697	700	701	699	702	704	683	683	685
502	610	565	517	518	519	716	725	728
657	655	546	383	383	383	534	535	536
618	586	597	368	369	369	501	501	503
638	520	398	648	414	573	394	394	393

4

Li et al. (2018a) studied hyperspectral reflectance for estimating N in upper, middle, and lower leaves of oilseed rape plants. They used partial least squares regression (PLSR) and reported optimal wavelengths of 437, 565, 667, 724, 993, 1084, and 1189 nm for upper leaves, 423, 570, 598, 659, 725, and 877 nm for middle leaves, and 420, 573, 597, 667, and 718 nm for lower leaves (Li et al., 2018a). Li et al. (2018b) also used PLSR to model and predict foliar N and P concentrations in oilseed rape. They compared PLSR with other data transformations such as first derivatives and continuum removal and found that PLSR with first derivatives was most effective for nutrient estimation. Optimal wavelengths selected for N were 445, 556, 657, 764, 985, 1082, and 1994 nm while those selected for P included 755, 832, 891, 999, 1196, and 1267 nm (Li et al., 2018b). Zhang et al. (2013) investigated the spectral response of oilseed rape to N, P, and K deficiencies using PLSR. They reported optimal wavelengths of 440, 473, 513, 542, 659, 718, 744, 865, 928, 965, 986, and 1015 nm for N, 468, 522, 698, 721, 817, 967, 979, and 1025 nm for P, and 456, 554, 667, 720, and 1027 nm for K (Zhang et al., 2013).

These past studies demonstrate similar results to what we obtained in the present study. In general, the majority of observed variation appears to be in the visible spectrum and falls specifically between 400 and 750 nm. However, other studies reported several significant wavelengths >800 nm (Li et al., 2018a 2018b; Zhang et al., 2013), which was not the case in our study. Furthermore, we identified bands of interest in the UV region, whereas most other studies did not. This may be due in part to the specific spectroradiometer used in this study. Also likely is that the species and nutrient deficiencies used in this study were different from the other studies, and plants are known to demonstrate different spectral responses by species (Thenkabail et al., 2019) and in response to different stimuli. Further work should investigate whether UV EMR is a good indicator of nutrient deficiencies in species other than tobacco.

Symptom Classification

Principal component analysis resulted in high accuracies while greatly reducing the data dimensionality. With just 10 PCs used in each model, dimensionality was reduced by more than 95% as we were able to combine our original 2250 bands into 10 linear combinations of bands that capture most of the variability. This method was also found to successfully reduce dimensionality in other studies investigating plant spectral response (Bajcsy and Groves, 2004; Bajwa et al., 2004). Information entropy and PCA are both cited as useful methods for selecting bands containing the most information in regards to variability (Bajcsy and Groves, 2004). The LDA model for young plants resulted in 92% overall accuracy with individual accuracies of 92%, 100%, 88%, and 90% for control, N-deficient, P-deficient, and S-deficient plants, respectively (Table 3). The most common misclassification for young plants was between S deficiency and the control, with several S-deficient plants being classified as controls, and some controls classified as S-deficient.

Overall accuracy for intermediate maturity plants was lower than for young plants at 82%. Classification accuracies for control, N-deficient, P-deficient, K-deficient, Mg-deficient, and S-deficient plants were 94%, 92%, 58%, 70%, 79%, and 80%, respectively (Table 4.3). Nitrogen-deficient plants were successfully classified in most instances, but some N-deficient plants were misclassified as being Mg-deficient and vice versa. Additionally, a large proportion of P-deficient leaves were misclassified as control leaves. This may have been because P-deficient leaves had large green, chlorotic, and necrotic spots that likely resulted in more variable spectral measurements. Furthermore, a large portion of the upper foliage of P-deficient plants was visually asymptomatic, leading these leaves to be classified with control plants.

Mature plants exhibited the lowest classification accuracy with an overall accuracy of 75%. Control plants had an 89% classification accuracy while N-deficient, P-deficient, K-deficient, Mg-deficient, and S-deficient plants had 100%, 52%, 42%, 92%, and 73%, respectively (Table 3). Potassium-deficient leaves were frequently misclassified as a control, Mg-deficient, or S-deficient leaf. Mature P-deficient leaves also exhibited low classification accuracy, with roughly one-third of all samples being classified as controls.

Table 4.3. Linear discriminant analysis classification accuracies for nutrient deficient flue-cured tobacco (*Nicotiana tabacum* L.) plants based on principal component analysis.

Deficiency treatment	Maturity stage		
	Young	Intermediate	Mature
Control	92%	94%	89%
Nitrogen (N)	100%	92%	100%
Phosphorus (P)	88%	58%	52%
Potassium (K)	—	70%	42%
Magnesium (Mg)	—	79%	92%
Sulfur (S)	90%	80%	73%
Overall accuracy	92%	82%	75%

Overall, PCA-based classification was highly accurate in distinguishing among the five macronutrient deficiencies induced in this study. Accuracy decreased with increasing maturity

likely due to the greater proportion of asymptomatic leaves on these plants. This proposed effect was especially impactful for the discrimination of P and K deficiencies. Nitrogen and S-deficient leaves were hypothesized to be similar enough to prevent accurate classification between these symptoms. However, in only three instances were S-deficient plants misclassified as N-deficient, and in no instance was a N-deficient plant misclassified as S-deficient. Phosphorus-deficient plants exhibited some of the lowest overall classification accuracies which may be attributed to the non-uniform appearance of the leaf surface. Similarly, mature K-deficient plants had poor classification accuracy possibly because a large portion of the upper leaves appeared completely asymptomatic, and those leaves remained in the analysis. Therefore, it may be inferred that N-, Mg-, and S-deficient plants have a greater proportion of leaves that are visibly and spectrally different from the leaves of control plants. Future work may find that dividing leaves by visual symptoms could yield helpful insights.

In conclusion, spectral discrimination of nutrient deficiencies appears to be a promising form of precision scouting that should be investigated further in field scenarios. With continual advancements in sensors and greater availability of technology, spectral remote sensing has the potential to become an indispensable tool for agronomic crop producers. The wavelengths identified here and in other studies should be used to develop simpler and less expensive sensors. Developing user-friendly software for automated spectral analysis should also be considered moving forward.

Acknowledgements

The authors would like to thank the North Carolina Tobacco Foundation for funding this research.

References

- Abdel-Rahman, E.M., F.B. Ahmed, and M. van den Berg. 2010. Estimation of sugarcane leaf nitrogen concentration using in situ spectrometry. *Int. J. Appl. Earth Observation Geoinformation* 12S:S52–S57.
- Adams, M.L., W.A. Norvell, W.D. Philpot, and J.H. Peverly. 2000a. Spectral detection of micronutrient deficiency in ‘Bragg’ soybean. *Agron. J.* 92:261–268.
- Adams, M.L., W.A. Norvell, W.D. Philpot, and J.H. Peverly. 2000b. Toward the discrimination of manganese, zinc, copper, and iron deficiency in ‘Bragg’ soybean using spectral detection methods. *Agron. J.* 92:268–274.
- Bajcsy, P., and P. Groves. 2004. Methodology for hyperspectral band selection. *Photogramm. Eng. Remote Sens.* 70:793–802.
- Bajwa, S., P. Bajcsy, P. Groves, and L. Tian. 2004. Hyperspectral image data mining for band selection in agricultural applications. *Trans. ASAE* 47:895–907.
- Behmann, J., J. Streinrücken, and L. Plümer. 2014. Detection of early plant stress responses in hyperspectral images. *ISPRS J. Photogramm. Remote Sens.* 93:98–111.
- Constantine, W., T. Hesterberg, K. Wittkowski, T. Song, and S. Kaluzny. 2016. *splus2R: Supplemental S-PLUS functionality in R*. R Package Documentation. p. 36.
- Daughtry, C.S.T., C.L. Walthall, M.S. Kim, E. Brown de Colstoun, and J.E. McMurtrey III. 2000. Estimating corn leaf chlorophyll concentration from leaf and canopy reflectance. *Remote Sens. Environ.* 74:229–239.
- Henry, J.B., M. Vann, I. McCall, P. Cockson, and B.E. Whipker. 2018a. Nutrient disorders of burley and flue-cured tobacco part 1: Macronutrient deficiencies. *Crop, Forage and Turfgrass Mgt.* 4:170076. doi:10.2134/cftm2017.11.0076.

- Henry, J.B., M. Vann, I. McCall, P. Cockson, and B.E. Whipker. 2018b. Nutrient disorders of burley and flue-cured tobacco part 2: Micronutrient disorders. *Crop, Forage and Turfgrass Mgt.* 4:170077. doi:10.2134/cftm2017.11.0077.
- Hoagland, R.J., and D.I. Arnon. 1950. The water-culture method for growing plants without soil. *California Agr. Expt. Sta. Circ.* 347. Revised ed.
- Koul, A., C. Becchio, and A. Cavallo. 2018. PredPsych: A toolbox for predictive machine learning-based approach in experimental psychology research. *Behavior Res. Methods* 50:1657–1672.
- Li, L., B. Jákli, P. Lu, T. Ren, J. Ming, S. Liu, S. Wang, and J. Lu. 2018a. Assessing leaf nitrogen concentration of winter oilseed rape with canopy hyperspectral technique considering a non-uniform vertical nitrogen distribution. *Industrial Crops and Products* 116:1–14.
- Li, L., S. Wang, T. Ren, Q. Wei, J. Ming, J. Li, X. Li, R. Cong, and J. Lu. 2018b. Ability of models with effective wavelengths to monitor nitrogen and phosphorus status of winter oilseed rape leaves using in situ canopy spectroscopy. *Field Crops Res.* 215:173–186.
- Mitra, G. 2017. Essential plant nutrients and recent concepts about their uptake. In: N. Naeem et al., editors, *Essential Plant Nutrients: Uptake, Use Efficiency, and Management*. Springer, Cham, Switzerland. p. 3–36.
- Osborne, S., J.S. Schepers, D. Francis and M.R. Schlemmer. 2002. Detection of phosphorus and nitrogen deficiencies in corn using spectral radiance measurements. *Agron. J.* 94:1215–1221.
- R Core Team. 2019. R: A language and environment for statistical computing. R Foundation for Statistical Computing, Vienna, Austria. <https://www.R-project.org/>

- Romanski, P., L. Kotthoff, and M.L. Kotthoff. 2018. Package 'FSelector'. R Package Documentation. p. 18.
- Römheld, V. 2012. Diagnosis of deficiency and toxicity of nutrients. In: P. Marschner, editor, Marschner's Mineral Nutrition of Higher Plants. 2nd ed. Academic Press, London, UK. p. 299–312.
- Rustioni, L., D. Grossi, L. Brancadoro, and O. Failla. 2018. Iron, magnesium, nitrogen and potassium deficiency symptom discrimination by reflectance spectroscopy. *Sci. Hortic.* 241:152–159.
- Stevens, A., and L. Ramirez–Lopez. 2014. An introduction to the prospectr package. R Package Documentation. p. 22.
- Thenkabail, P.S., J.G. Lyon, and A. Huete. 2019. Advances in hyperspectral remote sensing of vegetation and agricultural crops. In: P.S. Thenkabail et al., editors, *Hyperspectral Remote Sensing of Vegetation Volume One: Fundamentals, Sensor Systems, Spectral Libraries, and Data Mining for Vegetation*. 2nd ed. CRC Press, Boca Raton, FL. p. 3–37.
- Xie, L., G. Li, L. Peng, Q. Chen, Y. Tan and M. Xiao. 2017. Band selection algorithm based on information entropy for hyperspectral image classification. *J. Appl. Remote Sens.* 11:026018.
- Yang, C., R. Sui, and W.S. Lee. 2016. Precision agriculture in large-scale mechanized farming. In: Q. Zhang, editor, *Precision Agriculture Technology for Crop Farming*. CRC Press, Boca Raton, FL. p. 177–212.
- Zhang, X., F. Liu, Y. He and X. Gong. 2013. Detecting macronutrients content and distribution in oilseed rape leaves based on hyperspectral imaging. *Biosystems Engineering* 115:56–65.

CHAPTER 5

UAV-Based Hyperspectral Remote Sensing for Distinguishing Nutrient Disorders in Flue-Cured Tobacco

(Written in the style of Agronomy Journal)

UAV-Based Hyperspectral Discrimination of Macronutrient Deficiencies in Flue-Cured Tobacco

Core Ideas:

- Hyperspectral data were used to distinguish among N, P, and K deficiencies.
- K-nearest-neighbor classification achieved 99.7% overall accuracy.
- Information entropy and spectral derivatives selected optimal bands.

Abstract

Remote sensing of spectral reflection enables detection and identification of multiple plant health stressors including nutrient deficiencies. Past studies considered P and K deficiencies, but few have used a comprehensive approach to distinguish among nutrient deficiencies using remote sensing. This study was conducted to provide baseline spectral differentiation of nutrient disorders in flue-cured tobacco for N, P, and K deficiencies. These three nutrient disorders were previously determined to be easily inducible and are known to exhibit unique symptomology in terms of pattern, location, and most importantly, coloration. Field studies conducted over three field sites and two growing seasons enabled us to acquire spectral reflectance data which was analyzed using various band selection and classification techniques. To distinguish among these three deficiencies, information entropy and first and second derivative techniques were used. Information entropy selected bands centered at 475, 607, 672, 773, 820, and 911 nm while first and second derivative spectra selected wavelengths at 520, 585, 712, and 925 nm and 491, 549, 681, 741, and 898 nm; respectively. K-nearest-neighbor classification resulted in 99.7% classification accuracy with all data aggregated among sites and years. This information can be

used to develop inexpensive sensors that decrease the file size and computational complexity typically associated with hyperspectral data and can help flue-cured tobacco growers to better scout their crops for macronutrient deficiencies.

Abbreviations: BRDF, bidirectional reflectance distribution function; FIA, flow injection analysis; GDAL, geospatial data abstraction library; ICP-MS, inductively coupled plasma mass spectrometry; PC, principal component; PCA, principal component analysis; PLSR, partial least-squares regression; UAV, unmanned aerial vehicle

Introduction

Scouting crops for plant health related issues is traditionally time consuming and labor intensive. Thus, extensive effort in recent years has focused on developing and improving sensor technologies to automate crop scouting (Abdel-Rahman et al., 2010; Pu, 2017; Yang et al., 2016). Spectral remote sensing is a promising method to find and diagnose symptoms from biotic and abiotic plant stressors, such as insects, pathogens, and environmental conditions (Liew et al., 2008; Thenkabail et al., 2019). Different stressors cause physiological changes in plant tissues which may be quantified and characterized by how these changes affect spectral reflectance (Abdel-Rahman et al., 2010; Behmann et al., 2014). It is important to consider that there are many variables that affect measurement quality including time of day, cloud conditions, background (i.e., soil, water, weeds, etc.) reflectance, and solar angle (Adams et al., 2000b). However, one of the most important factors is addressed in the Bidirectional Reflectance Distribution Function (BRDF) which considers the angle of the sun, the sensor, and the subject in relation to one another (Liu et al., 2017). The concept that there are no perfect surfaces that

will reflect the same quality and quantity of light in every direction is captured by BRDF. Therefore, the location of the sensor relative to the location of the crop canopy and the sun is a highly important consideration for remote sensing (Barnsley, 1984; Roy et al., 2016).

Spectral sensors can be handheld or mounted to trucks, tractor booms, aircraft, or satellites (Jensen, 2007; Thenkabail et al., 2019). Of particular interest is remote sensing with spectral sensors mounted to UAVs, commonly referred to as drones. Often small, inexpensive, and easy to use, UAVs provide a rapid method of scouting that can greatly reduce the intensive labor costs associated with traditional scouting (Abdullahi et al., 2015; Huang et al., 2010; Mahajan et al., 2017). Furthermore, UAVs are now highly accessible for farmers due to US federal regulations no longer requiring individuals to obtain a pilot's license for commercial purposes (Patel, 2016). Although UAVs and satellites both obtain data covering a large area in a relatively short time, UAVs have advantages such as higher sensor resolution and greater ability to obtain data without time restrictions. For instance, satellites are limited to imaging during overpasses dictated by their orbital configuration and therefore, images may be rendered inappropriate for analysis due to cloud cover and other atmospheric noise. However, many concepts of spectral remote sensing remain the same regardless of how the instrument is deployed.

Two primary types of spectral imaging are commonly used: multispectral and hyperspectral (Jensen, 2007). Multispectral imaging typically records the amount of red, green, blue, and infrared light reflected from a surface (Mobaraki and Amigo, 2018). Each measured region of light is commonly referred to as a spectral "band", which can be wide or narrow in terms of the measured wavelengths (Jensen, 2007). In contrast to multispectral images which have very broad bands, hyperspectral imaging is characterized by measuring reflectance from

numerous narrow bands in order to create a nearly continuous spectrum (Mobaraki and Amigo, 2018). The shape of this spectrum is known as a spectral signature and it can be used to identify a particular subject like a unique fingerprint (Mobaraki and Amigo, 2018). Hyperspectral imaging has existed for almost 50 years (Amigo et al., 2015), but has had limited use due to expense and analysis difficulty.

Spectral imaging sensors utilize a combination of spectroscopy, radiometry, and conventional imaging methods to record one dimension of spectral data to be stored in two spatial dimensions in the form of pixels (Ferrari et al., 2013; Ortenberg, 2019). These one spectral and two spatial dimensions are put together to create a three-dimensional array of data, often referred to as a hypercube. It may be thought of as numerous images of the same area stacked atop each other, where each layer stores reflectance from a single band (Amigo et al., 2015; Ferrari et al., 2013). Each pixel within a hyperspectral image contains the average reflectance value for all objects within the pixel boundaries plus noise (Amigo et al., 2015).

Numerous methods are commonly used to analyze hyperspectral data. One of the primary goals of hyperspectral analysis is to determine which spectral bands are most correlated with the variability observed within the image. Information entropy is a measurement for how much variability is contained within a band and it is commonly used for hyperspectral band selection (Bajcsy and Groves, 2004; Bajwa et al., 2004; Xie et al., 2017). Derivative measures are also useful for band selection by identifying areas with rapid changes in direction or pattern within spectra (Bajcsy and Groves, 2004). Discriminant analysis is a classification method that involves modeling based on multiple variables (James et al., 2013a; Thenkabail et al., 2019). The analysis attempts to determine which explanatory variables or features are optimal for separating among two or more unique classes by creating a line to best separate observations by class in a multi-

dimensional space (Bajwa et al., 2019). K-nearest-neighbor classification works by classifying a test observation based on its proximity to neighboring training samples (James et al., 2013a). Pasolli et al., 2019). Random forests are a decision tree-based classification algorithm that utilize many individual decision trees (James et al., 2013b).

Differences observed in spectral reflectance can serve as non-invasive indicators of various plant stressors (Adams et al., 2000a). There are reflectance patterns that differ based on three major factors: 1) the plant species, 2) the stage of development, and 3) the plant stressor. It is essential that sensors function properly for multiple species, maturity levels, and stress responses and therefore, research must be conducted on a crop-by-crop basis. Plant pigments play an essential role in spectral detection of plant stress. Many plant stressors result in chlorophyll degradation, leading to symptoms of foliar chlorosis or yellowing (Liew et al., 2008). This makes chlorophyll estimation a good indicator of many plant stressors (Liew et al., 2008). Chlorophyll, which reflects highly in the green spectrum tends to degrade faster than yellow pigments such as carotenoids (Liew et al., 2008; Zhou et al., 2019). Thus, understanding the basis of various symptoms is certainly useful for remote sensing applications in plant health monitoring.

Plant nutrition is an area of study that can benefit significantly from spectral monitoring as demonstrated by numerous studies (Abdel-Rahman et al., 2010; Inoue et al., 2012; Li et al., 2018a, 2018b; Mahajan et al., 2017; Rustioni et al., 2018; Thorp et al., 2017; Zhang et al., 2013). Each of the essential nutrients perform crucial roles in plant development and deficiencies of each nutrient cause unique symptoms that are visually diagnosable in many instances. Nutrient deficiencies often cause changes in foliar coloration which may appear yellow (chlorotic), white (bleached), brown (necrotic), red, or black (Römheld, 2012). For instance, N deficiency is often

associated with chlorosis of the lower foliage due to chlorophyll degradation (Henry et al., 2018; Römheld, 2012). Phosphorus deficiency is associated with reddening due to enhanced anthocyanin or betacyanin synthesis and accumulation (Henry et al., 2019). Necrosis, or the death of plant tissue, often occurs when nutrient deficiencies or toxicities become severe (Römheld, 2012). Characterizing the spectral reflectance may enable sensor-based diagnostics of plant nutrient disorders. However, it is essential to consider that different species exhibit different spectral characteristics, and thus, species-specific research may be required to successfully utilize spectral remote sensing methods.

Nitrogen is typically considered the primary nutrient of interest due to the relatively high concentrations required by plants and because most common N forms are readily leached and volatilized from the root zone (Mitra, 2017; Stroppiana et al., 2019). In fact, it is estimated that only half of the N applied agronomically is used by the crop while the rest is lost to the environment, primarily through denitrification or leaching (Hawkesford et al., 2012; Sylvester-Bradley and Kindred, 2009). Much of the N is lost in the form of nitrate which can accumulate and pollute groundwater (Inoue et al., 2012). As a result, N deficiency is one of the most commonly observed nutrient disorders in crops. Therefore, rapid, automated, and accurate N deficiency identification using sensors has become a topic of significant interest (Thorp et al., 2017).

Although N status and deficiencies are most commonly observed and studied, other plant nutrients are also important to monitor. The essential macronutrients are needed in relatively high concentrations and include N, P, K, Ca, Mg, and S (Mitra, 2017). Each of the essential nutrients perform crucial roles in plant development and deficiencies of each nutrient cause unique symptoms that are visually diagnosable in many instances. Phosphorus nutrition is of

particular interest due to historically excessive concentrations applied to fields and contaminating ground and surface water. Such overfertilization has led to eutrophication of waterways with detrimental effects on organisms and the environment (Liu et al., 2015; Majsztrik and Lea-Cox, 2013). Even so, P deficiency may be observed in commercial production settings, necessitating advanced methods of rapid deficiency identification techniques. This demonstrates how accurate nutrient monitoring is essential for agricultural production moving forward.

The purpose of this study was to characterize the spectral properties of N, P, and K deficiency symptoms in flue-cured tobacco, and to determine if these symptoms could be distinguished from among one another using spectral reflectance data. This goal was achieved by inducing N, P, and K deficiencies in field conditions and acquiring UAV-based measurements throughout two growing seasons.

Materials and Methods

Plant Material and Experimental Design

Field experiments were conducted during the 2018 growing season in Wilson, NC (35°47'43" N lat, 77°57'01" W long) and during the 2019 growing season in Wilson (35°47'42" N lat, 77°56'52" W long) and Princeton, NC (35°27'20" N lat, 78°11'18" W long). The research sites were located on farms that were planted and maintained by the farm managers. Soil samples were collected prior to fertilization at each research site and tests were conducted by the North Carolina Department of Agriculture and Consumer Services (NCDA&CS; Raleigh, NC). Soils were primarily sand with average pH between 5.68 and 6.05 (Table 5.1). At each location, NC 196 tobacco seeds (GoldLeaf Seed Co.) were sown into 288-cell (2.2 × 2.2 cm) polystyrene trays

(Carolina Greenhouses, Kinston, NC) and germinated in a float system. In Wilson, the float system utilized a 20-10-20 fertilizer (Yara, Oslo, Norway) at a constant concentration of 125 mg L⁻¹ N.

Table 5.1. Average soil properties exhibited at each field site.

Soil properties	Wilson, NC		Princeton, NC
	2018	2019	2019
Soil series	Norfolk	Goldsboro / Marlboro	Goldsboro
Surface texture	loamy sand	sandy loam	sandy loam
Soil pH	5.70	5.68	6.05
CEC (cmol _c kg ⁻¹)	2.97	3.12	5.73
Humic matter (%)	0.20	0.32	0.48

There were 36 plots at each field site and the plots each received a specific rate of fertilizer. In 2018, a 6-6-18 fertilizer (Tobacco Super Rainbow; Agrium U.S., Inc., Denver, CO) was applied to 18 whole plots at a rate of 78.5 kg N ha⁻¹ on 4 May as a side-dress application. This rate was selected based on typical flue-cured tobacco production recommendations published by Fisher (2018). The remaining 18 whole plots were not fertilized with the 6-6-18 fertilizer, but instead received one strip treatment of N-, P-, or K-deficient fertilizer to induce N, P, or K deficiency, respectively. Each strip received a custom fertilizer made to replicate the 6-6-18 fertilizer without either N, P, or K (Table 2). In 2019, a similar approach was used but with the addition of two whole plot fertilization rates representing 50% and 200% of the standard rate recommended by Fisher (2018). Nine whole plots each received a fertilization treatment of 0,

39.25, 78.50, or 157.0 kg N ha⁻² from the commercial 6-6-18 fertilizer. Within each 0 and 39.25 kg N ha⁻² plot, three strips of 12 plants each were fertilized with the N-, P-, and K-deficient fertilizer, respectively (Table 5.2).

Table 5.2. Composition of custom deficiency inducing fertilizers created to replicate commercial 6-6-18 tobacco fertilizer devoid of either N, P, or K.

Fertilizer composition	N-P ₂ O ₅ -K ₂ O	Fertilizer applied (kg ha ⁻¹)		
		-N	-P	-K
NaNO ₃	16-0-0	-	277.2	490.0
KNO ₃ / K ₂ SO ₄ / KCl	12-0-46	-	283.8	-
CaH ₄ P ₂ O ₈ / CaHPO ₄	0-45-0	174.3	-	174.3
K ₂ SO ₄	0-0-52	251.2	-	-
2MgSO ₄ ·K ₂ SO ₄	0-0-22	475.4	475.4	-
CaSO ₄ ·2H ₂ O	0-0-0	-	145.0	348.3
MgSO ₄ ·7H ₂ O	0-0-0	-	-	523.0
Micronutrient Mix	0-0-0	48.9	48.9	48.9

Spectroscopic Measurements

A handheld spectrometer (PSM-2500; Spectral Evolution, Lawrence, MA) was used to collect spectral reflectance data throughout the study. The sensor had a spectral range of 300 to 2,500 nm and a spectral resolution of 3.5 nm at 700 nm, 22 nm at 1,500 nm, and 22 nm at 2,100 nm with the percent reflectance output in 1 nm increments. The sensor was equipped with a fiberoptic leaf clip capable of taking leaf-level measurements. This leaf clip had a self-contained

light source with two light settings, of which, the higher setting was used. Measurements were recorded at the final data collection in 2018 and at every data collection in 2019. At each data collection, one representative leaf was selected per strip and per subplot treatment for spectral analysis. Measurements using the leaf clip were taken approximately 2 to 3 cm from the leaf margin and one-third of the leaf length away from the leaf tip. This location was selected because it typically represented the average degree of symptoms for each leaf. Areas of necrosis were avoided as necrotic tissues reflected much different patterns than non-necrotic tissues, regardless of symptomology. The selected leaves were subsequently removed from the plant for foliar nutrient analysis.

Hyperspectral images were recorded during the field study from a UAV-based hyperspectral sensor. Hyperspectral data were collected using a UAV-mounted pushbroom scanner (Headwall Nano VNIR; Headwall Photonics, Inc., Boston, MA) attached to an UAV (DJI Matrice 600 Pro; SZ DJI Technology Co., Ltd., Shenzhen, Guangdong, China) flying at an altitude of 60 m. The sensor had a spatial resolution of 640×512 pixels, resulting in a pixel size of 1.5 cm. The spectral resolution ranged from 400–1,000 nm with 270 total bands. In 2018, data were collected by PrecisionHawk (Raleigh, NC) on 18 June, 2 July, 16 July, and 14 August. In 2019, data were obtained using the same sensor 6 June, 19 June, 3 July, 17 July, and 9 Aug.

Nutrient Analysis

Foliar tissue samples were collected in each experiment to quantify nutrient concentrations and ensure symptoms were due to the applied treatment. Leaf tissues were dried at 70 °C for 72 hr and then ground in a sample mill (Thomas Wiley® Mini-Mill; Thomas Scientific, Swedesboro, NJ), and analyzed for nutrient concentrations (AgSource Laboratories,

Lincoln, NE). Total N was processed by Kjeldahl digestion and determined via flow injection analysis (FIA). Extractable K was processed by 2% acetic acid digestion and determined via inductively coupled plasma mass spectrometry (ICP-MS). Total P and all other plant minerals were processed by nitric acid/hydrogen peroxide digestion, and determined via ICP-MS.

Data Preprocessing

Radiometric reflectance data were manipulated and analyzed using R statistical software (version 3.6.0, R Core Team, 2019). Measurements from each leaf of each treatment were assigned into several subgroups depending on various characteristics. Leaves received an objective symptom severity rating of four possible categories: 1) none, 2) low, 3) intermediate, or 4) high (Fig. 1). Furthermore, measurement stages were separated by plant maturity: 1) young, 2) intermediate, or 3) mature. Young plants were those that had 6 or fewer leaves, intermediate plants had 7 to 12 leaves, and mature plants had more than 12 leaves. Fully mature tobacco plants developed between 18 and 20 expanded leaves prior to anthesis. Reflectance data collected by the handheld spectroradiometer were visually inspected to ensure any errors or inaccurate measures were removed (e.g., improper placement of the leaf clip). Measurements were then assigned to several classes to define plant maturity (young, intermediate, or mature), leaf location (numerically from bottom to top), and symptom severity (low, intermediate, or high). Additionally, reflectance from bands between 1350 and 1450 nm and 1800 and 1950 nm were removed from further analysis due to high water absorptance within these ranges (Abdel-Rahman et al., 2010; Kumar et al., 2002; Liew et al., 2008).

Hyperspectral image tiles were orthorectified in QGIS (version 3.8 “Zanzibar”, QGIS Development Team) and merged into single raster files using the Geospatial Data Abstraction

Library (GDAL; GDAL/OGR contributors, Open Source Geospatial Foundation) in Python (version 3.7.4; Python Software Foundation). Rasters were aligned in QGIS and files were converted to ENVI format using GDAL. Soils and other background noise were removed by creating a mask to retain only pixels containing vegetation. A polygon layer was created to encompass each part of the field with its corresponding treatments, and this was used to calculate average spectra from each treatment. Average treatment values were then used for further analyses instead of using individual pixel values. This was done to reduce computational complexity.

Band Selection

Spectra were used to calculate information entropy as well as first and second spectral derivatives to identify which wavelengths contribute most to the variability observed among the nutrient-deficient leaves. Information entropy was calculated using the FSelector package (Romanski and Kotthoff, 2018) while derivatives were calculated using the prospectr package (Stevens and Ramirez-Lopez, 2014) in R. Savitzky-Golay filtering was applied with a window size of 10 bands to information entropy data to reduce noise and smooth the data. Derivatives were calculated and smoothed using the gap-segment algorithm with a filter length of 11 bands for both first and second order derivatives. Due to the nature of narrow bands, high correlation is often observed among neighboring bands (Thenkabail et al., 2019). This correlation, referred to as multicollinearity, leads to high levels of redundancy, meaning many bands will convey similar information regarding observed variability. Hence, peaks and valleys were calculated using the splus2R package (Constantine et al., 2016) to determine the greatest individual absolute values or ranges of values within a span of 10 bands. Ranges of continuous values with uniform

importance were aggregated and used to determine the central wavelength representing that range. The identified wavelengths represented those with the greatest impact on observed variability.

Symptom Classification

Reflectance spectra captured using the spectroradiometer were analyzed by growth stage using principal component analysis (PCA), with 10 principal components (PCs) selected for each growth stage. Linear discriminant analysis was used to develop classification models to distinguish among the various symptoms. The classification models were subjected to a custom-built five-fold cross validation function where 80% of the data was used for model training and the remaining 20% was used to test the models (James et al., 2013a). Following the first validation, a second validation was conducted with a new set of testing data previously used to train the model. This process was repeated to optimize the model until all data were used for both training and testing functions. The final classification results were put into a confusion matrix for each growth stage and analyzed using the PredPsych package (Koul et al., 2018) in R. The matrices were used to determine the overall accuracy and misclassification rates for each model.

Hyperspectral image classification was conducted using R. Principal components analysis was used for dimensionality reduction with 10 PCs being selected per data set. The selected PCs were used to train various classification models. Several classification methods and algorithms were tested including linear discriminant analysis, quadratic discriminant analysis, K-nearest neighbors, and random forest. Leave-one-out cross validation was used to test the classification models for each location and data collection separately and with all data aggregated together. Principal components analysis was used for dimensionality reduction with 10 PCs being selected

per data set. Classification results were put into a confusion matrix and analyzed to determine the overall accuracy and misclassification rates for each model.

Results and Discussion

Symptomology

The visible deficiency symptoms observed were more severe in Wilson than in Princeton. This was likely due to Princeton having soils with higher CEC and humic matter, which were better able to provide residual nutrients than the soils found in Wilson. Nitrogen-deficient strips typically exhibited the most severe symptoms. In most instances, N-deficient plants were visually indistinguishable from control plants that received no fertilizer. These plants were highly chlorotic throughout the experiment with only the youngest leaves maintaining any green pigmentation. These symptoms were in agreement with those described by Henry et al. (2018) who induced N deficiency symptoms in greenhouse-grown flue-cured tobacco.

Phosphorus-deficient strips appeared asymptomatic and were typically indistinguishable from control plants fertilized with 78.50 kg N ha⁻² from the commercial 6-6-18 fertilizer. The symptoms of non-uniform chlorosis with olive-green leaf spots and large necrotic lesions described by Henry et al. (2018) were not present in this study. However, the lack of P deficiency symptoms was likely attributable to the high P concentrations reported in the soil tests. Soil P concentrations were consistently reported to be two- to five-fold greater than optimum according to the reported P-index values (data not shown).

Potassium-deficient strips initially appeared healthy but later developed characteristic K deficiency symptoms on the lower to central leaves. These symptoms appeared as a marginal chlorosis and necrosis, similar to the symptoms reported by Henry et al. (2018). Symptoms

developed at both sites and during both years approximately 4 to 6 wk after application of the K-deficient fertilizer.

The symptoms observed in this study stress the importance of obtaining soil tests to use in conjunction with traditional or modern scouting methods. A tobacco grower with access to such soil tests would have an initial indication of which nutrients may be deficient simply based on soil nutrient availability. Although it is important to scout for nutrient disorders, it is also important to obtain preliminary ground truth data to inform decisions and investigation into the possible causes of observed symptoms.

Foliar nutrients

Foliar nutrient concentrations varied significantly by deficiency treatment. Plants grown without any fertilizer or with just the N-deficient fertilizer had the lowest foliar N concentrations, averaging 2.27% and 2.15%, respectively. In contrast, control plants grown with 78.5 kg ha⁻¹ N had average foliar N concentrations of 3.45%, while those grown with 157 kg ha⁻¹ N had foliar N concentrations of 3.93%. Flue-cured tobacco grown in a greenhouse using a complete Hoagland solution had foliar N concentrations of 4.76% while those grown with a N-deficient solution contained 1.16% N (Henry et al., 2018). This concentration of 1.16% was considered a critical nutrient concentration because it was the average concentration observed in plants that had just developed visible symptoms. Although N-deficient plants in our study had higher foliar N concentrations than those reported by Henry et al. (2018), the concentrations were still low enough to induce visible symptomology. This indicates that field-grown tobacco plants may exhibit a different critical N concentration than greenhouse-grown plants.

Any differences in foliar P concentrations were statistically insignificant, with P concentrations ranging from 0.26% to 0.31% (Table 5.3). Again, this was likely due to the fact that the soils used in these experiments already contained P concentrations in excess of what is typically required by flue-cured tobacco. The critical P concentration reported by Henry et al. (2018) was 0.07%, lower than what was observed in our study. This may help to explain why visible symptoms were not observed. In contrast, foliar P concentrations reported for greenhouse-grown flue-cured tobacco supplied with a complete Hoagland solution were 0.47% (Henry et al., 2018), higher than the highest foliar P concentrations observed in this study.

Trends in foliar K concentrations were closer to what was observed for N than for P. Average foliar K concentrations ranged 3.00% to 4.71%. Control plants grown with 157 kg ha⁻¹ N using a 6-6-18 fertilizer had higher foliar K concentrations than plants grown without fertilizer or with only the K-deficient fertilizer. These plants exhibited foliar K concentrations of 3.00% and 3.37%, respectively. The critical K concentration reported by Henry et al. (2018) for greenhouse-grown flue-cured tobacco was 0.76%, much lower than what was observed in our study. Furthermore, the K concentration found in nutrient-sufficient plants was 7.71% (Henry et al., 2018), much higher than what was observed in this study. This further supports the hypothesis that tobacco grown in a controlled environment may exhibit different nutrient requirements and critical nutrient concentrations than field-grown plants.

Table 5.3. Flue-cured tobacco (*Nicotiana tabacum* L.) foliar nutrient concentrations observed in the 2018 and 2019 field experiments. The base fertilizer rate of 6-6-18 was used as a control to compare with the N-deficient (-N), P-deficient (-P), and K-deficient (-K) strip treatments.

Fertilizer rate	Foliar nutrient concentration (%)		
Deficiency treatment	N	P	K
0 kg ha ⁻¹ N	2.27e †	0.29a	3.00e
-N	2.15e	0.26a	3.49de
-P	3.51bc	0.26a	4.26ab
-K	3.48c	0.29a	3.39de
37.25 kg ha ⁻¹ N	3.05d	0.29a	3.68cd
-N	3.03d	0.29a	4.01bc
-P	3.82ab	0.27a	4.35ab
-K	3.91a	0.30a	4.08bc
78.5 kg ha ⁻¹ N	3.45c	0.30a	4.37ab
157 kg ha ⁻¹ N	3.93a	0.31a	4.71a

† Different letters within columns indicate statistically significant differences between samples means based on Tukey's honestly significant differences.

Band Selection

Information entropy exhibited peaks at 475, 607, 672, 773, 820, and 911 nm with all data aggregated (Figure 5.1). These peaks demonstrate which wavelengths account for the most variation observed among the treatments. In contrast, the lowest information entropy was observed at 540 and 706 nm, demonstrating that these wavelengths contribute little to the

observed variability in these images. First derivative spectra demonstrated significant peaks and valleys at 520, 585, 712, and 925 nm (Figure 5.2). Second derivative spectra demonstrated significant peaks and valleys at 491, 549, 681, 741, and 898 nm (Figure 5.2). These wavelengths also illustrate regions of the spectrum contributing highly to the observed variability.

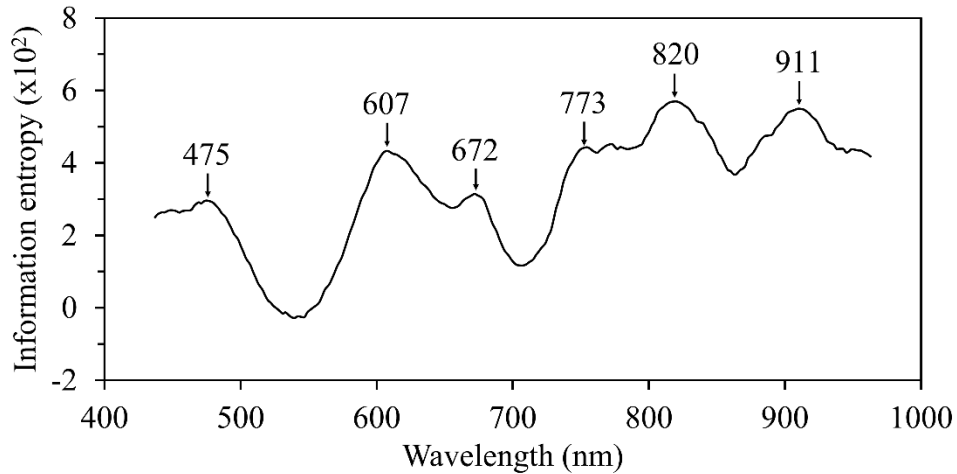


Figure 5.1. Savitzky-Golay filtered information entropy observed among flue-cured tobacco (*Nicotiana tabacum* L.) plants grown under N-, P-, and K-deficient conditions. Peak wavelengths demonstrate locations with the most informative bands necessary to distinguish among these deficiencies and asymptomatic plants.

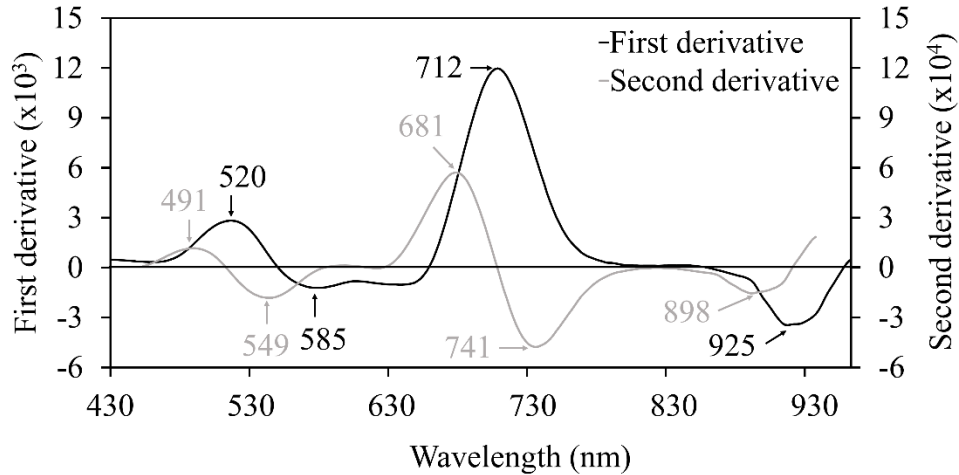


Figure 5.2. First and second derivatives for aggregated flue-cured tobacco (*Nicotiana tabacum* L.) plant data smoothed using the gap-segment algorithm. Peak wavelengths demonstrate locations with the most informative bands necessary to distinguish among N, P, and K deficiencies.

Li et al. (2018a) studied hyperspectral reflectance for estimating N in upper, middle, and lower oilseed rape (*Brassica napus* L.) plants. They used partial least-squares regression (PLSR) and reported optimal wavelengths of 437, 565, 667, 724, 993, 1084, and 1189 nm for upper leaves, 423, 570, 598, 659, 725, and 877 nm for middle leaves, and 420, 573, 597, 667, and 718 nm for lower leaves (Li et al., 2018a). Li et al. (2018b) also used PLSR to model and predict foliar N and P concentrations in oilseed rape. They compared PLSR with other data transformations such as first derivatives and continuum removal and found methods involving first derivatives were most effective. Optimal wavelengths selected for N were 445, 556, 657, 764, 985, 1082, and 1994 nm while those selected for P included 755, 832, 891, 999, 1196, and 1267 nm (Li et al., 2018b). Zhang et al. (2013) investigated the spectral response of oilseed rape to N, P, and K deficiencies using PLSR. They reported optimal wavelengths of 440, 473, 513,

542, 659, 718, 744, 865, 928, 965, 986, and 1015 nm for N, 468, 522, 698, 721, 817, 967, 979, and 1025 nm for P, and 456, 554, 667, 720, and 1027 nm for K (Zhang et al., 2013). These studies selected wavelengths that were often in similar regions to those selected in our study.

Band selection is essential for identifying the most important wavelengths from hyperspectral reflectance data. Each band can be considered another dimension to the data, and the high dimensionality exhibited by hyperspectral data limit the statistical power (Bajwa et al., 2019). With increasing dimensionality comes an exponential increase in the amount of data required to derive statistically significant results (Bajwa et al., 2019; Thenkabail et al., 2019). Dimensionality reduction attempts to eliminate redundancy while maintaining data that explain a high degree of the variability (Thenkabail et al., 2019). Furthermore, reducing the number of bands enables the development of less expensive sensors that only measure the most important wavelengths. This also has the potential to decrease computational power and can simplify analysis and interpretation of results.

Symptom Classification

K-nearest-neighbor classification with leave-one-out cross validation resulted in the highest classification accuracy. Overall classification accuracy was 99.7% with all data aggregated (Figure 5.3); however, accuracy varied significantly within each image. The first flight in 2018 in Wilson had an overall accuracy of 81.5%, correctly classifying all control plants. In contrast, N-, P-, and K-deficient plants had just 33.3%, 50.0%, and 50.0% classification accuracies, respectively. The second flight had 95.0% overall accuracy with 66.7%, 83.3%, and 100% accuracy for N-, P-, and K-deficient plants, respectively. The third flight had 88.9% overall accuracy with 66.7%, 50.0%, and 100% classification accuracies for N-, P-, and

K-deficient plants, respectively. Finally, the fourth flight exhibited 81.4% overall accuracy with N-, P-, and K-deficient plants exhibiting 66.7%, 66.7%, and 16.7% accuracies, respectively. In 2019, the Wilson site exhibited overall accuracies of 90.4%, 90.4%, 87.4%, 93.4%, and 84.5% for the first through fifth flights, respectively. In Princeton, overall accuracies were 87.3%, 86.3%, and 91.4% for the third, fourth, and fifth flights, respectively.

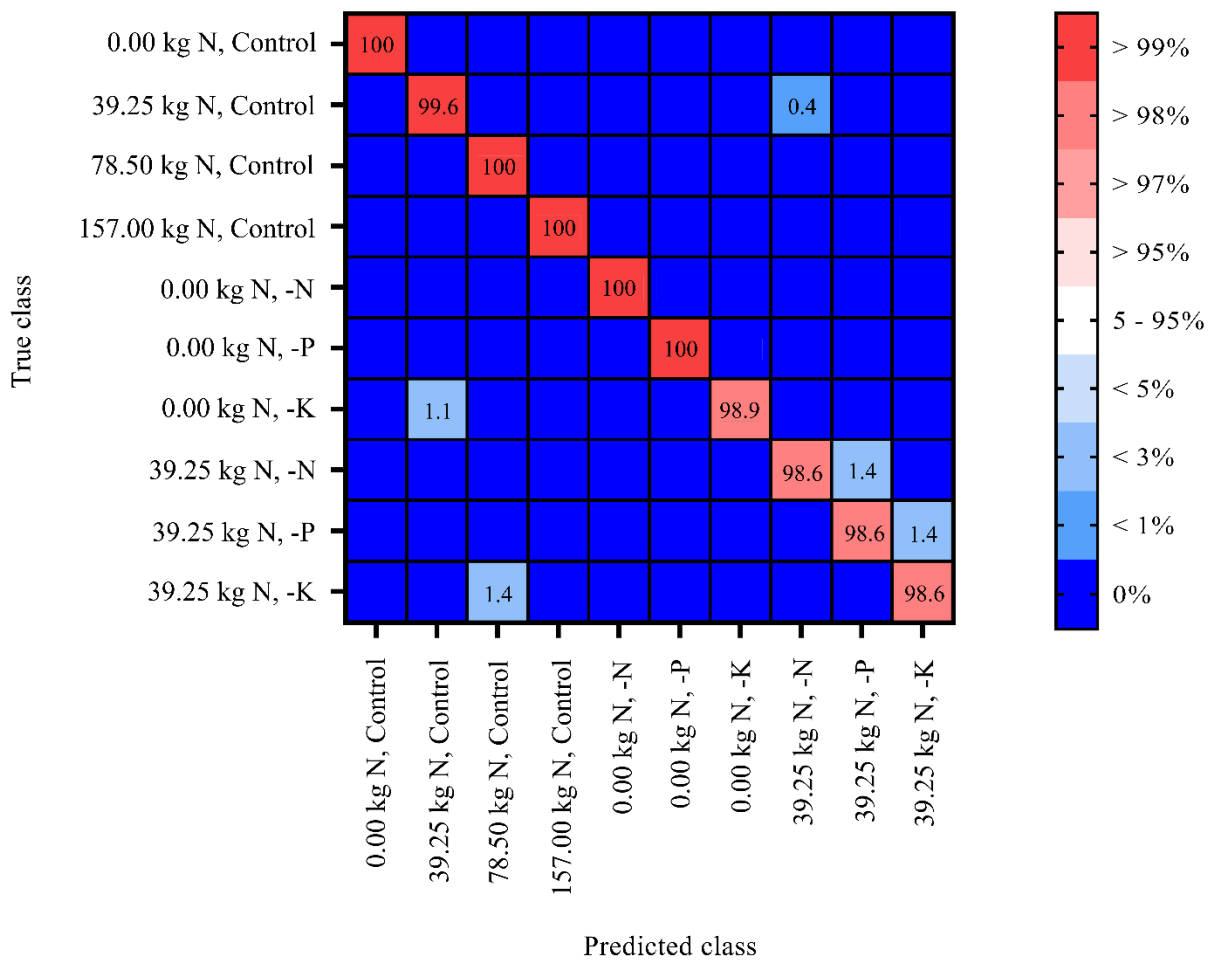


Figure 5.3. Heat map demonstrating classification accuracies achieved among aggregated data from all fertilizer treatment combinations used in the 2018 and 2019 field studies. Red cells along the diagonal represent the percentage of correctly classified subjects within a row while the blue cells represent the percentage of misclassified subjects within a row.

A study by Rustioni et al. (2018) reported successful discrimination among N, K, Mg, and Fe deficiencies in grape (*Vitis vinifera* L.) leaves using hyperspectral reflectance measurements. They used leaves of several maturity levels and recorded reflectance from different areas on the leaf surface (i.e., near veins, between veins, and near margins).

Symptomatic leaf reflectance data were transformed and normalized before being subtracted from control spectra (Rustioni et al., 2018). Each of the four nutrient deficiencies resulted in symptoms of chlorosis that were distinguishable based on the reflectance values associated with various pigments. For instance, the presence of chlorophylls *a* and *b*, carotenoids, and anthocyanins could be distinguished using bands near 678, 650, 495, and 550 nm (Rustioni et al., 2018). Similarly, varying symptoms of chlorosis were observed in our study but were found to be highly distinguishable when using the entire data set.

In this study, we successfully induced N and K deficiencies in two fields in NC. Although visible P deficiency symptoms did not develop, band selection and classification analysis techniques were successful in distinguishing among these deficiencies. The implications of the selected wavelengths that captured the most differences in symptoms demonstrate that inexpensive sensors can be developed with specific bands to decrease the size and computational complexity associated with hyperspectral data. Development of such sensors will help farmers, extension agents, and commercial crop health diagnosticians to quickly and accurately scout flue-cured tobacco fields for N, P, and K, deficiencies. This will ultimately help to save time, decrease fertilizer waste, and increase plant uniformity and quality.

Acknowledgements

We would like to thank the North Carolina Tobacco Foundation for funding this research. Further thanks to Vick Family Farms of Wilson, NC and Kornegay Farms of Princeton, NC for donating the field space, planting, and maintaining the research site. Thanks to Norman Harrell and Bryant Spivey for their help working with the farms. Thanks to our technicians Jeremy Machacek, Ingram McCall, and Scott Whitley for managing research preparation. Lastly, thank you to the graduate and undergraduate students for their contributions applying treatments, collecting data, and more; Jeb Bullard, Drew Clapp, Camden Finch, Paige Herring, Nathan Jahnke, Nick Manning, Channie Renn, Maggie Short, Drake Stevens, and Patrick Veazie.

Literature Cited

- Abdel-Rahman, E.M., F.B. Ahmed, and M. van den Berg. 2010. Estimation of sugarcane leaf nitrogen concentration using in situ spectrometry. *Int. J. Appl. Earth Observation Geoinformation* 12S:S52–S57.
- Abdullahi, H.S., F. Mahieddine, and R.E. Sheriff. 2015. Technology impact on agricultural productivity: A review of precision agriculture using unmanned aerial vehicles. In: P. Pillai, Y.F. Hu, I. Otung, and G. Giambene, editors, *Wireless and Satellite Systems*, 7th International Conference, WiSATS 2015, Bradford, UK, July 6–7, 2015, Revised Selected Papers. Springer, Cham, Switzerland. p. 388–400.
- Adams, M.L., W.A. Norvell, W.D. Philpot, and J.H. Peverly. 2000a. Spectral detection of micronutrient deficiency in ‘Bragg’ soybean. *Agron. J.* 92:261–268.
- Adams, M.L., W.A. Norvell, W.D. Philpot, and J.H. Peverly. 2000b. Toward the discrimination of manganese, zinc, copper, and iron deficiency in ‘Bragg’ soybean using spectral detection methods. *Agron. J.* 92:268–274.
- Amigo, J.M., H. Babamoradi, and S. Elcoroaristizabal. 2015. Hyperspectral image analysis. A tutorial. *Anal. Chim. Acta* 896:35–51.
- Bajcsy, P., and P. Groves. 2004. Methodology for hyperspectral band selection. *Photogramm. Eng. Remote Sens.* 70:793–802.
- Bajwa, S., P. Bajcsy, P. Groves, and L. Tian. 2004. Hyperspectral image data mining for band selection in agricultural applications. *Trans. ASAE* 47:895–907.
- Bajwa, S.G., Y. Zhang, and A. Shirzadifar. 2019. Hyperspectral image data mining. In: P.S. Thenkabail et al., editors, *Hyperspectral Remote Sensing of Vegetation Volume One:*

- Fundamentals, Sensor Systems, Spectral Libraries, and Data Mining for Vegetation. 2nd ed. CRC Press, Boca Raton, FL. p. 273–302.
- Barnsley, M.J. 1984. Effects of off-nadir view angles on the detected spectral response of vegetation canopies. *Int. J. Remote Sens.* 5:715–728.
- Behmann, J., J. Streinrücken, and L. Plümer. 2014. Detection of early plant stress responses in hyperspectral images. *ISPRS J. Photogramm. Remote Sens.* 93:98–111.
- Constantine, W., T. Hesterberg, K. Wittkowski, T. Song, and S. Kaluzny. 2016. splus2R: Supplemental S-PLUS functionality in R. R Package Documentation. p. 36.
- Ferrari, C., G. Foca, and A. Ulrici. 2013. Handling large datasets of hyperspectral images: Reducing data size without loss of useful information. *Anal. Chim. Acta* 802:29–39.
- Fisher, L.R. 2018. North Carolina State University: Flue-cured tobacco guide 2018 AG-187. Rev. ed. North Carolina Coop. Ext., Raleigh.
- Hawkesford, M., W. Horst, T. Kichey, H. Lambers, J. Schjoerring, I.S. Møller, and P. White. 2012. Functions of macronutrients. In: P. Marschner, editor, *Marschner's Mineral Nutrition of Higher Plants*. 2nd ed. Academic Press, London, UK. p. 135–189.
- Henry, J., P. Perkins-Veazie, I. McCall, and B. Whipker. 2019. Restricted phosphorus fertilization increases the betacyanin concentration and red foliage coloration of alternanthera. *J. Amer. Soc. Hortic. Sci.* 144:264–273.
- Henry, J.B., M. Vann, I. McCall, P. Cockson, and B.E. Whipker. 2018. Nutrient disorders of burley and flue-cured tobacco part 1: Macronutrient deficiencies. *Crop Forage Turfgrass Mgt.* 4:170076.

- Huang, Y., S.J. Thomson, Y. Lan, and S.J. Maas. 2010. Multispectral imaging systems for airborne remote sensing to support agricultural production management. *Int. J. Agric. Biol. Eng.* 3:50–62.
- Inoue Y., E. Sakaiya, Y. Zhu, and W. Takahashi. 2012. Diagnostic mapping of canopy nitrogen content in rice based on hyperspectral measurements. *Remote Sens. Environ.* 126:210–221.
- James, G., D. Witten, T. Hastie, and R. Tibshirani. 2013a. Classification. In: G. Casella, S. Fienberg, and I. Olkin, editors, *An Introduction to Statistical Learning with Applications* in R. Springer, New York, NY. p. 127–174.
- James, G., D. Witten, T. Hastie, and R. Tibshirani. 2013b. Tree-based methods. In: G. Casella, S. Fienberg, and I. Olkin, editors, *An Introduction to Statistical Learning with Applications* in R. Springer, New York, NY. p. 303–335.
- Jensen, J.R. 2007. *Remote sensing of the environment: An earth resource perspective*. 2nd ed. Pearson Prentice Hall, Upper Saddle River, NJ.
- Koul, A., C. Becchio, and A. Cavallo. 2018. PredPsych: A toolbox for predictive machine learning-based approach in experimental psychology research. *Behavior Res. Methods* 50:1657–1672.
- Kumar, L., K. Schmidt, S. Dury, and A. Skidmore. 2002. Imaging spectrometry and vegetation science. In: F.D. van der Meer and S.M. de Jong, editors, *Image Spectrometry: Basic Principles and Prospective Applications*, Volume 4. Springer, Dordrecht, The Netherlands. p. 111–155.

- Li, L., B. Jákli, P. Lu, T. Ren, J. Ming, S. Liu, S. Wang, and J. Lu. 2018a. Assessing leaf nitrogen concentration of winter oilseed rape with canopy hyperspectral technique considering a non-uniform vertical nitrogen distribution. *Ind. Crops Products* 116:1–14.
- Li, L., S. Wang, T. Ren, Q. Wei, J. Ming, J. Li, X. Li, R. Cong, and J. Lu. 2018b. Ability of models with effective wavelengths to monitor nitrogen and phosphorus status of winter oilseed rape leaves using in situ canopy spectroscopy. *Field Crops Res.* 215:173–186.
- Liew, O.W., P.K.J. Chong, B. Li, and A.K. Asundi. 2008. Signature optical cues: Emerging technologies for monitoring plant health. *Sensors* 8:3205–3239.
- Liu, G., K. Morgan, B. Hogue, Y. Li, and D. Sui. 2015. Improving phosphorus use efficiency for snap bean production by optimizing application rate. *Hortic. Sci.* 42:94–101.
- Liu, Y., Z. Wang, Q. Sun, A.M. Erb, Z. Li, C.B. Schaaf, X. Zhang, M.O. Román, R.L. Scott, and Q. Zhang. 2017. Evaluation of the VIIRS BRDF, albedo and NBAR products suite and an assessment of continuity with the long term MODIS record. *Remote Sens. Environ.* 201:256–274.
- Mahajan, G., R. Pandey, R. Sahoo, V. Gupta, S. Datta, and D. Kumar. 2017. Monitoring nitrogen, phosphorus and sulphur in hybrid rice (*Oryza sativa* L.) using hyperspectral remote sensing. *Precision Agric.* 18:736–761.
- Majsztzik, J.C., and J.D. Lea-Cox. 2013. Water quality regulations in the Chesapeake Bay: Working to more precisely estimate nutrient loading rates and incentivize best management practices in the nursery and greenhouse industry. *HortScience* 48:1097–1102.

- Mitra, G. 2017. Essential plant nutrients and recent concepts about their uptake. In: N. Naeem et al., editors, *Essential Plant Nutrients: Uptake, Use Efficiency, and Management*. Springer, Cham, Switzerland. p. 3–36.
- Mobaraki, N., and J.M. Amigo. 2018. HYPER-Tools. A graphical and user-friendly interface for hyperspectral image analysis. *Chemometrics Intelligent Lab. Syst.* 172:174–187.
- Ortenberg, F. 2019. Hyperspectral sensors characteristics: Airborne, spaceborne, hand-held, and truck-mounted; integration of hyperspectral data with LiDAR. In: P.S. Thenkabail et al., editors, *Hyperspectral Remote Sensing of Vegetation Volume One: Fundamentals, Sensor Systems, Spectral Libraries, and Data Mining for Vegetation*. 2nd ed. CRC Press, Boca Raton, FL. p. 41–70.
- Pasolli, E., S. Prasad, M.M. Crawford, and J.C. Tilton. 2019. Advances in hyperspectral image classification methods for vegetation and agricultural cropland studies. In: P.S. Thenkabail, J.G. Lyon, and A. Huete, editors, *Hyperspectral Remote Sensing of Vegetation Volume Two: Hyperspectral Indices and Image Classifications for Agriculture and Vegetation*. 2nd ed. CRC Press, Boca Raton, FL. p. 67–104.
- Patel, P. 2016. Agriculture drones are finally cleared for takeoff. *IEEE Spectrum* 53(11):13–14.
- Pu, R. 2017. Overview of hyperspectral remote sensing. In: Q. Weng, editor, *Hyperspectral Remote Sensing Fundamentals and Practices*. CRC Press Boca Raton, FL. p. 1–30.
- Romanski, P., L. Kotthoff, and M.L. Kotthoff. 2018. Package ‘FSelector’. R Package Documentation. p. 18.
- Römheld, V. 2012. Diagnosis of deficiency and toxicity of nutrients. In: P. Marschner, editor, *Marschner’s Mineral Nutrition of Higher Plants*. 2nd ed. Academic Press, London, UK. p. 299–312.

- Roy, D.P., H.K. Zhang, J. Ju, J.L. Gomez-Dans, P.E. Lewis, C.B. Schaaf, Q. Sun, J. Li, H. Huang, and V. Kovalskyy. 2016. A general method to normalize Landsat reflectance data to nadir BRDF adjusted reflectance. *Remote Sens. Environ.* 176:255–271.
- Rustioni, L., D. Grossi, L. Brancadoro, and O. Failla. 2018. Iron, magnesium, nitrogen and potassium deficiency symptom discrimination by reflectance spectroscopy. *Sci. Hortic.* 241:152–159.
- Stevens, A., and L. Ramirez–Lopez. 2014. An introduction to the prospectr package. R Package Documentation. p. 22.
- Stroppiana, D., F. Fava, M. Boschetti, and P.A. Brivio. 2019. Estimation of nitrogen content in herbaceous plants using hyperspectral vegetation indices. In: P.S. Thenkabail et al., editors, *Hyperspectral Remote Sensing of Vegetation Volume Two: Hyperspectral indices and image classifications for agriculture and vegetation*. 2nd ed. CRC Press, Boca Raton, FL. p. 201–225.
- Sylvester-Bradley, R., and D.R. Kindred. 2009. Analysing nitrogen responses of cereals to prioritize routes to the improvement of nitrogen use efficiency. *J. Exp. Bot.* 60:1939–1951.
- Thenkabail, P.S., J.G. Lyon, and A. Huete. 2019. Advances in hyperspectral remote sensing of vegetation and agricultural crops. In: P.S. Thenkabail, J.G. Lyon, and A. Huete, editors, *Hyperspectral Remote Sensing of Vegetation Volume One: Fundamentals, Sensor Systems, Spectral Libraries, and Data Mining for Vegetation*. 2nd ed. CRC Press, Boca Raton, FL. p. 3–37.

- Thorp, K.R., G. Wan, K.F. Bronson, M. Badaruddin, and J. Mon. 2017. Hyperspectral data mining to identify relevant canopy spectral features for estimating durum wheat growth, nitrogen status, and grain yield. *Comput. Electron. Agric.* 136:1–12.
- Xie, L., G. Li, L. Peng, Q. Chen, Y. Tan and M. Xiao. 2017. Band selection algorithm based on information entropy for hyperspectral image classification. *J. Appl. Remote Sens.* 11:026018.
- Yang, C., R. Sui, and W.S. Lee. 2016. Precision agriculture in large-scale mechanized farming. In: Q. Zhang, editor, *Precision Agriculture Technology for Crop Farming*. CRC Press, Boca Raton, FL. p. 177–212.
- Zhang, X., F. Liu, Y. He, and X. Gong. 2013. Detecting macronutrients content and distribution in oilseed rape leaves based on hyperspectral imaging. *Biosyst. Eng.* 115:56–65.
- Zhou, X., W. Huang, J. Zhang, W. Kong, R. Casa, and Y. Huang. 2019. A novel combined spectral index for estimating the ratio of carotenoid to chlorophyll content to monitor crop physiological and phenological status. *Int. J. Appl. Earth Observation Geoinformation* 76:128–142.

CHAPTER 6

Spectral Characterization of Boron Toxicity in Flue-Cured Tobacco

(Written in the style of Agronomy Journal)

Spectral Characterization of Boron Toxicity in Flue-Cured Tobacco

Core Ideas:

- Hyperspectral reflectance data successfully classified B toxicity in tobacco.
- Symptoms and spectral properties differed based on sensor type and field location.
- Nearest-neighbor and discriminant analyses developed high accuracy models.

Abstract

Spectral remote sensing has been successfully utilized for characterizing and classifying a variety of plant health problems including nutrient disorders. Few studies have investigated the spectral response nutrient toxicities in agronomic species. Boron toxicity can be a significant problem in sensitive species such as tobacco (*Nicotiana tabacum* L.). This study characterized the spectral responses observed from greenhouse and field-grown flue-cured tobacco plants using ground-based and aerial sensors. Information entropy and derivative analyses resulted in the selection of several wavelengths responsible for a high degree of the observed variability. Selected bands from greenhouse and field experiments were found throughout the visible spectrum, but some of the greatest variability was observed in the red-edge between 700 and 750 nm. Principal component analysis was used to reduce dimensionality for all experiments. Linear discriminant analysis and K-nearest-neighbor methods resulted in high classification accuracies in both the greenhouse and field experiments. Greenhouse-grown tobacco exhibited 90% overall classification accuracy. In field studies, aggregating all data resulted in overall classification accuracies of 99.7%. Classification accuracies within individual hyperspectral images were typically >85%. This study demonstrates that spectral discrimination of B toxicity in flue-cured

tobacco is achievable and in environmentally controlled and field-based settings. Selected bands may be used to develop less expensive spectral sensors for use in agricultural production settings.

Abbreviations: DI, deionized; FIA, flow injection analysis; ICP-MS, inductively coupled plasma mass spectrometry; NIR, near-infrared; PAR, photosynthetically active radiation; PC, principal component; PCA, principal component analysis; PVC, polyvinyl chloride; UAV, unmanned aerial vehicle

Introduction

Scouting crops to monitor plant health is essential for maintaining high yield and quality but has traditionally been labor intensive and time consuming. Recent technological advancements provide significant opportunity to obtain rapid, quantitative measurements to reveal various plant health characteristics (Abdel-Rahman et al., 2010; Yang et al., 2016). Studies over the past several decades report successful use of spectral reflectance data for diagnosing diseases and other disorders. In many instances, spectral reflectance data may be correlated with plant nutrient status and thus work to estimate foliar nutrient concentrations or distinguish between symptomatic and asymptomatic plants. Many studies focus on deficiencies of macronutrients such as N, P, or K (Abdel-Rahman et al., 2010; Li et al., 2018a, 2018b; Stroppiana et al., 2019; Thorp et al., 2017; Zhang et al., 2013). Additional studies report spectral characterization of other nutrient deficiencies including those of Cu, Fe, Mg, Mn, and Zn (Adams et al., 2000a, 2000b; Rustioni et al., 2018). However, few studies report the effects of nutrient toxicities on the spectral response observed from symptomatic plants. Furthermore,

studies demonstrate differences in spectral response based upon plant species, requiring research to accommodate each species of interest.

Spectral reflectance data can be obtained from a variety of instruments and platforms. For instance, spectroradiometers can be held above the plant canopy or integrated with a leaf clip attachment with an independent light source. Spectroradiometers may therefore be used to rapidly obtain data in both controlled environment and field settings. Hyperspectral imagers can be used to obtain spectral reflectance data, similar to spectroradiometers, but they also enable data to be stored spatially in the form of pixels. Adding a spatial element to the data enables elucidation of patterns that would be difficult to quantify using other methods.

Boron is an element essential to the growth and structural integrity of a plant. López-Lefebvre et al. (2002) reported that tobacco exhibits preferential accumulation of B in root rather than shoot tissues. They speculated that this may be a response to prevent foliar toxicity, which can readily develop in tobacco plants (Henry et al., 2018b; López-Lefebvre et al., 2002). Increased B concentrations led to higher biomass accumulation in tobacco while also increasing the relative uptake of N, P, K, Ca, and Na (López-Lefebvre et al., 2002). In contrast, higher amounts of B decreased Mg accumulation (López-Lefebvre et al., 2002). Flue-cured tobacco is reported to begin exhibiting visual B toxicity symptoms with 484.4 mg kg⁻¹ foliar B concentrations (Henry et al., 2018b). Boron toxicity is of particular concern due to its effects on cured leaf quality. For instance, increased B uptake and availability are found to increase nicotine and other alkaloids within tobacco leaves (Ruiz et al., 2001; Tariq et al., 2010). Higher nicotine concentrations will negatively impact leaf quality as proposed regulations aim to lower acceptable nicotine levels in tobacco products (Henry et al., 2019; Lewis, 2018). Furthermore, increased concentrations of secondary alkaloids, including nornicotine negatively affect human health (Henry et al., 2019;

Hoffman et al., 1977). Therefore, it is essential to optimize B fertilization to attain desired leaf quality and chemical composition.

Numerous studies considered the spectral characteristics of nutrient disorder symptoms; however, most of these studies utilize either greenhouse-grown or field-grown plants. Few studies compare plants grown in each environment. Furthermore, most studies utilize either a spectroradiometer or a spectral imaging system and do not compare these two methods of data acquisition. The primary goal of this study was to spectrally characterize the symptoms of B toxicity in flue-cured tobacco in order to distinguish symptomatic plants from asymptomatic plants via classification. A secondary goal of this study was to compare spectral reflectance values obtained from greenhouse and field grown plants. The final objective of this study was to compare the spectral reflectance values obtained from a spectroradiometer and an unmanned aerial vehicle (UAV)-based hyperspectral imager.

Materials and Methods

Greenhouse Experiment

The experiment was replicated twice over time beginning 9 Apr. and 7 June 2018. Each replication began by sowing pelletized K-326 tobacco seeds (GoldLeaf Seed Co., Hartsville, SC) into 128-cell plug flats and placing them in a glass-glazed greenhouse at North Carolina State University in Raleigh, NC (35°47'41" N lat, 78°41'57" W long). The substrate was an 80:20 (v:v) mix of Canadian sphagnum peat moss (Conrad Fafard, Agawam, MA) and horticultural coarse perlite (Perlite Vermiculite Packaging Industries, Inc., North Bloomfield, OH), amended with mesh size #100 dolomitic limestone (Rockydale Agricultural, Roanoke, VA) at 8.9 kg m⁻³ and wetting agent (AquaGro 2000 G; Aquatrols, Cherry Hill, NJ) at 0.6 kg m⁻³. This custom

substrate was used to limit nutrient contamination that would be present in a commercial substrate. Flats were irrigated by hand with nonfertilized water until seeds germinated and cotyledons fully expanded.

Following germination, seedlings were fertilized with a solution consisting of 7.5 mmol L⁻¹ N, 0.5 mmol L⁻¹ P, 3.0 mmol L⁻¹ K, and 2.5 mmol L⁻¹ Ca. Previous experiments demonstrated tobacco seedlings require a low concentration of primary macronutrients to develop sufficiently for studies investigating nutrient disorders (Henry et al., 2018a, 2018b). The selected concentrations were a half rate of the primary macronutrient concentrations used in the nutrient-sufficient control solution. The control solution was a modified all-nitrate Hoagland solution consisting of 15.0 mmol L⁻¹ N, 1.0 mmol L⁻¹ P, 6.0 mmol L⁻¹ K, 5.0 mmol L⁻¹ Ca, 2.0 mmol L⁻¹ Mg, and 2.0 mmol L⁻¹ S, 72.0 μmol L⁻¹ Fe, 18.0 μmol L⁻¹ Mn, 3.0 μmol L⁻¹ Cu, 3.0 μmol L⁻¹ Zn, 45.0 μmol L⁻¹ B, and 0.1 μmol L⁻¹ Mo (Hoagland and Arnon, 1950) mixed with deionized (DI) water of 18 megohm purity. All nutrients were provided by the following technical grade salts (Fisher Scientific, Pittsburg, PA): Ca(NO₃)₂·4H₂O, KNO₃, KH₂PO₄, K₂SO₄, MgSO₄·7H₂O, iron chelate (Fe-DTPA), MnCl₂·4H₂O, ZnCl₂·7H₂O, CuCl₂·2H₂O, H₃BO₃, and Na₂MoO₄·2H₂O. Solution pH was adjusted to ~6.0 using NaOH. Boron toxicity was induced with a solution comprising of tenfold the concentration of B (450.0 μmol L⁻¹) contained in the control solution. Fertilizer treatments began upon transplanting into a sand culture system.

The seedlings were thoroughly drenched with DI water three consecutive times to leach any remaining nutrients prior to transplanting. Seedlings were transplanted into 12.4 cm diameter pots (Dillen, Middlefield, OH) filled with silica sand [Millersville #2 (0.8 to 1.2 mm diameter); Southern Products & Silica Co., Hoffman, NC] that was soaked in sulfuric acid and triple-rinsed with DI water prior to use. The transplanted seedlings were placed into an automated

recirculating sand culture system on 1 May and 21 June 2018. The system was built on benches in a glass-glazed greenhouse in Raleigh, NC and utilized a completely randomized design. Each segment of the system consisted of 10.2 cm diameter polyvinyl chloride (PVC) piping (Charlotte Plastics, Charlotte, NC) fit with 12.7 cm diameter PVC reducer couplings (Charlotte Plastics). Six couplings were used to hold pots and recapture irrigation solutions in each line. Fertilizer solutions were delivered via drip tubes fed from individual 20 L plastic buckets equipped with submersible pumps (model 1A; Little Giant Pump Co., Oklahoma City, OK). Each line contained one treatment. Solutions were delivered for 1 min each cycle with as many cycles necessary per day to prevent apparent water stress (i.e., wilting) between 6:00 and 18:00 hr. Nutrient solutions were replaced on a weekly basis. Plants were measured and harvested once symptoms became visually apparent.

Field Experiment

Field experiments were conducted during the 2018 growing season in Wilson, NC (35°47'43" N lat, 77°57'01" W long) and during the 2019 growing season in Wilson (35°47'42" N lat, 77°56'52" W long) and Princeton, NC (35°27'20" N lat, 78°11'18" W long). The research sites were located on farms that were planted and maintained by the farm managers. Soil samples were collected before fertilization and each research site and tests were conducted by the North Carolina Department of Agriculture and Consumer Services (NCDA&CS; Raleigh, NC). Soils were primarily sandy with average pH between 5.68 and 6.05 (Table 6.1). At both locations, NC 196 tobacco seeds (GoldLeaf Seed Co.) were sown into 288-cell (2.2 × 2.2 cm) polystyrene trays (Carolina Greenhouses, Kinston, NC) and germinated in a float system. In Wilson, the float

system utilized a 20-10-20 fertilizer (Yara, Oslo, Norway) at a constant concentration of 125 mg L⁻¹ N.

Table 6.1. Average soil properties exhibited at each field planting site.

Soil properties	Wilson, NC		Princeton, NC
	2018	2019	2019
Surface texture	loamy sand	sandy loam	sandy loam
Soil pH	5.70	5.68	6.05
CEC (cmol _c kg ⁻¹)	2.97	3.12	5.73
Humic matter (%)	0.20	0.32	0.48

There were 36 plots at each field site and the plots each received a specific rate of fertilizer. In 2018, a 6-6-18 fertilizer (Tobacco Super Rainbow; Agrium U.S., Inc., Denver, CO) was applied to 18 plots at a rate of 78.5 kg N ha⁻¹ on 4 May as a side-dress application. This rate was selected based on typical flue-cured tobacco production recommendations published by Fisher (2019). Within each plot, a strip treatment of excess B fertilizer (Coastal Agrobusiness, Inc., Greenville, NC) was applied to eight individual plants to induce B toxicity. Each strip received B at either 2.25, 4.50, or 9.00 kg ha⁻¹. The remaining 18 plots were left non-fertilized to provide a baseline with which to compare. In 2019, the same 36 plot design was implemented, but with four different fertilizer treatments. Nine plots from each base fertilizer treatment received 0, 39.25, 78.50, or 157.0 kg N ha⁻¹ from the same 6-6-18 fertilizer. Within each plot, a strip plot of excess B fertilizer was applied to individual plants. The 18 plots fertilized with 78.50 and 157.0 kg N ha⁻¹ each received three strip treatments of 12 individual plants with excess B at

4.50, 9.00, and 18.0 kg ha⁻¹. A higher maximum rate was selected in 2019 because symptoms were not as severe as expected in 2018. The B fertilizer was applied at a rate of 1.15 mL, 2.30 mL, 4.60, or 9.20 mL 10% liquid B, corresponding to 2.25, 4.50, 9.00, and 18.0 kg ha⁻¹, respectively, delivered within 250 mL solution per plant.

Spectral Measurements

A handheld spectrometer (PSM-2500; Spectral Evolution, Lawrence, MA) was used to collect spectral reflectance data throughout the study. The sensor had a spectral range of 300 to 2,500 nm and a spectral resolution of 3.5 nm at 700 nm, 22 nm at 1,500 nm, and 22 nm at 2,100 nm with the percent reflectance output in 1 nm increments. The sensor was equipped with a fiberoptic leaf clip capable of taking leaf-level measurements. This leaf clip had a self-contained light source with two light settings, of which, the higher setting was used. Leaf clip measurements were taken inside the greenhouse under ambient conditions. Measured plants were irrigated prior to measurement to ensure drought stress would not be a confounding factor.

Throughout the experiment, symptomatic and asymptomatic control plants were selected to obtain hyperspectral measurements of the individual leaves. At each measurement date, four individual plant replicates were selected. Reflectance data were collected from each leaf, except for the small bottom two to three leaves exhibiting natural senescence and the few immature upper leaves that were narrow with limited expansion. Measurements using the leaf clip were taken approximately 2 to 3 cm from the leaf margin and one-third of the leaf length away from the leaf tip. This location was selected because it typically represented the average degree of symptoms for each leaf. Areas of necrosis were avoided as necrotic tissues reflected much different patterns than non-necrotic tissues, regardless of symptomology.

Spectral measurements were taken in the greenhouse experiment at every sampling time. Each leaf was measured for every plant sampled. Throughout the experiment, symptomatic and asymptomatic control plants were selected to obtain hyperspectral measurements of the individual leaves. At each measurement date, four individual plant replicates were selected. Reflectance data were collected from each leaf, except for the small bottom two to three leaves exhibiting natural senescence and the few immature upper leaves that were narrow with limited expansion. During the field study, measurements were recorded at the final data collection in 2018 and at every data collection in 2019. Handheld spectroradiometer measurements were obtained only from the leaf clip attachment. At each data collection, one representative leaf was selected per strip and per subplot treatment for spectral analysis. The selected leaves were subsequently removed from the plant for foliar nutrient analysis.

Hyperspectral images were recorded during the field study from a UAV-based hyperspectral sensor. Hyperspectral data were collected using a UAV-mounted pushbroom scanner (Headwall Nano VNIR; Headwall Photonics, Inc., Boston, MA) attached to an UAV (DJI Matrice 600 Pro; SZ DJI Technology Co., Ltd., Shenzhen, Guangdong, China) flying at an altitude of 60 m. The sensor had a spatial resolution of 640×512 pixels, resulting in a pixel size of 1.5 cm. The spectral resolution ranged from 400–1,000 nm with 270 total bands. In 2018, data were collected by PrecisionHawk (Raleigh, NC) on 18 June, 2 July, 16 July, and 14 August. In 2019, data were obtained using the same sensor 6 June, 19 June, 3 July, 17 July, and 9 Aug.

Nutrient Analysis

Foliar tissue samples were collected in each experiment to quantify nutrient concentrations and ensure symptoms were due to the applied treatment. Leaf tissues were dried

at 70 °C for 72 hr and then ground in a sample mill (Thomas Wiley® Mini-Mill; Thomas Scientific, Swedesboro, NJ), and analyzed for nutrient concentrations (AgSource Laboratories, Lincoln, NE). Total N was processed by Kjeldahl digestion and determined via flow injection analysis (FIA). Extractable K was processed by 2% acetic acid digestion and determined via inductively coupled plasma mass spectrometry (ICP-MS). Total P and all other plant minerals were processed by nitric acid/hydrogen peroxide digestion and determined via ICP-MS. Data were analyzed in SAS (version 9.4; SAS Institute, Cary, NC) using ANOVA with means separation using the Tukey adjustment.

Data Preprocessing

Radiometric reflectance data were manipulated and analyzed using R statistical software (version 3.6.0, R Core Team, 2019). Measurements from each leaf of each treatment were assigned into several subgroups depending on various characteristics. Leaves received an objective symptom severity rating of four possible categories: 1) none, 2) low, 3) intermediate, or 4) high (Figure 6.1). Furthermore, measurement stages were separated by plant maturity: 1) young, 2) intermediate, or 3) mature. Young plants were those that had 6 or fewer leaves, intermediate plants had 7 to 12 leaves, and mature plants had more than 12 leaves. Fully mature tobacco plants developed between 18 and 20 expanded leaves prior to anthesis. Reflectance data collected by the handheld spectroradiometer were visually inspected to ensure any errors or inaccurate measures were removed (e.g., improper placement of the leaf clip). Measurements were then assigned to several classes to define plant maturity (young, intermediate, or mature), leaf location (numerically from bottom to top), and symptom severity (low, intermediate, or high). However, visible B toxicity symptoms were only observed in mature plants. Additionally,

reflectance from bands between 1350 and 1450 nm and 1800 and 1950 nm were removed from further analysis due to high water absorptance within these ranges.

Hyperspectral image tiles were orthorectified in QGIS (version 3.8 “Zanzibar”, QGIS Development Team) and merged into single raster files using the Geospatial Data Abstraction Library (GDAL; GDAL/OGR contributors, Open Source Geospatial Foundation) in Python (version 3.7.4; Python Software Foundation). Rasters were aligned in QGIS and files were converted to ENVI format using GDAL. Soils and other background noise were removed by creating a mask to retain only pixels containing vegetation. A polygon layer was created to encompass each part of the field with its corresponding treatments, and this was used to calculate average spectra from each treatment. Average treatment values were then used for further analyses instead of using individual pixel values. This was done to reduce computational complexity.

Band Selection

Spectra were used to calculate information entropy as well as first and second spectral derivatives to identify which wavelengths contribute most to the variability observed among the nutrient-deficient leaves. Information entropy is a measurement for how much variability is contained within a band and it is commonly used for hyperspectral band selection (Bajcsy and Groves, 2004; Bajwa et al., 2004; Xie et al., 2017). Derivative measures are also useful for band selection by identifying areas with rapid changes in direction or pattern within spectra (Bajcsy and Groves, 2004). Information entropy was calculated using the FSelector package (Romanski and Kotthoff, 2018) while derivatives were calculated using the prospectr package (Stevens and Ramirez-Lopez, 2014) in R. Savitzky-Golay filtering was applied with a window size of 10

bands to information entropy data to reduce noise and smooth the data. Derivatives were calculated and smoothed using the gap-segment algorithm with a filter length of 11 bands for both first and second order derivatives. Due to the nature of narrow bands, high correlation is often observed among neighboring bands (Thenkabail et al., 2019). This correlation, referred to as multicollinearity, leads to high levels of redundancy, meaning many bands will convey similar information regarding observed variability. Hence, peaks and valleys were calculated using the splus2R package (Constantine et al., 2016) to determine the greatest individual absolute values or ranges of values within a span of 10 bands. Ranges of continuous values with uniform importance were aggregated and used to determine the central wavelength representing that range. The identified wavelengths represented those with the greatest impact on observed variability.

Symptom Classification

Reflectance spectra captured using the spectroradiometer were analyzed by growth stage using principal component analysis (PCA), with 10 principal components (PCs) selected for each growth stage. Linear discriminant analysis was used to develop classification models to distinguish among the various symptoms. The classification models were subjected to a custom-built five-fold cross validation function where 80% of the data was used for model training and the remaining 20% was used to test the models. Following the first validation, a second validation was conducted with a new set of testing data previously used to train the model. This process was repeated to optimize the model until all data were used for both training and testing functions. The final classification results were put into a confusion matrix for each growth stage

and analyzed using the PredPsych package (Koul et al., 2018) in R. The matrices were used to determine the overall accuracy and misclassification rates for each model.

Hyperspectral image classification was conducted using R. Principal components analysis was used for dimensionality reduction with 10 PCs being selected per data set. The selected PCs were used to train various classification models. Several classification methods and algorithms were tested including linear discriminant analysis, quadratic discriminant analysis, K-nearest neighbors, and random forest. Discriminant analysis is a classification method that involves modeling based on multiple variables (James et al., 2013a; Thenkabail et al., 2019). The analysis attempts to determine which explanatory variables or features are optimal for separating among two or more unique classes by creating a line to best separate observations by class in a multi-dimensional space (Bajwa et al., 2019). K-nearest-neighbor classification works by classifying a test observation based on its proximity to neighboring training samples (James et al., 2013a). Pasolli et al., 2019). Random forests are a decision tree-based classification algorithm that utilize many individual decision trees (James et al., 2013b). Leave-one-out cross validation was used to test the classification models for each location and data collection separately and with all data aggregated together. Principal components analysis was used for dimensionality reduction with 10 PCs being selected per data set. Classification results were put into a confusion matrix and analyzed to determine the overall accuracy and misclassification rates for each model.

Results and Discussion

Greenhouse Study

In the greenhouse study, only mature plants fertilized with the B toxicity solution for the entirety of the study developed distinct visual symptoms. Lower and central leaves developed the

most severe symptoms. Initial symptoms were marginal dull chlorotic spots on the lowest leaves with an undulating appearance (Figure 6.1). Chlorotic spots continued to expand until the majority of lower leaves were pale yellow and only the midveins remained green. By the end of the study, some lower leaves developed marginal and interveinal necrosis.



Figure 6.1. Intermediate symptoms of B toxicity observed on greenhouse-grown flue-cured tobacco (*Nicotiana tabacum* L.).

Band selection using information entropy demonstrated peaks at 418, 462, 552, 571, 597, 623, 631, and 703 nm (Figure 6.2). First derivative analysis resulted in peaks at 383, 414, 521, 572, 612, 645, 711, and 950 nm (Figure 6.3). Second derivative analysis exhibited peaks at 393, 413, 425, 506, 538, 550, 583, 636, 693, 733, and 965 nm (Figure 6.4) First and second-order derivative spectra are often calculated for analysis of spectral reflectance data (Abdel-Rahman et al., 2010; Thorp et al., 2017). A benefit of using derivatives is that it enables one to analyze the degree of change or slope at various points in the spectra (Abdel-Rahman et al., 2010; Thorp et al., 2017). For instance, the red-edge is a common indicator of plant health based on the rapid shift from low reflectance in the red to high reflectance in the near-infrared (NIR), between 680 and 750 nm (Thorp et al., 2017). Healthy plants typically exhibit a greater rate of change in the

red-edge than do stressed plants (Abdel-Rahman et al., 2010). In the present study, each band selection method selected a band in the red-edge. Other wavelengths of interest fall in the blue, (375, 466, and 490 nm), green (515, 520, 525, 550, and 575 nm) and red (675 and 682 nm) spectra (Thenkabail et al., 2019). These wavelengths have demonstrated a response to nutrient stress or pigment changes (Thenkabail et al., 2019).

Linear discriminant analysis and K-Nearest Neighbor methods both resulted in high classification accuracy. Symptom classification using PCA-based linear discriminant analysis had 90% overall accuracy. Control plants were accurately classified 94% of the time while B-toxic plants were accurately classified 81% of the time. The higher misclassification rate exhibited by the B-toxic plants was likely because upper leaves typically remained visually asymptomatic as B accumulated primarily in the lower leaves. This could be an issue for industrial remote sensing approaches as sensors are typically oriented to view the crop from above, making the upper leaves the most prominent subject within the field of view. K-Nearest Neighbor classification resulted in higher overall accuracy at 95%, with 98% accuracy for control plants and 90% accuracy for B-toxic plants. Both methods are commonly used for similar classification scenarios, but this illustrates the importance of testing several models to determine which will provide the best fit for a given set of data.

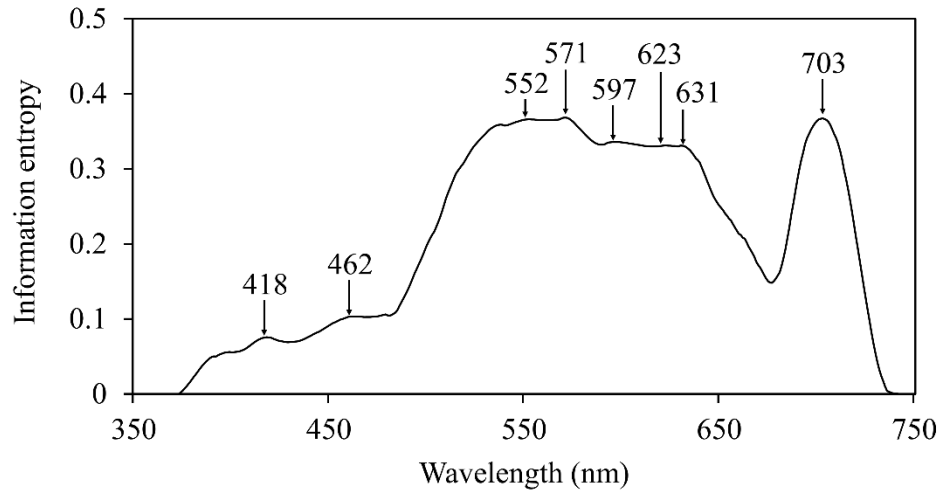


Figure 6.2. Savitzky-Golay filtered information entropy observed among mature B-toxic and control flue-cured tobacco (*Nicotiana tabacum* L.) plants. Peak wavelengths demonstrate locations with the most informative bands necessary to distinguish between B toxicity and the control.

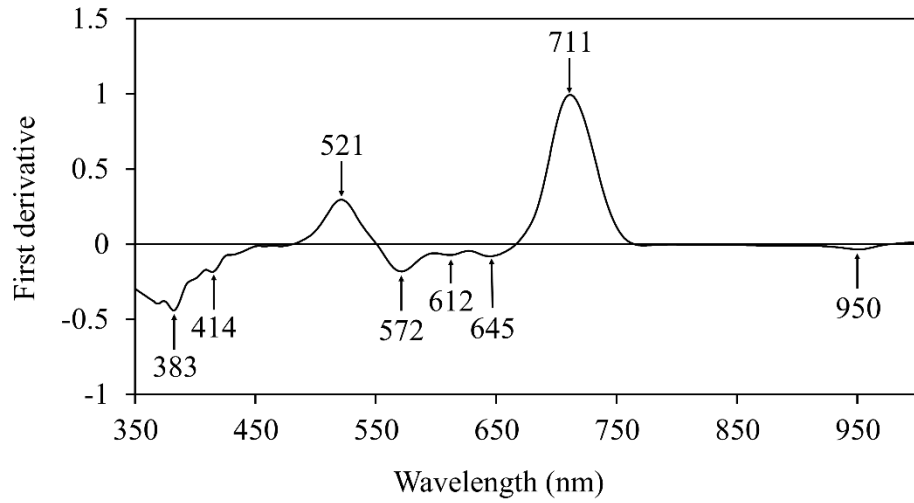


Figure 6.3. First spectral derivatives of mature B-toxic and control flue-cured tobacco (*Nicotiana tabacum* L.) plants smoothed using the gap-segment algorithm. Peak wavelengths demonstrate locations with the most informative bands necessary to distinguish between B toxicity and the control.

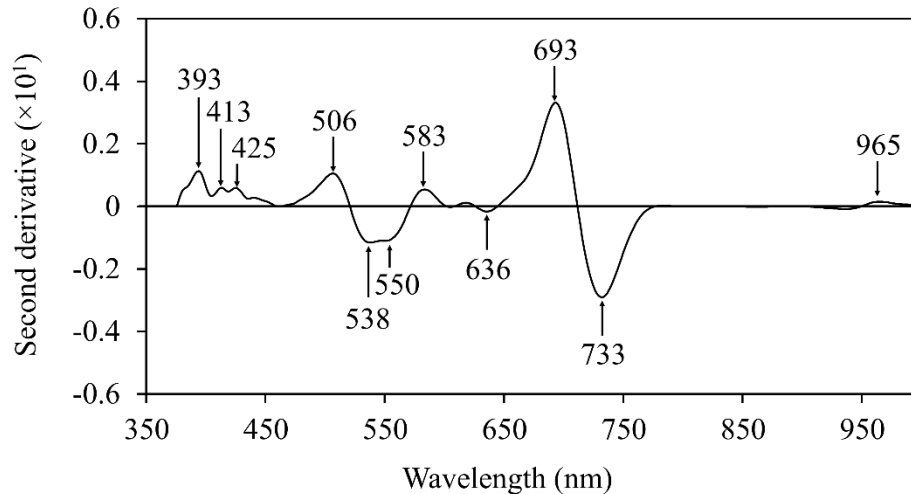


Figure 6.4. Second spectral derivatives of mature B-toxic and control flue-cured tobacco (*Nicotiana tabacum* L.) plants smoothed using the gap-segment algorithm. Peak wavelengths demonstrate locations with the most informative bands necessary to distinguish between B toxicity and the control.

Many studies demonstrate spectral patterns exhibited by specific stressors in controlled environments (Abdel-Rahman et al., 2008); however, it is important to consider that growth habits are significantly influenced by their environment. For instance, the glass panes of a greenhouse will reflect, refract, and transmit light of specific wavelengths, altering the quantity and quality of light reaching the leaf surface compared to a plant grown in the presence of direct sunlight (Liew et al., 2008). This and other factors in a controlled environment (e.g., substrate, pot size, irrigation frequency) will certainly affect the growth and spectral signature compared to field-grown plants. Therefore, controlled environment studies are good for research purposes, but cannot always be directly applied to field situations without prior testing.

Field Study

In the field studies, symptoms of B toxicity were variable based on location. In 2018, symptoms were moderate in Wilson, leading us to apply higher concentrations in 2019. In 2019, symptoms in Princeton were often visually indistinguishable from other plants within each subplot, while symptoms in Wilson were quite severe. Similar to what was observed in the greenhouse experiment, toxicity symptoms of a spotty chlorosis began on the lower leaves (Figure 6.5). The leaves also developed an undulating appearance with chlorotic spots becoming convex or concave. Symptoms progressed up the plant with central leaves developing chlorotic spots and lower leaves developing a dark amber chlorosis. Leaf margins became necrotic and curled upward (Figure 6.5). Later in the season, lower and central leaves developed necrotic spots that desiccated and in severe cases would disintegrate. Holes developed across the surface of the leaf, causing a “window-pane” effect. Foliar B concentrations were higher in B treated plants than those grown without excess B. Average B concentrations were 34.25 g kg^{-1} in control plants and 161.64 g kg^{-1} in B-treated plants. The highest foliar B concentrations were found in plants grown with 9 or 18 kg ha^{-1} B, reaching mean B concentrations up to 282.30 g kg^{-1} .



Figure 6.5. Symptoms of B toxicity observed on field-grown flue-cured tobacco (*Nicotiana tabacum* L.).

The K-Nearest Neighbors algorithm in combination with leave-one-out cross validation resulted in the highest classification accuracy among the hyperspectral images. Overall classification accuracy was 99.7% with all data aggregated. As demonstrated in Figure 6.6 classification accuracy reached 100% for several classes, with the lowest accuracy at 97.2%. Boron-toxic plants were highly distinguishable from control plants and were typically distinguishable based on each individual N and B rate combination (Fig. 6). Additionally, control plants fertilized with different rates of the complete 6-6-18 fertilizer were distinguishable from one another (Figure 6.6). In comparison to the results of the greenhouse study, discriminant analysis led to poor classification results for the field-based toxicity data (< 60%). This may have been due to the numerous factors not controlled for in the field such as temperature, root-zone nutrient availability, and irrigation frequency.

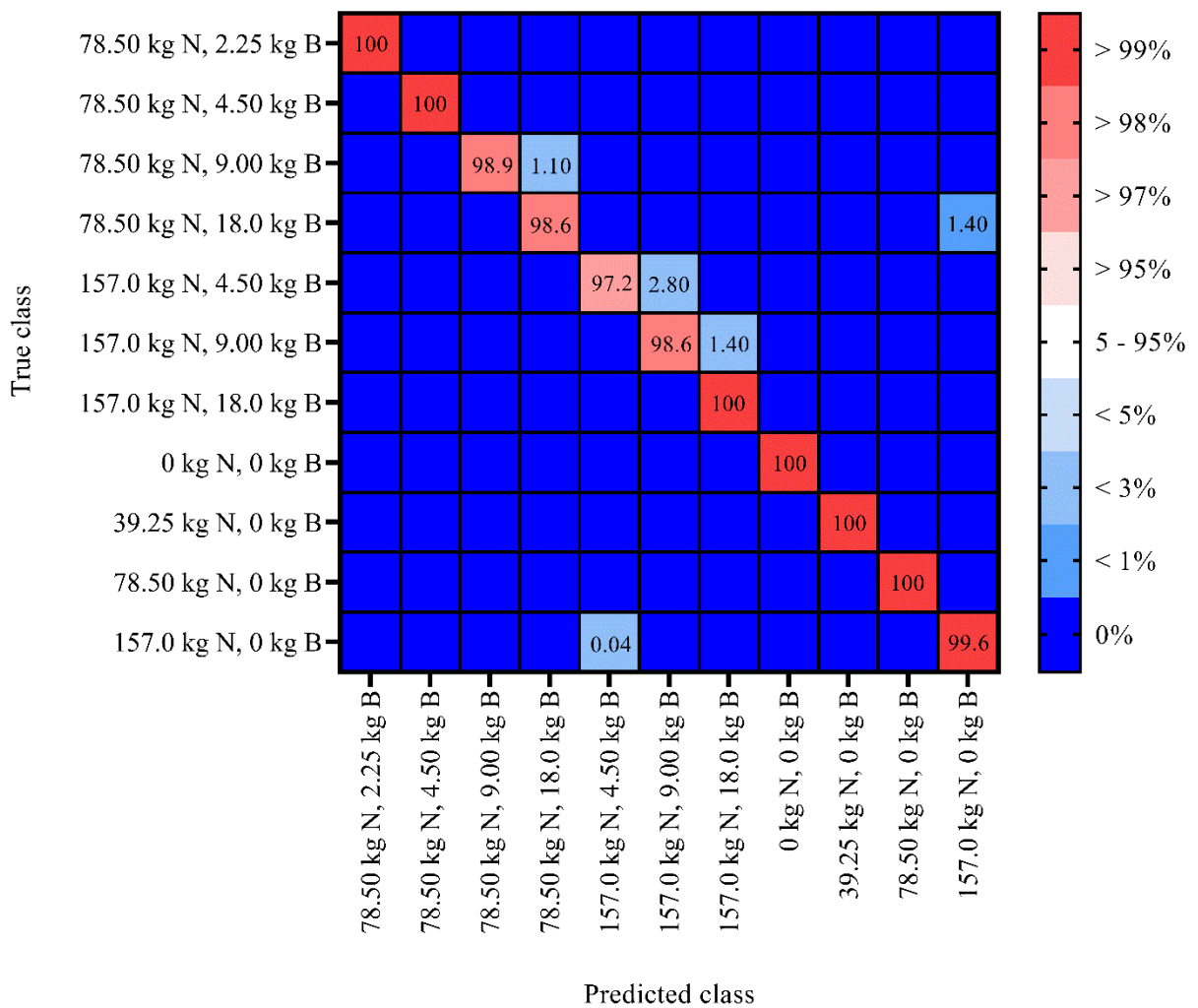


Figure 6.6. Heat map demonstrating classification accuracies achieved among aggregated data from all fertilizer treatment combinations used in the 2018 and 2019 field studies. Red cells along the diagonal represent the percentage of correctly classified subjects within a row while the blue cells represent the percentage of misclassified subjects within a row.

Average spectral signatures for each treatment varied over time and by location, so it was also of interest to determine classification accuracy for each individual image. In 2018, overall classification accuracy for the first image was 85% (Table 6.2); however, the controls were

classified with 100% accuracy and all plants fertilized with excess B were classified into one of the B-toxic classes. This demonstrates that the excess B fertilization treatments were highly distinguishable from control plants even though classification by the specific B rate was relatively low at 50%, 50%, and 66% for the 2.25, 4.5, and 9 kg ha⁻¹ B treatments, respectively. This trend was observed throughout the remaining 2018 imagery, with B-toxic and control plants always being 100% distinguishable from each other. Overall classification accuracies remained at 85% for each image throughout the 2018 growing season (Table 6.2).

In 2019, overall classification accuracies at the Wilson site were 87%, 87%, 89%, 87%, and 87% for the first, second, third, fourth, and fifth images, respectively (Table 6.2). As observed in 2018, classification between control and B toxicity treatments was high with most misclassification occurring among the various rates within the control or B toxicity treatments. It is also important to note that only 5 classes were used in 2018, while 10 classes were used in 2019 due to the additional fertilizer rates. The 2019 experiments had a higher B fertilization treatment (18 kg B ha⁻¹) as well as two additional complete fertilizer rates (39.25, and 157.0 kg N ha⁻¹ from a 6-6-18 fertilizer). Although the number of classes doubled, the classification accuracy was similar for 2019 imagery. The first two images acquired in Princeton were not used due to image misalignment. Overall accuracies for the third, fourth, and fifth flights were 89%, 94%, and 95%, respectively (Table 6.2).

Table 6.2. Overall classification accuracies calculated among flue-cured tobacco (*Nicotiana tabacum* L.) plants exhibiting different levels of B toxicity for each hyperspectral image.

Location	Year	Image number	Classification accuracy (%)
Wilson	2018	1	85
Wilson	2018	2	85
Wilson	2018	3	85
Wilson	2018	4	85
Wilson	2019	1	87
Wilson	2019	2	87
Wilson	2019	3	89
Wilson	2019	4	87
Wilson	2019	5	87
Princeton	2019	3	89
Princeton	2019	4	94
Princeton	2019	5	95

These classification results are interesting due to the variability in symptoms observed between years and locations. Although B toxicity symptoms were visually more distinct in Wilson in 2019, classification accuracy was higher in Princeton for the fourth and fifth flights. This illustrates how spectral reflectance can elucidate differences that are not visually apparent. Visual symptoms do not appear to necessarily correlate with classification accuracy, demonstrating a significant advancement over traditional scouting methods. The different

symptom severities observed may have been due to differences in soil composition, cultural practices, or environmental conditions. However, hyperspectral discrimination among treatments was highly accurate whether data were aggregated or separated by location and year.

Peaks identified using information entropy demonstrate wavelengths responsible for explaining the highest proportions of variability. When aggregating all data, maximum information entropy was observed at 484, 598, 668, 797, and 911 nm (Figure 6.7). These bands may prove useful for the development of inexpensive sensors with fewer measured bands for identifying B toxicity in tobacco. In hyperspectral remote sensing, the dimensionality can be considered equal to the number of bands being measured. Hyperspectral sensors with hundreds of bands exhibit high dimensionality, which leads to a sparsity of data that limits statistical power. This phenomenon is commonly referred to as the curse of dimensionality (Bajwa et al., 2019). With increasing dimensionality comes an exponential increase in the amount of data required to derive statistically significant results (Bajwa et al., 2019; Thenkabail et al., 2019). High dimensionality may also lead to overfitting of statistical models (Thenkabail et al., 2000). Dimensionality reduction attempts to eliminate redundancy while maintaining data that explain a high degree of the variability (Thenkabail et al., 2019).

The ultimate goal of band selection and dimensionality reduction is to use the minimum number of explanatory variables while maximizing model accuracy and computational efficiency (Bajwa et al., 2019). Selected bands could be used to develop multispectral sensors that are made to monitor specific crop-stressor pairs. Over time, research will elucidate which bands are most important and which are redundant for various agricultural applications (Thenkabail et al., 2019). This will greatly increase the speed at which useful information is extracted from hyperspectral data and implemented in commercial production settings. Table 6.3 demonstrates the highest

entropy wavelengths for each image. In general, the most important wavelengths were centered near 600, 690, 750, 775, 860, and 925 nm (Table 6.3). Wavelengths identified multiple times include 556, 607, 757, 777, and 862 nm (Table 6.3).

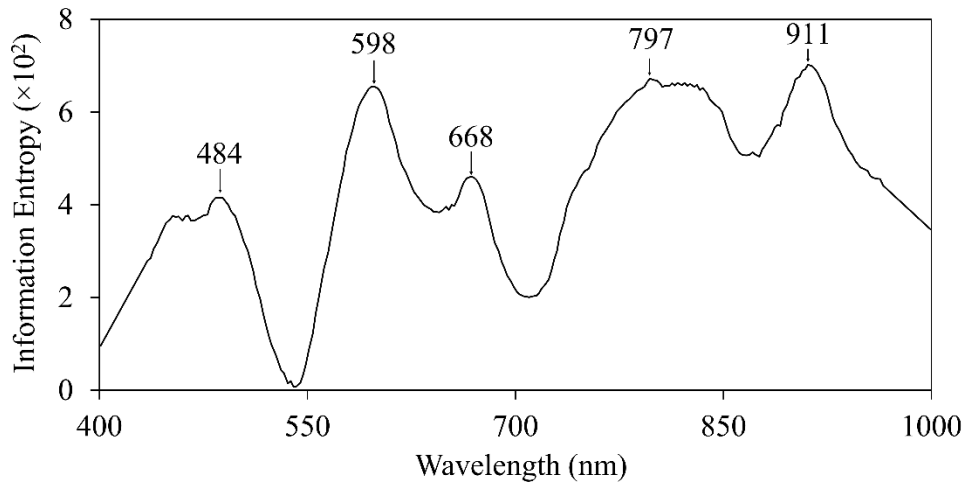


Figure 6.7. Savitzky-Golay filtered information entropy observed among mature B-toxic and control flue-cured tobacco (*Nicotiana tabacum* L.) plants. Peak wavelengths demonstrate locations with the most informative bands necessary to distinguish between B toxicity and the control.

Table 6.3. Five highest information entropy wavelengths for classifying among flue-cured tobacco (*Nicotiana tabacum* L.) plants exhibiting different levels of B toxicity for each hyperspectral image.

Location	Year	Image number	Wavelength (nm)†				
Wilson	2018	1	779	893	945	730	400
		2	777	874	757	556	600
		3	777	400	862	672	478
		4	755	831	927	556	607
Wilson	2019	3	918	773	609	862	699
		4	936	768	822	585	520
		5	929	677	484	757	858
Princeton	2019	3	580	692	627	607	516
	2019	4	632	690	748	826	920
	2019	5	635	—‡	—	—	—

† Peak identified wavelengths ranked with the highest information entropy on the left and decreasing entropy to the right.

‡ Missing values are due to uniform entropy among all other wavelengths.

First and second derivative spectra were calculated with all data aggregated and separately for each image. First derivative spectra for the aggregated data set demonstrate highest absolute values at 520, 585, 650, 712, and 925 nm (Figure 6.8). Second derivative spectra demonstrated highest absolute values at 491, 549, 683, 744, 898, and 943 nm (Figure 6.8). In general, similar wavelengths were selected from first (Table 6.4) and second (Table 6.5) spectral

derivatives for each individual image. This demonstrates that the spectral signatures observed within each image had significant changes in slope near the same wavelengths regardless of time or location. Spectral signatures from each hyperspectral image exhibited high variability, but the similar inflection points identified using derivative analysis indicate that a reasonably large training dataset may be used to classify B toxicity in flue-cured tobacco without having to subset data based on growth stage or location.

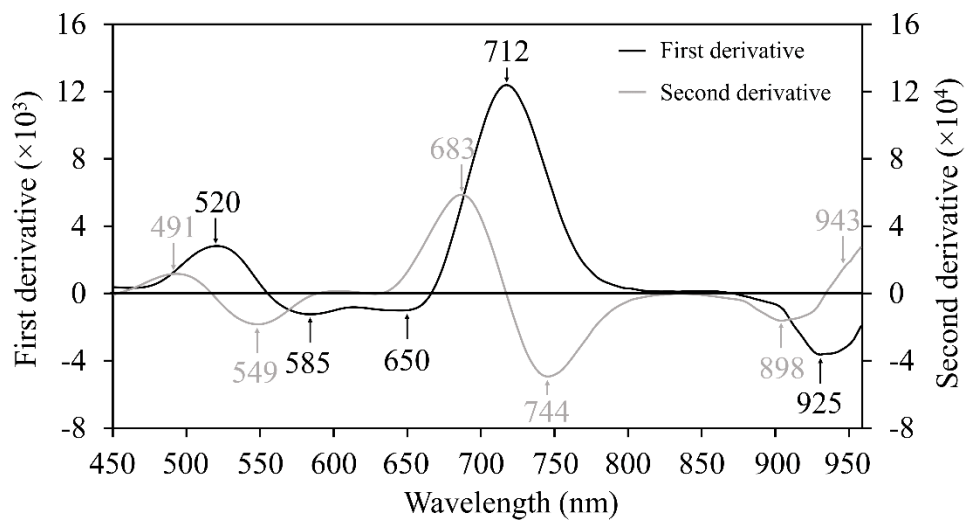


Figure 6.8. First and second derivatives for aggregated flue-cured tobacco (*Nicotiana tabacum* L.) plant data smoothed using the gap-segment algorithm. Peak wavelengths demonstrate locations with the most informative bands necessary to distinguish among each nutrient deficiency.

Table 6.4. Five most significant wavelengths selected for discrimination among flue-cured tobacco (*Nicotiana tabacum* L.) exhibiting different levels of B toxicity for each hyperspectral image. Wavelengths were selected based on first derivate spectra peaks and valleys with highest absolute values.

Location	Year	Image number	Wavelength (nm)†				
Wilson	2018	1	717	522	938	639	585
Wilson	2018	2	715	522	938	650	589
Wilson	2018	3	715	522	940	645	587
Wilson	2018	4	708	522	934	650	592
Wilson	2019	1	712	518	931	578	623
Wilson	2019	2	712	518	931	578	623
Wilson	2019	3	715	520	923	583	641
Wilson	2019	4	712	518	925	583	645
Wilson	2019	5	710	520	931	589	650
Princeton	2019	3	712	520	925	583	639
Princeton	2019	4	715	925	518	580	632
Princeton	2019	5	708	518	925	587	647

† Peak identified wavelengths ranked with the highest absolute derivative value on the left and decreasing values to the right.

Table 6.5. Five most significant wavelengths selected for discrimination among flue-cured tobacco (*Nicotiana tabacum* L.) exhibiting different levels of B toxicity for each hyperspectral image. Wavelengths were selected based on second derivate spectra peaks and valleys with highest absolute values.

Location	Year	Image number	Wavelength (nm)				
Wilson	2018	1	685	748	551	495	898
Wilson	2018	2	683	746	554	495	900
Wilson	2018	3	683	744	554	495	900
Wilson	2018	4	679	737	554	495	898
Wilson	2019	1	683	741	547	491	907
Wilson	2019	2	683	741	547	491	907
Wilson	2019	3	683	744	549	898	491
Wilson	2019	4	683	744	547	898	491
Wilson	2019	5	681	739	551	898	493
Princeton	2019	3	683	744	549	898	493
Princeton	2019	4	685	744	547	898	491
Princeton	2019	5	679	737	549	491	898

† Peak identified wavelengths ranked with the highest absolute derivative value on the left and decreasing values to the right.

Boron toxicity symptoms were readily induced in both greenhouse and field settings. Leaves of symptomatic plants exhibited distinct spectral signatures that made classification possible. K-nearest-means classification resulted in the highest classification accuracy in most instances. Aggregating all data also led to higher classification accuracy. Information entropy and derivative analysis resulted in selection of bands which account for a large proportion of the variability. Bands in the red-edge between 700 and 750 nm typically explained the highest degree of variability, but several distinct bands were selected using each method. These results demonstrate that B toxicity can be accurately identified in flue-cured tobacco using spectral sensors.

Acknowledgements

We would like to thank the North Carolina Tobacco Foundation for funding this research. Further thanks to Vick Family Farms of Wilson, NC and Kornegay Farms of Princeton, NC for donating the field space, planting, and maintaining the research site. Thanks to Norman Harrell and Bryant Spivey for their help working with the farms. Thanks to our technicians Jeremy Machacek, Ingram McCall, and Scott Whitley for managing research preparation. Lastly, thank you to the graduate and undergraduate students for their contributions applying treatments, collecting data, and more; Jeb Bullard, Drew Clapp, Camden Finch, Paige Herring, Nathan Jahnke, Nick Manning, Channie Renn, Maggie Short, Drake Stevens, and Patrick Veazie.

References

- Abdel-Rahman, E.M., F.B. Ahmed, and M. van den Berg. 2008. Imaging spectroscopy for estimating sugarcane leaf nitrogen concentration. In: C.M.U. Neale, M. Owe, and G. D'Urso, editors, Proceedings SPIE 7104, Remote Sensing for Agriculture, Ecosystems, and Hydrology X, Cardiff, United Kingdom. p. V1–V12.
- Abdel-Rahman, E.M., F.B. Ahmed, and M. van den Berg. 2010. Estimation of sugarcane leaf nitrogen concentration using in situ spectrometry. *Int. J. Appl. Earth Observation Geoinformation* 12S:S52–S57.
- Adams, M.L., W.A. Norvell, W.D. Philpot, and J.H. Peverly. 2000a. Spectral detection of micronutrient deficiency in 'Bragg' soybean. *Agron. J.* 92:261–268.
- Adams, M.L., W.A. Norvell, W.D. Philpot, and J.H. Peverly. 2000b. Toward the discrimination of manganese, zinc, copper, and iron deficiency in 'Bragg' soybean using spectral detection methods. *Agron. J.* 92:268–274.
- Bajcsy, P., and P. Groves. 2004. Methodology for hyperspectral band selection. *Photogramm. Eng. Remote Sens.* 70:793–802.
- Bajwa, S., P. Bajcsy, P. Groves, and L. Tian. 2004. Hyperspectral image data mining for band selection in agricultural applications. *Trans. ASAE* 47:895–907.
- Bajwa, S.G., Y. Zhang, and A. Shirzadifar. 2019. Hyperspectral image data mining. In: P.S. Thenkabail et al., editors, *Hyperspectral Remote Sensing of Vegetation Volume One: Fundamentals, Sensor Systems, Spectral Libraries, and Data Mining for Vegetation*. 2nd ed. CRC Press, Boca Raton, FL. p. 273–302.
- Constantine, W., T. Hesterberg, K. Wittkowski, T. Song, and S. Kaluzny. 2016. *splus2R: Supplemental S-PLUS functionality in R*. R Package Documentation. p. 36.

- Fisher, L.R. 2019. North Carolina State University: Flue-cured tobacco guide 2019 AG-187.
Rev. ed. North Carolina Coop. Ext., Raleigh.
- Henry, J.B., M. Vann, I. McCall, P. Cockson, and B.E. Whipker. 2018a. Nutrient disorders of burley and flue-cured tobacco part 2: Micronutrient disorders. *Crop, Forage and Turfgrass Mgt.* 4:170077. doi:10.2134/cftm2017.11.0077.
- Henry, J.B., M. Vann, I. McCall, P. Cockson, and B.E. Whipker. 2018b. Nutrient disorders of burley and flue-cured tobacco part 1: Macronutrient deficiencies. *Crop, Forage and Turfgrass Mgt.* 4:170076. doi:10.2134/cftm2017.11.0076.
- Henry, J.B., M.C. Vann, and R.S. Lewis. 2019. Agronomic practices affecting nicotine concentration in flue-cured tobacco: A review. *Agron. J.* 111:1–9.
doi:10.2134/agronj2019.04.0268.
- Hoagland, R.J. and D.I. Arnon. 1950. The water-culture method for growing plants without soil. *California Agr. Expt. Sta. Circ.* 347. Revised ed.
- Hoffmann, D., M. Dong, and S.S. Hecht. 1977. Origin in tobacco smoke of N'-nitrosornicotine, a tobacco-specific carcinogen: Brief communication. *J. Natl. Cancer Inst.* 58:1841–1844.
- James, G., D. Witten, T. Hastie, and R. Tibshirani. 2013a. Classification. In: G. Casella, S. Fienberg, and I. Olkin, editors, *An Introduction to Statistical Learning with Applications* in R. Springer, New York, NY. p. 127–174.
- James, G., D. Witten, T. Hastie, and R. Tibshirani. 2013b. Tree-based methods. In: G. Casella, S. Fienberg, and I. Olkin, editors, *An Introduction to Statistical Learning with Applications* in R. Springer, New York, NY. p. 303–335.

- Koul, A., C. Becchio, and A. Cavallo. 2018. PredPsych: A toolbox for predictive machine learning-based approach in experimental psychology research. *Behavior Res. Methods* 50:1657–1672.
- Lewis, R.S. 2018. Potential mandated lowering of nicotine levels in cigarettes: A plant perspective. *Nicotine Tob. Res.* 21(7):991–995.
- Li, L., B. Jákli, P. Lu, T. Ren, J. Ming, S. Liu, S. Wang, and J. Lu. 2018a. Assessing leaf nitrogen concentration of winter oilseed rape with canopy hyperspectral technique considering a non-uniform vertical nitrogen distribution. *Industrial Crops and Products* 116:1–14.
- Li, L., S. Wang, T. Ren, Q. Wei, J. Ming, J. Li, X. Li, R. Cong, and J. Lu. 2018b. Ability of models with effective wavelengths to monitor nitrogen and phosphorus status of winter oilseed rape leaves using in situ canopy spectroscopy. *Field Crops Res.* 215:173–186.
- Lopez-Lefebvre, L., R. Rivero, P. Garcia, E. Sanchez, J. Ruiz, and L. Romero. 2002. Boron effect on mineral nutrients of tobacco. *J. Plant Nutr.* 25:509–522.
- Pasolli, E., S. Prasad, M.M. Crawford, and J.C. Tilton. 2019. Advances in hyperspectral image classification methods for vegetation and agricultural cropland studies. In: P.S. Thenkabail, J.G. Lyon, and A. Huete, editors, *Hyperspectral Remote Sensing of Vegetation Volume Two: Hyperspectral Indices and Image Classifications for Agriculture and Vegetation*. 2nd ed. CRC Press, Boca Raton, FL. p. 67–104.
- Romanski, P., L. Kotthoff, and M.L. Kotthoff. 2018. Package ‘FSelector’. R Package Documentation. p. 18.

- Ruiz, J.M., L.R. Lopez-Lefebvre, E. Sanchez, R.M. Rivero, P.C. Garcia, and L. Romero. 2001. Preliminary studies on the influence of boron on the foliar biomass and quality of tobacco leaves subjected to NO_3^- fertilisation. *J. Sci. Food Agric.* 81:739–744.
- Rustioni, L., D. Grossi, L. Brancadoro, and O. Failla. 2018. Iron, magnesium, nitrogen and potassium deficiency symptom discrimination by reflectance spectroscopy. *Sci. Hortic.* 241:152–159.
- Stevens, A., and L. Ramirez–Lopez. 2014. An introduction to the prospectr package. R Package Documentation. p. 22.
- Stroppiana, D., F. Fava, M. Boschetti, and P.A. Brivio. 2019. Estimation of nitrogen content in herbaceous plants using hyperspectral vegetation indices. In: P.S. Thenkabail et al., editors, *Hyperspectral Remote Sensing of Vegetation Volume Two: Hyperspectral indices and image classifications for agriculture and vegetation*. 2nd ed. CRC Press, Boca Raton, FL. p. 201–225.
- Tariq, M., A. Akbar, Lataf-ul-Haq, and A. Khan. 2010. Comparing application methods for boron fertilizer on the yield and quality of tobacco (*Nicotiana tabacum* L.). *Commun. Soil Sci. Plant Anal.* 41:1525-1537.
- Thenkabail, P.S., J.G. Lyon, and A. Huete. 2019. Advances in hyperspectral remote sensing of vegetation and agricultural crops. In: P.S. Thenkabail, J.G. Lyon, and A. Huete, editors, *Hyperspectral Remote Sensing of Vegetation Volume One: Fundamentals, Sensor Systems, Spectral Libraries, and Data Mining for Vegetation*. 2nd ed. CRC Press, Boca Raton, FL. p. 3–37.

- Thorp, K.R., G. Wan, K.F. Bronson, M. Badaruddin, and J. Mon. 2017. Hyperspectral data mining to identify relevant canopy spectral features for estimating durum wheat growth, nitrogen status, and grain yield. *Comput. Electron. Agric.* 136:1–12.
- Xie, L., G. Li, L. Peng, Q. Chen, Y. Tan and M. Xiao. 2017. Band selection algorithm based on information entropy for hyperspectral image classification. *J. Appl. Remote Sens.* 11:026018.
- Yang, C., R. Sui, and W.S. Lee. 2016. Precision agriculture in large-scale mechanized farming. In: Q. Zhang, editor, *Precision Agriculture Technology for Crop Farming*. CRC Press, Boca Raton, FL. p. 177–212.
- Zhang, X., F. Liu, Y. He, and X. Gong. 2013. Detecting macronutrients content and distribution in oilseed rape leaves based on hyperspectral imaging. *Biosyst. Eng.* 115:56–65.